Master thesis

Design of a PMSM for use in Formula style racing car
Master thesis in Electric Power Engineering

Andreas Carlsson

CHALMERS
UNIVERSITY OF TECHNOLOGY

Institution of Electrical Engineering
Department of Electric Power Engineering
Chalmers University of Technology
Gothenburg, Sweden 2021

Design of PMSM for use in formula style racing car

Master thesis in electric power engineering

Andreas Carlsson

Supervisor and Examiner: Stefan Lundberg

Master Thesis
Department of Electrical Engineering
Division of Electric Power Engineering
Chalmers University of technology
SE-412 96 Gothenburg
Sweden
Phone: +46 31 772 1000

Cover: Chalmers Formula Student 20 car
Printed by: Chalmers Reproservice
Gothenburg, Sweden 2021

Abstract

In 2020, the Chalmers Formula Student team identified that there were potential performance improvements that could be made on the recently implemented front motors. A re-design of the existing permanent magnet synchronous machine (PMSM) was conducted to suit the requirements of being used as front hub-motors in a formula style racing car. A drive cycle analysis tool was used to obtain the performance requirements of the front motors where several gear ratios and types of driving cycles were examined. The old motor and re-designed motors were analyzed and compared in the finite element method (FEM) software Ansys maxwell. An iterative design process of the re-designed motors was then conducted where each version is briefly described and the respective problems with it is discussed and used as a base for the design modifications made on the next version of the motor.

The efficiency, maximum power and weight of the different concepts were compared to each other and to the old motor. In the end a recommendation was made on which motor version that was the most suitable for the application. The recommended motor was between 9-12 % or 1.2-1.54 kg lighter than the old motor and was able to deliver a maximum power of 25 kW to be able to handle most expected operational points which were indicated by the drive cycle analysis tool. The motor also had the highest expected rated power of 12 kW which means that it is the least likely of the designs to overheat. The theoretical efficiency at rated operation was estimated to be 92.6 % which is 0.1 % higher than for the old motor. Also, the rotor losses of the recommended motor were lower than the rest which is one of the most critical part of the PMSM and is the most sensitive to overheating.

Acknowledgements

This master thesis would not have been possible without the very generous support from those involved. Firstly, I would like to thank Johan Åström and Simon Nilsson from AROS electronics who provided the FEM model of the motor which made this thesis possible at all. I want to thank my examiner Stefan Lundberg whose vast experience within Formula Student and electric drives was very useful when making design decisions. Finally, I would like to thank the Formula Student team who helped me to find updated vehicle parameters for the power-train model and had an almost infinite supply of high-caffeine drinks which is the fuel of an engineer.

Abbreviations

RWD - Rear wheel drive
PMSM - Permanent magnet synchronous machine
AWD - All wheel drive
4WD - Four-wheel drive
FSG - Formula Student Germany
FSAC - Formula Student Aachen (Test event)
HEV - Hybrid electric vehicle
EV - Electric vehicle
TS - Tractive system
EM - Electric machine
RMS - Root mean square
EMF - Electromotive force
MMF - Magnetomotive force
CFS - Chalmers Formula Student
CFSXX - Chalmers Formula Student team from year 20XX
MTPA - Maximum torque per ampere
FEM - Finite element method
FFT - Fast Fourier transform
PM - Permanent magnet
IPM - Interior mounted permanent magnet
COM - Centre of mass
COG - Centre of gravity
AC - Alternating current
DC - Direct current

Symbols

P_{mech} - Mechanical power $[W]$
ω - Angular velocity $[Rad/s]$
T - Torque $[Nm]$
S - Surface $[m^2]$
F_{TS} - Tractive system force $[N]$
$m_{vehicle}$ - Vehicle mass $[kg]$
a - Acceleration $[m/s^2]$
F_{Drag} - Drag force $[N]$
F_{Roll} - Rolling resistance $[N]$
C_D - Drag coefficient
v - Velocity $[m/s]$
A - Cross-section area $[m^2]$
A_{car} - Car front cross-section area $[m^2]$
ρ - Density of air $[kg/m^3]$
g - Gravitational acceleration $[m/s^2]$
C_r - Rolling resistance coefficient
α - incline angle of the road $[^o]$
P_{TS} - Tractive system power $[W]$
ΔF_{front} - Change of force on front axle $[N]$
h_{COG} - Centre of gravity height $[m]$
l_{wb} - Wheel base $[m]$
A_d - d-axis quantity

A_q - q-axis quantity
A_a - a-vector quantity
A_b - b-vector quantity
A_c - c-vector quantity
Θ - Transformation angle $[^o]$
J - Electric current density $[A/m^2]$
I_{enc} - Enclosed current $[A]$
H - Magnetic field strength $[A/m]$
V - Electric potential $[V]$
U - Voltage $[V]$
e - EMF $[V]$
i_t - Current as a function of time $[A]$
$\mathcal{F}$ - MMF $[A_{turn}]$
Φ - Magnetic flux $[Wb]$
N - Number of turns
$\Re$ - Reluctance $[H^-1]$
l_Φ - Flux path length $[m]$
μ_0 - Vacuum permeability $[H/m]$
μ_r - Relative permeability $[H/m]$
$\Re_{PMSM}$ - PMSM Reluctance $[H^-1]$
$l_{\Phi,i}$ - Partial flux path length $[m]$
A_i - Partial flux path cross-section $[m^2]$
t_{mag} - Magnet thickness $[m]$
H_{mag} - Magnetic field intensity produced by permanent magnet
A - Area m^2
B - Magnetic flux density $[T]$
I - Current magnitude $[A]$
Ψ - Flux linkage $[Wb]$
t - Time $[s]$
L - Inductance $[H]$
L_l - Leakage inductance $[H]$
L_m - Main inductance $[H]$
R_s - Phase resistance $[\Omega]$
L_{stator} - Stator inductance $[H]$
Ψ_w - Winding flux linkage $[Wb]$
Φ_w - Winding flux $[Wb]$
θ_r - Rotor angle $[^o]$
Ψ_{PM} - Magnet flux linkage $[Wb]$
Ψ_s - Stator flux linkage $[Wb]$
L_m - Main inductance $[H]$
Ψ_r - Rotor flux linkage $[Wb]$
U_a - Phase voltage in phase a $[V]$
U_b - Phase voltage in phase b $[V]$
U_c - Phase voltage in phase c $[V]$
U_{conv} - Voltage magnitude from the converter $[V]$
R_a - Phase resistance in phase a $[\Omega]$
R_b - Phase resistance in phase b $[\Omega]$
R_c - Phase resistance in phase c $[\Omega]$
$\Psi_{w,a}$ - Phase flux linkage in phase a caused by stator current a $[Wb]$
$\Psi_{w,b}$ - Phase flux linkage in phase b caused by stator current a $[Wb]$
$\Psi_{w,c}$ - Phase flux linkage in phase c caused by stator current a $[Wb]$
$\Psi_{r,a}$ - Phase flux linkage in phase a caused by the rotor flux $[Wb]$
$\Psi_{r,b}$ - Phase flux linkage in phase b caused by the rotor flux $[Wb]$

$\Psi_{r,c}$ - Phase flux linkage in phase c caused by the rotor flux $[Wb]$
L_{aa} - Self-inductance of phase a $[H]$
L_{bb} - Self-inductance of phase b $[H]$
L_{cc} - Self-inductance of phase c $[H]$
L_{ab} - Mutual inductance of phase a and phase b $[H]$
L_{ba} - Mutual inductance of phase b and phase a $[H]$
L_{bc} - Mutual inductance of phase b and phase c $[H]$
L_{cb} - Mutual inductance of phase c and phase b $[H]$
L_{ac} - Mutual inductance of phase a and phase c $[H]$
L_{ca} - Mutual inductance of phase c and phase a $[H]$
L_{aa0} - Fundamental harmonic of self-inductance in phase a $[H]$
L_{aa2} - Second order harmonic of self-inductance in phase a $[H]$
L_{ab0} - Fundamental harmonic of mutual inductance between phase a and b $[H]$
Φ_{mag} - Permanent magnet flux $[Wb]$
$\Re_{mag}$ - Permanent magnet reluctance $[H^{-1}]$
B_r - Permanent magnet remanence $[T]$
A_{mag} - Permanent magnet cross-section area $[m^2]$
W_{mag} - Permanent magnet width $[m]$
L_{stack} - Stack length $[m]$
a_{object} - Acceleration of an arbitrary object $[m/s^2]$
$F_{applied}$ - Applied force $[N]$
m_{object} - Mass of an arbitrary object $[kg]$
$r_{objrect}$ - Distance from center of object $[m]$
$\theta_{applied}$ - Angle of applied force $[^o]$
P_{coil} - Power stored in the coil $[W]$
dW_{coil} - Electric energy in the coil $[J]$
dW_{mech} - mechanical energy in the coil $[J]$
dW_{Φ} - Magnetic energy in the coil $[J]$
dW'_{coil} - Electric co-energy in the coil $[J]$
r - Radius $[m]$
P_{PMSM} - PMSM power $[W]$
T_{PMSM} - PMSM power $[Nm]$
Ω_{PMSM} - Mechanical speed of PMSM $[RPM]$
ω_{PMSM} - Angular velocity of PMSM $[Rad/s]$
U_S - Stationary frame two phase equivalent voltage $[V]$
I_S - Stationary frame two phase equivalent current $[A]$
Ψ_d - d-axis flux linkage $[Wb]$
Ψ_q - q-axis flux linkage $[Wb]$
U_d - d-axis voltage $[V]$
U_q - q-axis voltage $[V]$
i_d - d-axis current $[A]$
i_q - q-axis current $[A]$
β - MTPA angle $[^o]$
I_{mag} - Current magnitude $[A]$
L_d - d-axis inductance $[H]$
L_q - q-axis inductance $[H]$
$R_{P.U.l}$ - Per unit length resistance $[\Omega/m]$
A_{wire} - Wire cross-section area $[m^2]$
ρ_{copper} - Copper resistivity $[\Omega m]$
H_{tooth} - Tooth height $[m]$
$r_{insulation}$ - End winding insulation radius $[m]$
W_{tooth} - Stator tooth width $[m]$
R_{phase} - Phase resistance $[\Omega]$

d_{wire} - Wire diameter $[m]$
ρ_{copper} - Copper resistivity $[\Omega m]$
N_{slot} Number of stator slots
OD_{stator} - Outer diameter of the stator $[m]$
ID_{stator} - Inner stator diameter $[m]$
H_{S0} - Slot opening height $[m]$
$L_{tooth,w}$ - Length of the non-slot wedge tooth length $[m]$
A_{cu} - Copper area in the slot $[m]$
$h_{insulation}$ - End winding insulation height $[m]$
$R(T)$ - Resistance as a function of temperature $[\Omega]$
R_0 - Calculated resistance at temperature T_0 $[\Omega]$
T_0 - Temperature at which the original resistance is calculated. $[K]$
α - Temperature coefficient of resistance which determines the rise in resistivity as the temperature increases
T - Temperature of the material. $[K]$
$P_{Fe/kg}$ - Iron losses per kilogram of weight $[W/kg]$
P_0 - Per electric cycle hysteresis loss $[W]$
f_m - Magnetizing frequency $[Hz]$
σ - Conductivity of the material $[S/m]$
d - Lamination thickness $[m]$
B_{max} - Peak flux density $[T]$
G - Mobility coefficient $[m^2V^{-1}s^{-1}]$
S - Cross-section of the lamination m^2
V_0 - Material characteristic statistical distribution function of the coercive fields.
P_c - Eddy current losses $[W]$
P_e - Excess losses $[W]$
P_h - Hysteresis losses $[W]$
k_c - Eddy current loss coefficient
k_e - Excess loss coefficient
k_h - Hysteresis loss coefficient
β_m - Measured value that is material specific coefficient
$\mathcal{F}_{current}$ - Total MMF in the stator $[A/m]$
$N_{parallel}$ - Number of coils connected in parallel
N_{series} - Number of series connected coils
q - Number of slots per pole per phase
N_{pole} - Number of poles in the motor
N_{phase} - Number of phases used
$W_{w,factor}$ - Key winding factor
k_w - Winding factor
k_d - Distribution factor
k_p - Pitch factor
q_{ph} - Number of slots per phase
α_{ph} - Angle between two adjacent tooth $[^o]$
y_p - Pole pitch
α_a - Offset between fundamental flux and back EMF $[^o]$
k_w - Winding factor
A_{tooth} - Stator tooth cross-section area $[m^2]$
$N_{tooth,frac}$ - Stator tooth fractions where flux passes through
A_{slot} - Slot area $[m^2]$
ID_{stator} - Inner stator diameter $[m]$
OD_{stator} - Outer stator diameter $[m]$
$F_{L,front}$ - Lift force acting on the front axle $[N]$ $F_{L,rear}$ - Lift force acting on the rear axle $[N]$ $\mathcal{F}_0$ - No-load MMF of the permanent magnet $[A/m]$

ω_e - Electrical angular velocity $[Rad/s]$
T_{max} - Maximum torque $[Nm]$

List of Figures

List of Tables

Contents

1 Introduction

1.1 Background

Formula Student is the largest engineering competition in the world where universities compete against each other in designing, manufacturing, racing and selling a Formula style racing car. The competitions are held all over the world and consist of a series of static and dynamic events where the design of the car is put to the test and a fictional business plan for how to sell the car. There are three main classes within Formula Student. There is a class for combustion cars, one for electric cars and one for driverless cars [1]. In Europe, Formula Student Germany is currently the largest competition and the rules which they use are also mostly applicable to the other competitions. The different dynamic events which are relevant for this project will be covered in a later Section. The Chalmers Formula Student (CFS) team competes in the class for electric vehicle and has been competing in this class since 2015.

The formula student rules (EV 2.2.1) state that the maximum tractive system power out of the accumulator container must not exceed 80 kW. In addition, it is specified that regenerative braking power is unrestricted. Regenerative braking means that the motors are used to decelerate the car which will feed power back to the battery. However the rules state that the discharge and charge rate specified in the datasheet of the battery must not be exceeded. A formula style racing car will have more traction at higher speed due to the aero package producing higher downforce at higher speeds. Also when the car is accelerating, the centre of gravity (COG) will be transferred to the rear and hence there will be more traction on the rear wheels compared to the front wheels [2]. When using regenerative braking, it is at high speeds where the largest amount of power can be regenerated back to the battery. A majority of the regenerated power will come from the front motors due to the load transfer to the front wheels when decelerating which means that they will have more traction compared to the rear. The regenerative braking is also complemented by a standard disc braking system which is able to lock all four wheels on its own.

Since 2017, the Chalmers Formula Student team has been using a permanent magnet synchronous machine (PMSM) which is rated for 32 kW peak and it was designed by AROS electronics in 2017. The power requirements of that motor were specified by analysing driving cycles from data obtained by previous teams and it was mainly focused on a rear wheel driven car. The 2018 car had rear wheel drive (RWD) and had two of these new motors. During the benching, the motors were able to handle power levels of up to 40 kW for short periods of time. In 2019 four-wheel drive was implemented with two outboard hub motors in the front and two on-board motors in the rear. In 2020, the rear motors were changed to outboard hub motors as well. When 4WD was implemented, it became apparent that the powerful CFS17 motors was not fully utilized when four of them were implemented. As previously mentioned, two of the current motors are combined able to handle short stints of the maximum allowed tractive system power. That would indicate that the overall size of the motors could be reduced. Taking the load transfer during acceleration and deceleration into account, using four 20 kW motors is likely not the most optimal setup. The size reduction of the front motors will both lead to a weight reduction and provide benefits for the wheel assembly and suspension as a result of allowing for a more compact packaging.

1.2 Aim

The aim is to re-design the current motor provided by AROS electronics to be suitable for use as front motors on the Chalmers Formula Student car. The goal will be to obtain an overall size and weight reduction of the motor whilst still having sufficient performance to satisfy the requirements of formula style racing. Also, the design will seek to reduce the time required to manufacture the motor and to recommend the manufacturing methods used to assemble the stator and rotor.

1.3 Scope

The thermal behaviour of the new PMSM is not studied in detail, but instead the theoretical power losses are calculated and compared to the CFS17 PMSM. The thermal behaviour of the CFS17 PMSM is known from data obtained when benching the motor. By using the existing data combined with comparing the theoretical losses of the PMSMs, the thermal behaviour of the new design can be estimated. Possible problems with overtemperatures would be discovered when benching the motor and the most crucial components is the rotor where the magnets will demagnetize if they reach too high temperatures. The FEM model used will provide data on the iron losses, rotor losses and copper losses and hence it may be possible to predict where high temperatures are reached. Should the rotor overheat during testing it may be mitigated by changing the material of the rotor shaft to a material which conduct heat better. Different motor types will not be discussed and large changes such as the magnet positioning in the rotor, pole or slot number will not be changed. The reason for that is that the purpose of the thesis is not to design a new motor but rather to modify an existing design.

1.4 Ethical aspects

This project is about the re-design of a PMSM and the ethical aspects of such a re-design should therefore be discussed. Having proper sizing of a PMSM is important in terms of reducing unnecessary use of raw material. The choice of raw material itself also comes with some ethical problems. Since the magnet types used are rare earth magnets and the sourcing of these materials may be problematic. The reason for that is that the magnets can only be sourced from certain countries. The efficiency of a PMSM is one of the most important factors of the design and achieving a higher efficiency will reduce the requirement of large battery packs. Also, achieving lower weight traction motor will reduce the energy required to accelerate and maintain the speed of a vehicle. When it comes to this project, it is not certain that the outcome will produce the above-mentioned potential benefits. Even if the project would not produce a satisfactory results and manufacturing of the new design cannot be motivated, the tools needed for future designing new motors will be made available to all future CFS teams. Having these tools available could prove to be important, since the requirements from the motors could change both as a result of changes to other parts of the car and as a result of changes in the Formula Student rules. These aspects will be taken into account throughout this thesis.

2 CFS car

In Figure 2, the Chalmers Formula Student 2021 car is shown. The design of the car was initialized in 2019 with the goal of competing in the 2020 season. Due to the cancellation of all Formula Student competitions, the design was refined during the autumn of 2020 in order to compete in the 2021 season. This chapter will cover the powertrain of the CFS20 car, the necessary vehicle dynamics used when modelling the car in MATLAB and the different dynamic competition events which the car will participate in. The main characteristics of the car is specified in Table 1.

Figure 2: Photograph of the Chalmers Formula Student 2021 car taken at a sponsor event in 2020

Table 1: List of the main specifications for the CFS21 car

Design parameter	Specification
Chassis construction	Single piece monocoque
Length	2.92 m
Width	1.455 m
Height	1.19 m
Weight	200 kg (estimated)
Tyres	Hoosier 18x6 0 R10 R25B
Wheelbase	1.530 m
Driving wheels	4WD
Motor type	Custom PMSM
Motor controller	IGBT based 3-phase converter
Maximum battery voltage	582 V
Gear box	Planetary gearbox 1:14
Cooling	Water cooling

2.1 CFS powertrain

Chalmers Formula Student continuously develop their power train over each season. In Figure 3 the 3D-Cad model of the electric powertrain of the CFS20 car is shown. In 2020, a new battery pack was designed which had a maximum voltage of 582 V and can deliver 46.6 kW continuously and the maximum allowed 80 kW for a short duration. In Figure 3, the battery container is the lower large container with the four fans mounted on the front. The battery powers four industrial class three-phase inverters, supplied by AROS electronics, which are located in the large container above the battery container, one inverter for each motor. During the spring of 2020, the development of new in-house designed Silicon-Carbide inverters was initialized where Alexander Andersson, Erik Lund, Marcus Vencel and Rene Lause designed and tested them as their Master thesis [3] [4]. The aim was to reduce the size and the weight of the inverters. Another system which was changed for the 2020 season was that outboard hub-motors would be used on all wheels which can be seen in Figure 3. In 2019, outboard hub-motors were only used on the front. The current motors was designed by Johan Åström at AROS electronics in 2017 and are six-pole PMSMs as seen in Figure 4a and 4b which use an iron-cobalt stator. In Figure 4a the stator is shown where it has been mounted in its cooling jacket and potted using epoxy to improve insulation and thermal conduction. The motors are connected to the wheels via a planetary gearbox with a 14:1 gear ratio.

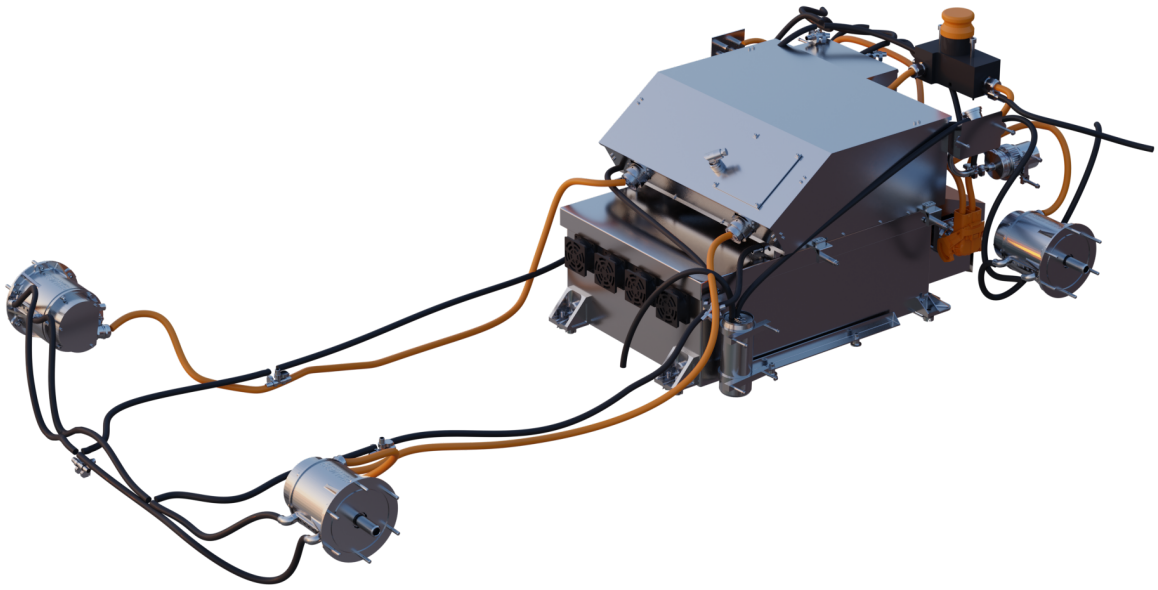

Figure 3: Rendered 3D CAD-model of the 2020 electric powertrain where the battery container, power electronics, motors and wiring can be seen

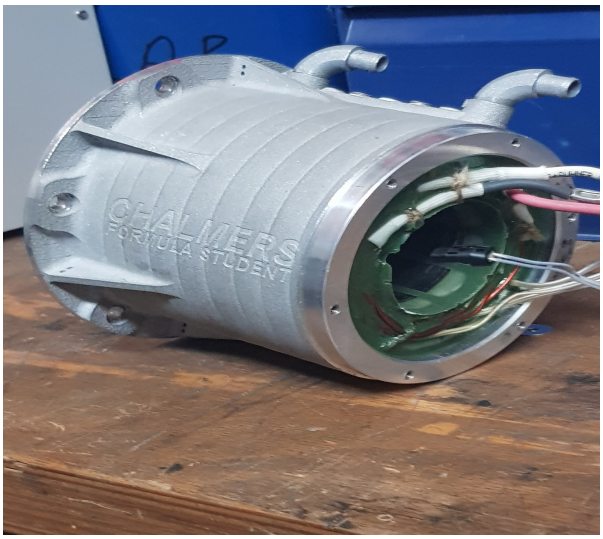

(a) CFS17 PMSM stator mounted and potted in a cooling jacket

(b) Fully assembled CFS17 rotor where two 35 mm rotor stacks has been mounted on the steel rotor shaft

Figure 4: CFS17 stator and rotor assembly

2.2 1-D Vehicle dynamics

A one-dimensional (1-D) model of the vehicle is a useful tool in order to understand how the forces act on the vehicle at various speeds and the power requirements of the vehicle. In steady state, i.e. constant speed the net horizontal forces acting on the vehicle will be equal to zero. Hence the force exerted by the tractive system must be equal to the forces acting on the vehicle in the opposite direction relative to the direction the vehicle is traveling in. There are mainly two lateral forces acting on the vehicle at speed as can be seen in Figure 5.

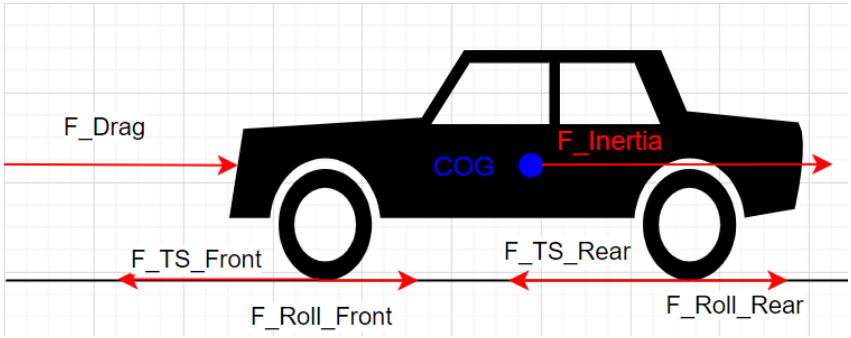

Figure 5: Illustration of the lateral forces acting on a car traveling in a straight line

There is the rolling resistance from the tires and the drag force which is caused by the vehicle displacing air when moving. The total force needed to be exerted in order to accelerate at with a given magnitude can be modelled according to

$$F_{TS} = m_{vehicle} \cdot a + F_{Drag} + F_{Roll} \tag{1}$$

where:

- F_{TS} is the total tractive force required $[N]$
- $m_{vehicle}$ is the mass of the vehicle $[kg]$
- a is the acceleration of the vehicle $[m/s^2]$
- F_{Drag} is the drag force acting on the vehicle $[N]$
- F_{Roll} is the rolling resistance experienced by the vehicle $[N]$

The drag force acting on the vehicle can be expressed according to

$$F_{Drag} = \frac{1}{2} \cdot C_D A_{car} \rho v^2 \tag{2}$$

where:

- C_D is the drag coefficient
- v is the velocity of the car $[m/s]$
- ρ is the density of air $[kg/m^3]$
- A_{car} is the front cross-sectional area of the car $[m^2]$

And the rolling resistance is calculated according to

$$F_{Roll} = gm_{vehicle}C_r cos(\alpha) \tag{3}$$

where:

- g is the gravitational acceleration m/s^2
- C_r is the rolling resistance coefficient
- α is the angle of incline of the road surface [^{o}]

The power needed from the tractive system in order to create the force needed to accelerate or maintain a certain speed is expressed as

$$P_{TS} = F_{TS} \cdot v \tag{4}$$

where P_{TS} [W] is the tractive system power required. According to the FSG rules [1], the maximum allowed tractive system power taken out from the accumulator is limited to 80 kW.

2.2.1 Power distribution

Since the CFS car has several motors providing traction power the main problem will be to define how it should be distributed. In addition to the horizontal forces acting on the car, there will also be vertical forces acting on the car which is shown in Figure 6. The vertical forces acting down on the car is the gravitational force and the downforce produced by the aero package of the car. These forces are countered by the normal force acting in the opposite direction on the tires of the car.

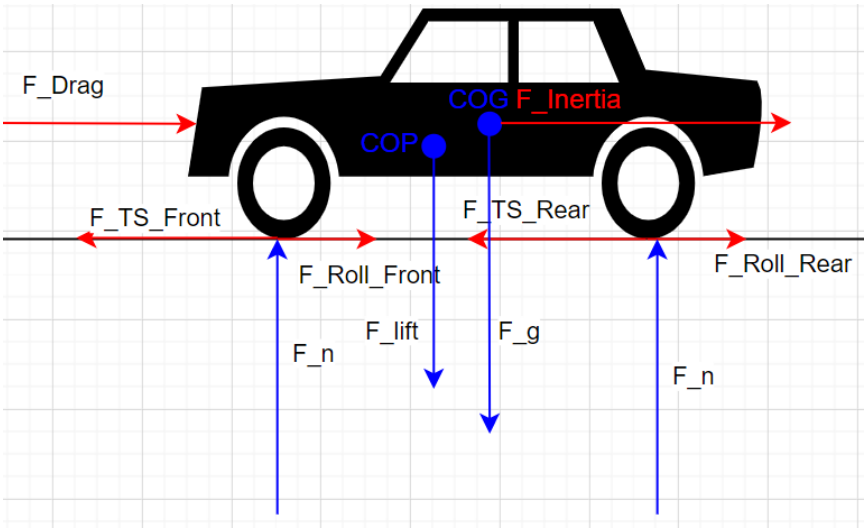

Figure 6: Lateral and vertical forces acting on a car traveling in a straight line

The weight distribution of the car will determine where the gravitational force vector will act on the car and in cartesian coordinates of the car centre of mas (COM) can be determined as [5]

$$x_{cm} = \frac{m_1 x_1 + m_2 x_2 + m_3 x_3 \cdots m_n x_n}{m_{vehicle}} = \frac{1}{m_{vehicle}} \sum_{i=1}^{n} m_i x_i \tag{5}$$

$$y_{cm} = \frac{m_1 y_1 + m_2 y_2 + m_3 y_3 \cdots m_n y_n}{m_{vehicle}} = \frac{1}{m_{vehicle}} \sum_{i=1}^{n} m_i y_i \tag{6}$$

$$z_{cm} = \frac{m_1 z_1 + m_2 z_2 + m_3 z_3 \cdots m_n z_n}{m_{vehicle}} = \frac{1}{m_{vehicle}} \sum_{i=1}^{n} m_i z_i \tag{7}$$

where:

- x_{cm} is the coordinate in x-direction of the COM $[m]$
- y_{cm} is the coordinate in y-direction of the COM $[m]$
- z_{cm} is the coordinate in z-direction of the COM $[m]$
- m_i in the mass in point i $[kg]$
- x_i is the x-coordinate of the centre of mass in point i $[m]$
- y_i is the y-coordinate of the centre of mass in point i $[m]$
- z_i is the z-coordinate of the centre of mass in point i $[m]$

If it can be assumed that the gravitational acceleration is constant everywhere on the car, the centre of gravity (COG) will be the same as the COM. The z-coordinate z_{cm} is usually defined as the height of the COM and hence in the case of the car, also the height of the COG. If the COG is located at the most middle point of the car, i.e. the weight distribution is 50/50, the normal force acting on each tire will be equal. The normal force acting on each tire will influence the level of traction on each individual tire. In vehicle dynamics, there are two dynamic factors influencing the distribution of normal force acting on the tires. There is weight transfer and there is load transfer. Weight transfer is the change of COM as a result of change of weight distribution caused by objects moving within the car. One common cause of weight transfer is the liquids in the car moving within their containers and hence changing the weight distribution. Load transfer is the change of load on each tire when accelerating and decelerating. The cause of load transfer is that the traction power is directed through the wheels and not through the COG of the car. The inertia from the COG will cause moments with the opposite direction to the traction forces exerted by the tires. That is because the traction forces do not pass through the COM. The level of load transfer can be reduced by lowering the COG. The load transfer is also affected by the incline of the road surface [2]. The load transfer of a car as a result of acceleration or deceleration can be calculated as

$$\Delta F_{front,cm} = -a \frac{z_{cm}}{l_{wb}} m_{vehicle} \tag{8}$$

where:

- $\Delta F_{front,cm}$ is the change in force on the front axle of the vehicle caused by the COG $[N]$
- l_{wb} is the wheelbase $[m]$

As previously mentioned, the incline of the road will also influence the load transfer of the vehicle and is calculated as

$$\Delta F_{front,incline} = -m_{vehicle} g \frac{l_r(1 - cos(\theta_{road})) + z_{cm} sin(\theta_{road})}{l_{wb}} \tag{9}$$

where:

- $\Delta F_{front,incline}$ is the change in force on the front axle of the vehicle caused by the incline of the road $[N]$
- l_r is the horizontal distance between the COG and the rear axle $[m]$
- θ_{road} is the angle of incline on the road $[^o]$

The aerodynamic drag forces acting on the vehicle can also influence the load transfer of the car. The aerodynamic drag force will influence the load transfer according to

$$\Delta F_{front,drag} = -F_{drag} \frac{h_{drag}}{l_{wb}} \tag{10}$$

where h_{drag} $[m]$ is the height at which the aerodynamic drag force acts on the vehicle and $\Delta F_{front,drag}$ is the change in force on the front axle of the vehicle caused by the incline of the road $[N]$. The aerodynamic lift force will also influence the lead transfer. The lift forces on each axle is defined as

$$F_{L,front} = \frac{1}{2} c_{l,front} \rho A_{car} v^2 \tag{11}$$

$$F_{L,rear} = \frac{1}{2} c_{l,rear} \rho A_{car} v^2 \tag{12}$$

where:

- $F_{L,front}$ is the lift force acting on the front axle $[N]$
- $F_{L,rear}$ is the lift force acting on the rear axle $[N]$

The normal forces acting on the tires will determine the level of traction on each individual tire and can be written as

$$F_{n,front} = F_{n,front}(v = 0) + \Delta F_{front,cm} + F_{L,front} + \Delta F_{front,drag} \tag{13}$$

$$F_{n,rear} = F_{n,rear}(v = 0) - \Delta F_{front,cm} + F_{L,rear} - \Delta F_{front,drag} \tag{14}$$

where:

- $F_{n,front}$ is the normal force acting on the front tires $[N]$
- $F_{n,front}(V = 0)$ is the normal force acting on the front tires as the car is stationary $[N]$
- $F_{n,rear}$ is the normal force acting on the rear tires $[N]$
- $F_{n,rear}(V = 0)$ is the normal force acting on the rear tires as the car is stationary $[N]$

When a tire is rotating, it will translate to a certain vehicle speed. If there is no traction, the wheel will spin and generate no forward speed for the vehicle. The relationship between the speed of the vehicle and the speed of the tire is defined as slip [2]. When accelerating, the slip is calculated using

$$s_a = \frac{r_{tire}\omega_w - v}{r_{tire}\omega_w} \tag{15}$$

where:

- s_a is the slip of the wheels when accelerating
- r_{tire} is the tire radius $[m]$
- ω_w is the angular speed of the wheel $[rad/s]$

When decelerating, the slip is instead defined as

$$s_d = \frac{v - r_{tire}\omega_w}{v} \tag{16}$$

where s_d is the slip of the wheels when decelerating. The grip levels of the tires are determined by the friction force between the ground and the tires [2]. There are two types of friction which can occur. There is static friction and kinetic friction [5]. If there is no slip, the maximum friction is calculated using

$$f_s = \mu_s f_n \tag{17}$$

where:

- f_s is the maximum static friction $[N]$
- μ_s is the static friction coefficient
- f_n is the normal force $[N]$

If the traction force exceeds the maximum static friction, there will be some slip from the tires. Then the friction force is calculated using

$$f_k = \mu_k f_n \tag{18}$$

where μ_k is the kinetic friction coefficient and f_k $[N]$ is the kinetic friction [5]. From (17) and (18) it can be seen that the normal force will determine the maximum friction that can be achieved. That means that when load transfer occurs, the maximum friction on the front and rear wheels will change and hence the level of traction will differ [2]. The traction force applied will relate to an applied torque which is given according to

$$T_w = \begin{cases} f_s r_{tire} & static \\ f_k r_{tire} & kinetic \end{cases} \tag{19}$$

where T_w $[Nm]$ is the wheel torque. The angular velocity relates to the vehicle speed according to

$$v_{tire} = \omega_w r_{tire} \tag{20}$$

where v_{tire} $[m/s]$ is the circumference velocity of the wheel. The torque of the wheel is transferred through a planetary gearbox which transforms the torque and speed whilst maintaining most of the power.

The relationship between the wheel torque & speed and the PMSM torque & speed is given as

$$\omega_w \cdot T_w = \eta_{GB} \cdot \omega_{mech} \cdot T_{PMSM} \tag{21}$$

where:

- η_{GB} is the efficiency of the planetary gearbox [%]
- ω_{mech} is the mechanical speed of the PMSM $[rad/s]$
- T_{PMSM} is the torque produced by the PMSM $[N]$

The mechanical power produced by the PMSM is calculated using

$$P_{mech} = T_{PMSM} \cdot \omega_{mech} \tag{22}$$

where P_{mech} is the mechanical power $[W]$. One property which is unique to electric vehicles is the ability to regenerate power when braking. If the forward rotation of the machine is defined by a positive value, applying negative torque will according to (22) cause a negative powerflow to the EM and hence energy can be regenerated. The use of regenerative braking will decrease the average power used during a driving cycle. That is however assuming that all other variables are unaffected by the implementation of regenerative braking and that a negative torque relative to the direction of rotation is applied at any point during the drive cycle. In the powertrain model, a speed controller is required additionally which calculates traction force required to follow the speed of the driving cycles, i.e. the controller will act as the driver of the car.

2.3 Formula Student competition dynamic events

At the Formula Student competitions, there are four dynamic events which the car will compete in [1]. The events are:

- Acceleration
- Autocross
- Endurance
- Skidpad

The skidpad event is not relevant for this project since it is not limited by the performance from the motors in terms of maximum power or rated power.

2.3.1 Autocross

The autocross event is a timed event where the team has four attempts at setting a lap time on the autocross track. The specifications of the track are listed in Table 2 as specified in the FSG rules [1]. The track layout itself can vary depending on the competition. The logged data from a typical autocross run is shown in Figure 7 where the distance, reference and vehicle speed from the vehicle model is shown. All of the autocross events used in the simulations will have similar characteristics to the one shown. What should be noted in Table 2 and as can be seen in Figure 7 is that the expected duration of the event is between one and two minutes with a distance of less than 1.5 km which means that the driver does not need to save energy during the event and can drive the vehicle as fast as possible.

Table 2: Autocross track layout rules and event specification [1]

Track specification	
Distance	$\geq$ 1.5 km
Straights	$\geq$ 80 m
Constant turn diameter	$\geq$ 50 m
Hairpin turn outside diameter	$\geq$ 9 m
Slaloms	7.5-12 m cone spacing
Track width	$\geq$ 3 m
Duration	1-2 Minutes

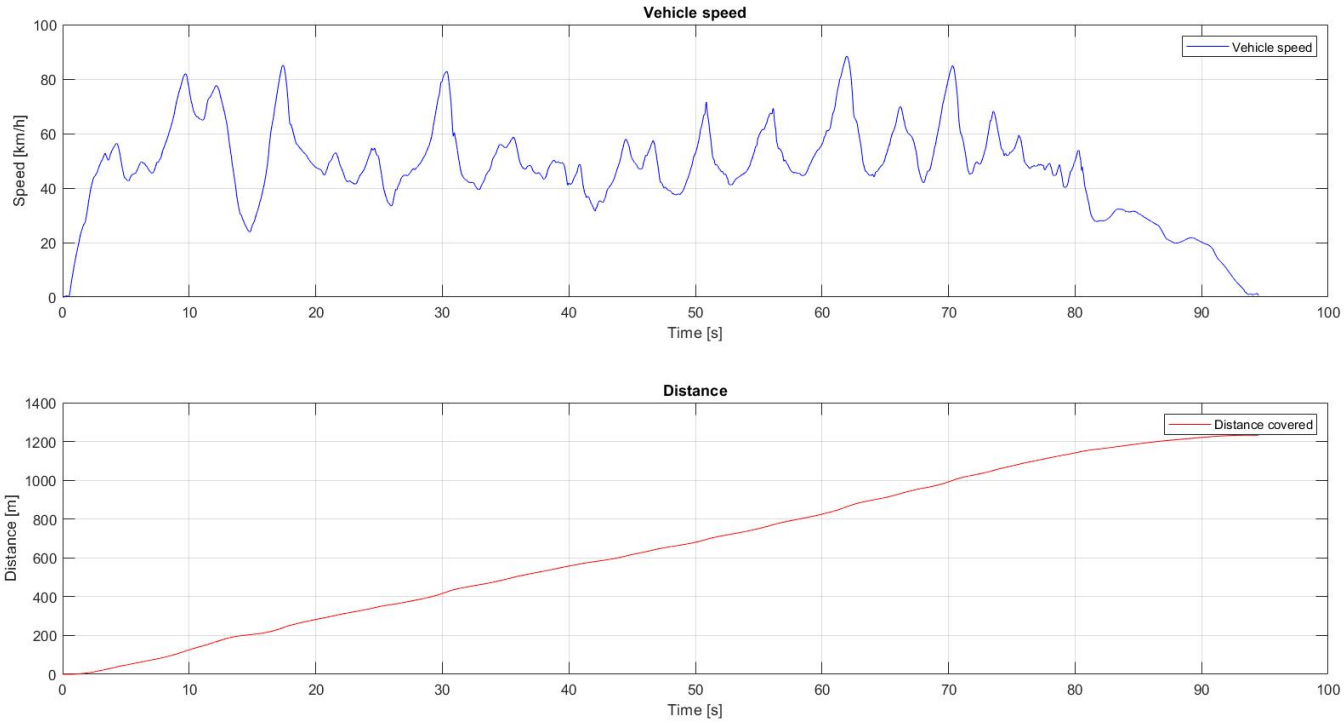

Figure 7: Speed and distance plots from one lap of the 2016 FSG autocross run

2.3.2 Acceleration

The acceleration event is a timed straight line drive from a standing start. The track specification is shown in Table 3. This event will require the largest instantaneous power from the tractive system (TS) since the car will reach a velocity where the maximum power can be extracted without losing traction on the wheels. The car will also reach its maximum speed during the acceleration event as seen in Figure 8, which shows logged data fron a typical acceleration event.

Table 3: Acceleration track layout rules and event specification [1]

Track specification	
Length	75 m
Track width	$\geq$ 5 m
Duration	4-7 Seconds

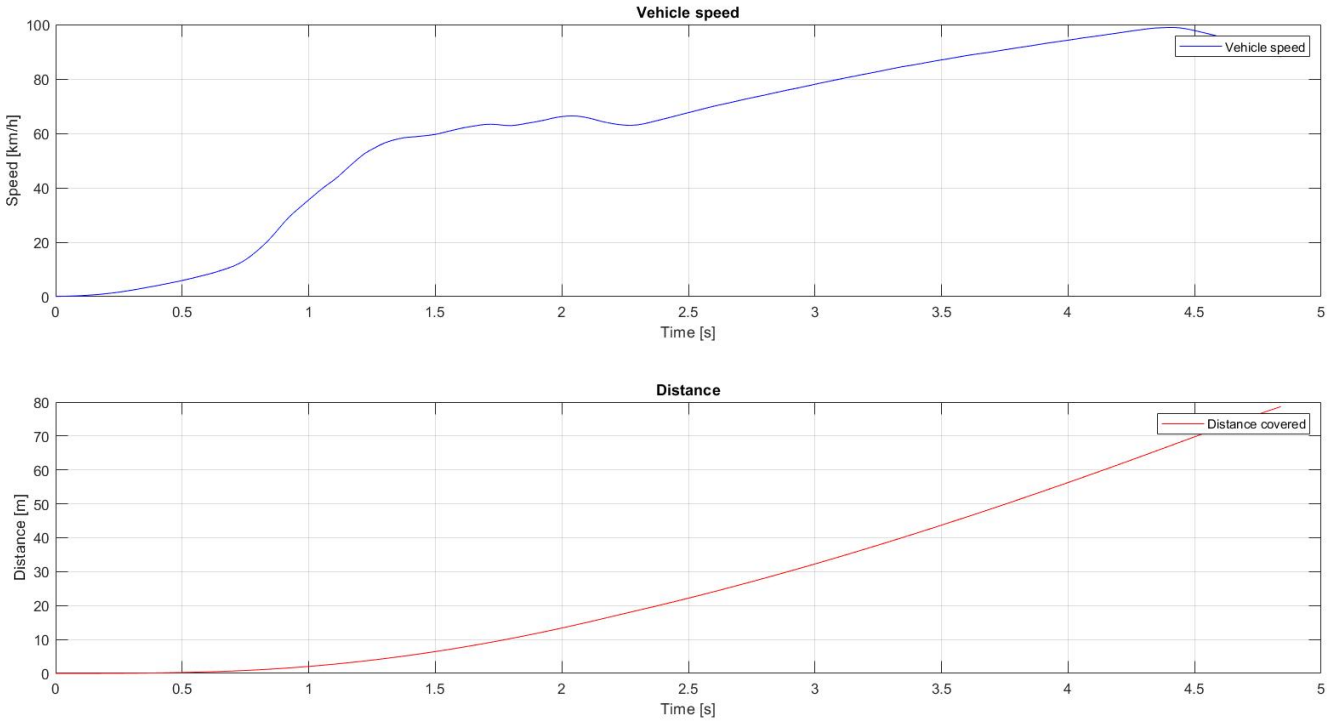

Figure 8: Speed and distance plots from the 2019 FSAC acceleration run

2.3.3 Endurance

The endurance event is a 22 km event where the track is approximately 1 km. At the midpoint of the event, the driver must be changed [1]. The track layout is specified in Table 4 and in Figure 9, the characteristics for half of a typical endurance run is shown where it should be noted that the speed characteristics is similar to that of the autocross event, but the duration of the event is much longer.

Table 4: Endurance track layout and specification [1]

Track specification	
Distance	$2 \cdot 11$ km
Straights	≥ 80 m
Constant turn diameter	≥ 50 m
Hairpin turn outside diameter	≥ 9 m
Slaloms	7.5-12 m cone spacing
Track width	≥ 3 m
Duration	25-30 Minutes

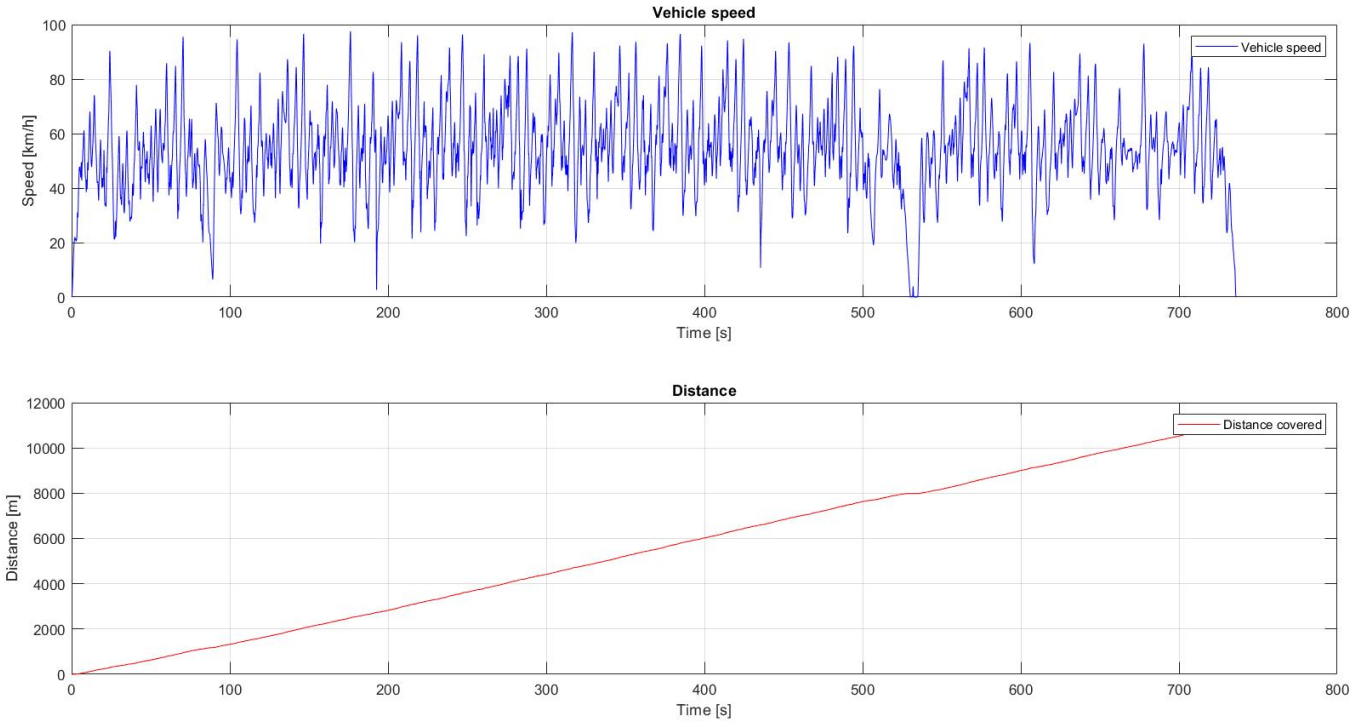

Figure 9: Speed and distance plots from the 2018 FSG endurance run

3 PMSM design theory

This chapter is a summary of the basic PMSM practical and theoretical knowledge required in order to understand the design of the PMSM. If the reader is familiar with PMSM design, this chapter can be skipped. The PMSM consist of two main components, the stator and the rotor which are shown in Figure 10.

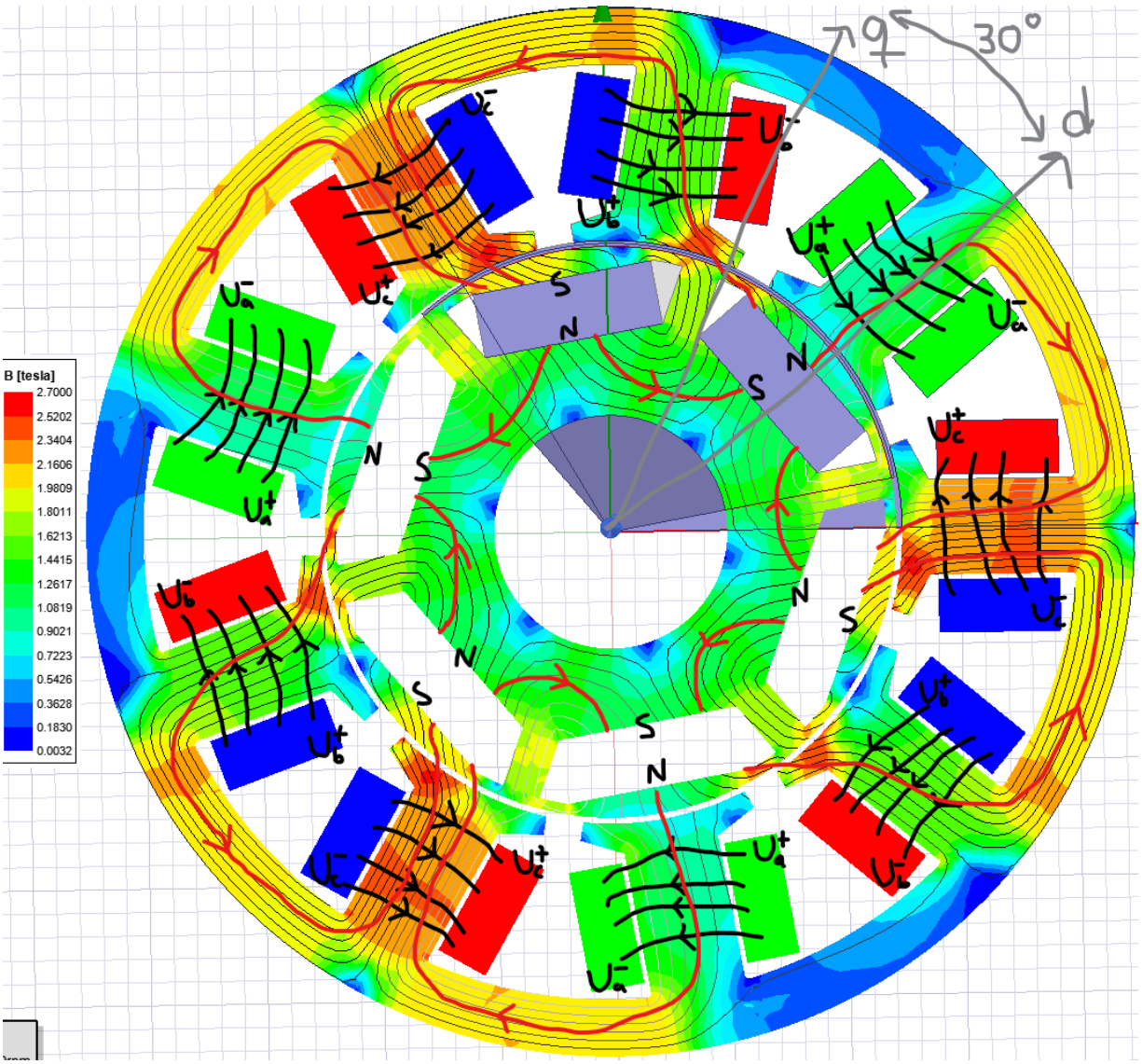

Figure 10: Two-dimensional model of a PMSM where the coil windings are drawn, flux density plotted and flux lines plotted

Inside the stator of a PMSM there are several stator teeth which coated copper wires are wound around. The coating of the wires is there to isolate them from each other so that a turn does not short circuit. The stator material is usually a type of iron alloy known as a ferromagnetic material and when a conductor is wound around the stator and current flows through it, a magnetic field will be generated. There are magnets mounted in the rotor which generates a magnetic field inside the motor.

During operation there are two "separate" magnetic fields inside the PMSM, one is generated by the rotor as previously mentioned and the second one is generated by the alternating 3-phase currents in the stator windings. During steady state, the magnetic field generated by the rotor will lock with the rotating magnetic field of the stator and hence synchronous speed is achieved [6].

3.1 PMSM magnetic circuit

In order to understand the fundamentals of PMSM design and the content of the thesis, the basic principles of electromagnetism should be covered. This section will show the relationship between how a current flowing through a coil will create a magnetic flux which will both generate a torque and an electromotive force in the copper wires. When studying the magnetic circuit in a PMSM, a single coil from Figure 10 will be considered as seen in Figure 11, more coils and magnets will be considered later.

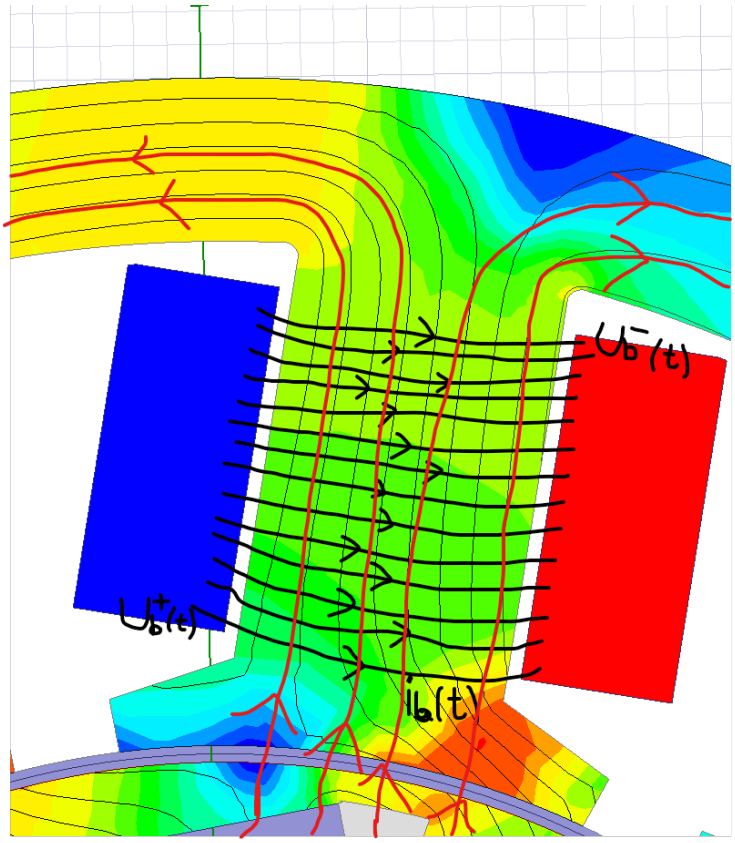

Figure 11: One coil from the PMSM model where phase b is wound around one stator tooth and the red lines represent the magnetic flux

3.1.1 Magnetic field strength and magnetomotive force(MMF)

According to Amperes law on integral form which relates the current passing through a conductor with surface area S to the magnetic field strength passing through an enclosed loop crossing the conductor [7], [6]. The enclosed loop of magnetic field strength is also known as magnetomotive force (MMF). The enclosed loop can be seen in Figure 10 where the red lines indicate this loop. The relationship is described according to

$$\mathcal{F} = \oint_l H\, dl = \int_s J dS = I_{enc} = \sum i(t) \tag{23}$$

where:

- $\mathcal{F}$ is the MMF $[A_{Turn}]$
- H is the magnetic field strength $[A/m]$
- J is the surface current density $[A/m^2]$
- I_{enc} is the enclosed current $[A]$
- $i(t)$ is the conductor current $[A]$

The MFF is required in order to create a magnetic flux. In order to illustrate the generation of MFF by having an electric current flow through a conductor wound into a coil, Amperes law on integration form in (23) is used and is expressed as

$$\mathcal{F} = \oint_l H\, dl = N \cdot i(t) \tag{24}$$

where N is the number of turns in the coil [6]. The MMF will generate a magnetic flux since there will always be a closed magnetic circuit. The magnitude of the flux generated is determined by the reluctance of the magnetic circuit [8], [7].

3.1.2 Reluctance

Reluctance is the magnetic circuit theory equivalent to resistance in electric circuit theory. It describes how easily the magnetic flux will flow through the specific material. The relationship between magnetic flux and reluctance is called Hopkinson's law [7] and is in the case of a PMSM described with

$$\mathcal{F} = \Phi \cdot \Re_{PMSM} \tag{25}$$

where:

- Φ is the magnetic flux $[Wb]$
- $\Re_{PMSM}$ is the total reluctance in the flux path in the PMSM $[H^{-1}]$

The reluctance of a uniform solid is determined by its relative permeability of the specific material, the cross-section area of the flux path and the length of the flux path [8]. In order to reduce the reluctance of a magnetic circuit there are three changes that can be made. Either reduce the length of the flux path, increase the cross-sectional area of the flux path or change material to one with a higher permeability. If the flux path is non-uniform as seen in Figure 10 where the cross-section area of the flux path will vary, the total reluctance can be calculated by summing up the reluctance of the different parts of the flux path [7], [6]. The total reluctance in the machine will consist of the stator core, rotor core and the air gap which is crossed twice. For a PMSM the total reluctance is calculated as

$$\Re_{PMSM} = \sum_{i=1}^{n} \Re_i = \sum_{i=1}^{n} \frac{l_{\Phi,i}}{\mu_0 \mu_r A_i} \tag{26}$$

where:

- $\Re_i$ is a partial reluctance in the magnetic circuit of the PMSM $[H^{-1}]$
- $l_{\phi,i}$ is a partial length of the flux path $[m]$
- A_i is a partial cross-section area of the flux path in the PMSM $[m^2]$
- μ_0 is the permeability in vacuum $[H/m]$

The materials often used in magnetic circuits are called soft iron materials and has a very high relative permeability under certain operating conditions. This will be covered in Section 4.1.4.

3.1.3 Magnetic flux

In any magnetic circuit where a MFF is generated, there will be a magnetic flux which will pass through an enclosed loop. That means that there will be no conservation of magnetic flux within the loop. That is described with Gauss law on integral form for magnetic flux density which states that the net flux through a closed surface is always equal to zero [7] which is expressed as

$$0 = \oint_s B \, ds \tag{27}$$

where B $[T]$ is the magnetic flux density and in practice it means that the flux entering a certain surface also must leave it. That means that for an arbitrary surface area, the total flux can be approximated to

$$\Phi = B \cdot A \tag{28}$$

assuming that the flux distribution is even across the surface. By combining (24), (26) and (25), the flux can be written as

$$\Phi = \frac{N \cdot I}{\sum_{i=1}^{n} \frac{l_i}{\mu_0 \mu_i \cdot A}} \tag{29}$$

where it can be seen that the flux is determined by the current, the number of turns and the reluctance of the fluxpath. Equation (29) describes how the flux is affected by the current magnitude and number of turns for a given magnetic circuit which is composed of a series of reluctances.

3.1.4 Permanent magnets

Permanent magnets act as "batteries" in a magnetic circuit and hence is a source of MMF. The MFF produced by a given magnet is calculated as

$$\mathcal{F} = H_{mag} \cdot t_{mag} = \Phi_{mag} \cdot \Re_{mag} \tag{30}$$

where:

- H_{mag} is the coectivity of the magnet $[A/m]$
- t_{mag} is the magnet thickness $[m]$
- Φ_{mag} is the flux produced by the magnet $[Wb]$
- $\Re_{mag}$ is the magnet reluctance $[H^{-1}]$

The magnet reluctance depends on the magnet width, stack length and magnet remanence. The reluctance is of the magnet can be calculated using

$$\Re_{mag} = B_r \cdot A_{mag} = B_r \cdot W_{mag} \cdot L_{stack} \tag{31}$$

where:

- B_r is the magnet remanence $[T]$
- A_{mag} is the cross-section area of the magnet $[m^2]$
- W_{mag} is the magnet width $[m]$
- L_{stack} is the stator lamination stack length $[m]$

In PMSMs, there are several types of magnets that can be used. There are rare earth magnets such as NdFeB, SmCo and AlNiCo. These magnets require mining and can only be found on certain places on the planet. Ferrites is an alternative to permanent magnets but according to [9], the use of ferrites will lead to a decrease in efficiency by about 1 %. They will also require a higher number of turns in the stator core due to a reduction in magnet flux in order to maintain the same performance. With a larger number of stator turns, there will be a risk of having large leakage inductance and hence the torque output may be compromised [9].

Rare earth magnets will demagnetize at high temperatures which means that their magnetic properties will be reduced permanently. The energy density of the NdFeB magnets is reduced at higher temperatures and hence the losses will increase [10]. At temperatures which are above ambient but below the temperature where the magnets demagnetize, it can be observed that there can be some temporary demagnetization which could increase losses [10].

When producing the magnets, there are mainly two methods used to form the magnets. There are sintering and there is bonding of the magnets. Sintering is a manufacturing method where the material is formed into one solid magnet by heating the material up to a high temperature but below the melting temperature of the material. Magnets can also be formed using different types of bonding which offers a higher flexibility in terms of shaping the material. The choice of manufacturing method can affect the magnetic properties of the magnets and its thermal behaviour.

3.1.5 Faraday's law of induction, EMF and flux linkage

When a magnetic flux passes through a surface enclosed by a conductor, the induced voltage is equal to the negative line integral of the electric field along an enclosing line on the surface. That line integral of the electric field strength will according to

$$U = \oint_l E \, dl \tag{32}$$

be equal to the induced voltage or electromotive force (EMF). By replacing flux with (29), the two "changes" that can be used to induce a voltage can be seen as either changing the surface area or changing the magnetic flux density. When having a coil as in Figure 11 it is useful to introduce the term flux linkage which is defined as the level of flux multiplied with the number of coil turn. The relationship between the back EMF and the flux linkage is described as

$$N\frac{d\Phi}{dt} = -\frac{d\Psi}{dt} = -\int_l E \, dl = -e = B\frac{dA}{dt} + A\frac{dB}{dt} \tag{33}$$

where:

- e is the back EMF $[V]$
- N is the number of turns
- Ψ is the flux linkage $[Wb]$

The definition of inductance is the ratio between the current and the flux linkage. In an electric machine there are several coils as seen in Figure 10 which produce flux linkage, which means that there are two sources of flux which can produce inductance in each coil. The inductance produced by the flux linkage that the coil itself produces is called self-inductance whilst the inductance produced from flux linkage from other coils is called mutual inductance. When having a coil wound around a core there will always be some leakage flux present caused by the airgap between the strands and the core. The leakage flux is denoted Φ_l and the main flux is denoted Φ_m. Hence the inductance for a single coil can be described according to (34), which also can be described in terms of number of turns and reluctance as

$$L = L_l + L_m = \frac{\Psi}{i} = \frac{\Psi_l}{i} + \frac{\Psi_m}{i} = \frac{N^2}{\Re} \tag{34}$$

where:

- L is the total coil inductance $[H]$.
- L_l is the inductance caused by the leakage flux $[H]$.
- L_m is the inductance caused by the main flux $[H]$.

3.2 Analytical model of the PMSM

This section will contain the electric, magnetic and mechanical modelling of the PMSM and show how the machine converts the applied phase voltage and the load torque into the phase currents, output torque and rotational speed of the machine.

3.2.1 Electric model

As seen in Figure 10 there are 9 coils in the machine and since there are three phases, there will be three coils per phase. The three phase voltages can all be written on the following format as

$$U_a = U_{conv} sin(\omega t) = R_a i_a + \frac{d(\Psi_a(t))}{dt} \tag{35}$$

$$U_b = U_{conv} sin(\omega t + \frac{2\pi}{3}) = R_b i_b + \frac{d(\Psi_b(t))}{dt} \tag{36}$$

$$U_c = U_{conv} sin(\omega t - \frac{2\pi}{3}) = R_c i_c + \frac{d(\Psi_c(t))}{dt} \tag{37}$$

where:

- U_a is the voltage in phase a $[V]$
- U_b is the voltage in phase b $[V]$
- U_c is the phase voltage in phase c $[V]$
- U_{conv} is the voltage magnitude from the converter $[V]$
- R_a is the resistance in phase a $[\Omega]$
- R_b is the resistance in phase b $[\Omega]$
- R_c is the resistance in phase c $[\Omega]$
- Ψ_a is the total flux linkage in phase a $[Wb]$
- Ψ_b is the total flux linkage in phase b $[Wb]$
- Ψ_c is the total flux linkage in phase c $[Wb]$

When studying electrical machines, the use of a rotating coordinate system is common in order to be able to model the rotor flux as DC. The reason for this is that it will simplify the dynamic model of the PMSM [11]. In order to change the coordinate system Park transformation which is also known as DQ-transformation is used and a transformation matrix is used [11] [12]

$$\begin{bmatrix} A_d \\ A_q \end{bmatrix} = \begin{bmatrix} cos(\Theta) & cos(\Theta - \frac{2\pi}{3}) & cos(\Theta + \frac{2\pi}{3}) \\ -sin(\Theta) & -sin(\Theta - \frac{2\pi}{3}) & -sin(\Theta + \frac{2\pi}{3}) \end{bmatrix} \begin{bmatrix} A_a \\ A_b \\ A_c \end{bmatrix} \tag{38}$$

where Θ is the transformation angle.

In order to model the PMSM in the dq-coordinate system, the voltages are re-written on matrix form as

$$\begin{bmatrix} U_a \\ U_b \\ U_c \end{bmatrix} = \begin{bmatrix} R_s i_a + \frac{d(\Psi_a)}{dt} \\ R_s i_b + \frac{d(\Psi_b)}{dt} \\ R_s i_c + \frac{d(\Psi_c)}{dt} \end{bmatrix} \tag{39}$$

where it is assumed that they have the same phase resistance which is denoted as R_s [Ω]. When performing dq-transformation on the PMSM model, the direction of the d-axis is defined as the direction of the rotor flux as can be seen in Figure 10. Hence the transformation angle should be selected to the angle between the d-axis and the phasor from phase a [11]. That in practice means that the transformation angle will be equal to that of the rotor position relative to phase a and as such, the angle Θ should be selected as the rotor angle θ_r. Now performing the transformation on the phase voltages as

$$\begin{bmatrix} U_d \\ U_q \end{bmatrix} = \begin{bmatrix} cos(\Theta) & cos(\Theta - \frac{2\pi}{3}) & cos(\Theta + \frac{2\pi}{3}) \\ -sin(\Theta) & -sin(\Theta - \frac{2\pi}{3}) & -sin(\Theta + \frac{2\pi}{3}) \end{bmatrix} \begin{bmatrix} R_s i_a + \frac{d(\Psi_a)}{dt} \\ R_s i_b + \frac{d(\Psi_b)}{dt} \\ R_s i_c + \frac{d(\Psi_c)}{dt} \end{bmatrix} \tag{40}$$

which gives

$$U_d = (R_s i_a + \frac{d(\Psi_a)}{dt})cos(\theta_r) + (R_s i_b + \frac{d(\Psi_b)}{dt})cos(\theta_r - \frac{2\pi}{3}) + (R_s i_c + \frac{d(\Psi_c)}{dt})cos(\theta_r + \frac{2\pi}{3}) \tag{41}$$

$$U_q = -(R_s i_a + \frac{d(\Psi_a)}{dt})sin(\theta_r) - (R_s i_b + \frac{d(\Psi_b)}{dt})sin(\theta_r - \frac{2\pi}{3}) - (R_s i_c + \frac{d(\Psi_c)}{dt})sin(\theta_r + \frac{2\pi}{3}) \tag{42}$$

Equation (41) and (42) is then re-written as

$$\begin{aligned} U_d = R_s(i_a cos(\theta_r) + i_b cos(\theta_r - \frac{2\pi}{3}) + i_c cos(\theta_r + \frac{2\pi}{3})) + \\ + \frac{d(\Psi_a)}{dt} cos(\theta_r) + \frac{d(\Psi_b)}{dt} cos(\theta_r - \frac{2\pi}{3}) + \frac{d(\Psi_c)}{dt} cos(\theta_r + \frac{2\pi}{3}) \end{aligned} \tag{43}$$

$$\begin{aligned} U_q = -R_s(i_a sin(\theta_r) + i_b sin(\theta_r - \frac{2\pi}{3}) + i_c sin(\theta_r + \frac{2\pi}{3})) + \\ - \frac{d(\Psi_a)}{dt} sin(\theta_r) - \frac{d(\Psi_b)}{dt} sin(\theta_r - \frac{2\pi}{3}) - \frac{d(\Psi_c)}{dt} sin(\theta_r + \frac{2\pi}{3}) \end{aligned} \tag{44}$$

From (43) and (44), it can be noted that the voltages in dq-frame can be expressed in terms of d- and q-axis flux linkages and currents. It should also be noted that there is a time dependence on the rotor position and hence should be accounted for in the derivatives. Hence the following expression is obtained

$$U_d = R_s i_d + \frac{d\Psi_d}{dt} - \omega_r(\Psi_a sin(\theta_r) + \Psi_b sin(\theta_r - \frac{2\pi}{3}) + \Psi_b sin(\theta_r + \frac{2\pi}{3})) =$$

$$= R_s i_d + \frac{d\Psi_d}{dt} - \omega_r \Psi_q \tag{45}$$

$$U_q = R_s i_q + \frac{d\Psi_q}{dt} + \omega_r(\Psi_a cos(\theta_r) + \Psi_b cos(\theta_r - \frac{2\pi}{3}) + \Psi_b cos(\theta_r + \frac{2\pi}{3})) =$$

$$= R_s i_q + \frac{d\Psi_q}{dt} + \omega_r \Psi_d \tag{46}$$

where ω_r is the time derivative of the rotor angle.

3.2.2 Magnetic model

As mentioned in Section 3.1.5, the total flux linkage in a coil consists of several components. In the case of the PMSM the flux linkage has four components. That is the flux linkage from the coil itself, the two adjacent coils and the permanent magnet [13] [11]. The flux linkage can be modelled in terms of self-inductance, mutual inductance and magnet flux linkage and can be written as

$$\Psi = (L_s + L_{m1} + L_{m2})i + \Psi_{PM} \tag{47}$$

where L_{m1} $[H]$ is the mutual inductance from the first of the two adjacent coils and L_{m2} $[H]$ is the mutual inductance from the second coil. For the three phase PMSM, the phase flux linkages will be expressed as

$$\begin{bmatrix} \Psi_a \\ \Psi_b \\ \Psi_c \end{bmatrix} = \begin{bmatrix} L_a i_a + \Psi_{PM} cos(\theta_r) \\ L_b i_b + \Psi_{PM} cos(\theta_r - \frac{2\pi}{3}) \\ L_c i_c + \Psi_{PM} cos(\theta_r + \frac{2\pi}{3}) \end{bmatrix} \tag{48}$$

The inductance components are then also expressed on matrix form as

$$L_{matrix} = \begin{bmatrix} L_a \\ L_b \\ L_c \end{bmatrix} = \begin{bmatrix} l_{aa} & l_{ab} & l_{ac} \\ l_{ba} & l_{bb} & l_{bc} \\ l_{ca} & l_{cb} & l_{cc} \end{bmatrix} \tag{49}$$

where:

- L_a is the inductance in phase a $[H]$
- L_b is the inductance in phase b $[H]$
- L_c is the inductance in phase c $[H]$
- l_{aa} is the self-inductance of phase a $[H]$
- l_{bb} is the self-inductance of phase b $[H]$
- l_{cc} is the self-inductance of phase c $[H]$
- l_{ba} is the mutual inductance in phase b caused by phase a $[H]$
- l_{ca} is the mutual inductance in phase c caused by phase a $[H]$
- l_{ab} is the mutual inductance in phase a caused by phase b $[H]$

- l_{ac} is the mutual inductance in phase a caused by phase c $[H]$
- l_{cb} is the mutual inductance in phase c caused by phase b $[H]$
- l_{bc} is the mutual inductance in phase b caused by phase a $[H]$

The mutual and self-inductances themselves consist of several components which are caused by the different harmonics of the flux and is calculated according to [14]

$$l_{aa} = L_{aa0} + L_{aa2}cos(2\theta_r) \tag{50}$$

$$l_{bb} = L_{aa0} + L_{aa2}cos(2(\theta_r - \frac{2\pi}{3})) \tag{51}$$

$$l_{cc} = L_{aa0} + L_{aa2}cos(2(\theta_r + \frac{2\pi}{3})) \tag{52}$$

$$l_{ab} = L_{ba} = -[L_{ab0} + L_{aa2}cos(2(\theta_r + \frac{\pi}{6}))] \tag{53}$$

$$l_{bc} = L_{cb} = -[L_{ab0} + L_{aa2}cos(2(\theta_r + \frac{\pi}{2}))] \tag{54}$$

$$l_{ac} = L_{ca} = -[L_{ab0} + L_{aa2}cos(2(\theta_r + \frac{5\pi}{6}))] \tag{55}$$

where:

- L_{aa0} is the fundamental harmonic of the self-inductance in phase a $[H]$
- L_{aa2} is the second order harmonic of the self-inductance in phase a $[H]$
- L_{ab0} is the fundamental harmonic of the mutual inductance between phase a and b $[H]$

Now the equations are inserted into the inductance matrix described in (49) as

$$L_{matrix} =$$

$$\begin{bmatrix} [L_{aa0} + L_{aa2}cos(2\theta_r)] & -[L_{ab0} + L_{aa2}cos(2(\theta_r + \frac{\pi}{6}))] & -[L_{ab0} + L_{aa2}cos(2(\theta_r + \frac{5\pi}{6}))] \\ -[L_{ab0} + L_{aa2}cos(2(\theta_r + \frac{\pi}{6}))] & [L_{aa0} + L_{aa2}cos(2(\theta_r - \frac{2\pi}{3}))] & -[L_{ab0} + L_{aa2}cos(2(\theta_r - \frac{\pi}{2}))] \\ -[L_{ab0} + L_{aa2}cos(2(\theta_r + \frac{5\pi}{6}))] & -[L_{ab0} + L_{aa2}cos(2(\theta_- \frac{\pi}{2}))] & [L_{aa0} + L_{aa2}cos(2(\theta_r + \frac{2\pi}{3}))] \end{bmatrix} \tag{56}$$

The flux linkages in the machine can now be expressed in terms of inductance harmonics and phase currents according to

$$\Psi_a = (L_{aa0} + L_{ab_0} + \frac{3}{2}L_{aa2}cos(2\theta_r))i_a + \frac{\sqrt{3}}{2}L_{aa2}sin(2\theta_r)(i_b - i_c) + \Psi_{PM}cos(\theta_r) \tag{57}$$

$$\Psi_b = (L_{aa0} + L_{ab_0} + \frac{3}{2}L_{aa2}cos(2(\theta_r - \frac{2\pi}{3})))i_b + \frac{\sqrt{3}}{2}L_{aa2}sin(2(\theta_r - \frac{2\pi}{3}))(i_c - i_a) + \Psi_{PM}cos(\theta_r - \frac{2\pi}{3}) \tag{58}$$

$$\Psi_c = (L_{aa0} + L_{ab_0} + \frac{3}{2}L_{aa2}cos(2(\theta_r + \frac{2\pi}{3})))i_c + \frac{\sqrt{3}}{2}L_{aa2}sin(2(\theta_r + \frac{2\pi}{3}))(i_a - i_b) + \Psi_{PM}cos(\theta_r + \frac{2\pi}{3}) \tag{59}$$

which will be used to derive the flux linkages in dq-frame.

Now Parks transformation is used

$$\begin{bmatrix}\Psi_d\\ \Psi_q\end{bmatrix} = \begin{bmatrix} cos(\theta_r) & cos(\theta_r - \frac{2\pi}{3}) & cos(\theta_r + \frac{2\pi}{3}) \\ -sin(\theta_r) & -sin(\theta_r - \frac{2\pi}{3}) & -sin(\theta_r + \frac{2\pi}{3}) \end{bmatrix} \begin{bmatrix}\Psi_a\\ \Psi_b\\ \Psi_c\end{bmatrix} \tag{60}$$

to obtain the d- and q-axis flux linkages and placing the d-axis in the direction of the rotor flux [12] [11]. The d- and q-axis flux linkages is now expressed as

$$\Psi_d = (L_{aa0} + L_{ab0} + \frac{3}{2}L_{aa2})i_d + \Psi_{PM} \tag{61}$$

$$\Psi_q = (L_{aa0} + L_{ab0} - \frac{3}{2}L_{aa2})i_q \tag{62}$$

and hence the inductance's can be re-written as

$$L_d = L_{aa0} + L_{ab0} + \frac{3}{2}L_{aa2} \tag{63}$$

$$L_q = L_{aa0} + L_{ab0} - \frac{3}{2}L_{aa2} \tag{64}$$

where it can be noted that the second order harmonic of the self-inductance is the difference between the d- and q- axis inductances [11]. Now the expressions for the d- and q- flux linkages can be inserted into (45) and (46) and expressed in terms of inductance which gives

$$U_d = R_s i_d + L_d \frac{di_d}{dt} - \omega_r L_q i_q \tag{65}$$

$$U_q = R_s i_q + L_s \frac{di_q}{dt} + \omega_r L_d i_d + \omega_r \Psi_{PM} \tag{66}$$

3.2.3 Mechanical model

The output power from a PMSM is the output torque multiplied with the mechanical speed and is also equal to the input electric power minus the copper losses if it can be assumed that the other losses (iron, magnet, bearing,...) losses are small. Hence the following equation is obtained.

$$P_{PMSM} = T_{PMSM}\omega_{PMSM} = \frac{T_{PMSM}\omega_e}{p} \tag{67}$$

where p is the number of poles in the machine. A pole pair in a machine can be explained as one magnetic circuit in which flux will flow. If the machine has several pole pairs, that can be visualized as several magnetic circuits connected in parallel. These magnetic circuits will all contribute to the total flux produced in the machine and each magnetic circuit has their own MMF source. For the mechanical model of the machine that means that the torque will have a linear dependency of the number of pole pairs. The relationship between the mechanical and electric speed will also be influenced according to (67). When deriving the equation used to model the PMSM torque, Clarke transformation is used where a three-phase system is transformed into a two-phase system. This type of transformation is also known as $\alpha\beta$-transformation. The transformation matrix is defined as [15]

$$\begin{bmatrix}S_\alpha\\ S_\beta\end{bmatrix} = K \begin{bmatrix} \frac{2}{3} & -\frac{1}{3} & -\frac{1}{3} \\ 0 & \frac{1}{\sqrt{(3)}} & -\frac{1}{\sqrt{(3)}}) \end{bmatrix} \begin{bmatrix}S_a\\ S_b\\ S_c\end{bmatrix} \tag{68}$$

where K is the scaling constant. The scaling constant will determine what the relationship between the abc-frame and the $\alpha\beta$-frame. If K=1, the transformation will be amplitude invariant which means that the amplitudes will be the same in the two frames.

The $\alpha\beta$-frame is a stationary frame which means that the coordinate system does not rotate which it does in dq-frame. One can transform from $\alpha\beta$-frame to dq-frame using the Euler formula as [11]

$$A_{dq} = e^{-j\Theta} S_{\alpha\beta} \tag{69}$$

Where:

- $A_{dq} = A_d + jA_q$
- $S_{\alpha\beta} = S_\alpha + jS_\beta$

The electric active power P_e $[W]$ is the input power of the machine and is calculated using

$$P_e(t) = U_a(t)i_a(t) + U_b(t)i_b(t) + U_c(t)i_c(t) = \begin{bmatrix} U_a(t) & U_b(t) & U_c(t) \end{bmatrix} \begin{bmatrix} i_a(t) \\ i_b(t) \\ i_c(t) \end{bmatrix} = \tag{70}$$

$$= \begin{bmatrix} U_\alpha(t) & U_\beta(t) \end{bmatrix} \Lambda^{-1^T} \Lambda^{-1} \begin{bmatrix} i_\alpha(t) \\ i_\beta(t) \end{bmatrix} = \frac{3}{2k^2} \begin{bmatrix} U_\alpha(t) & U_\beta(t) \end{bmatrix} \begin{bmatrix} i_\alpha(t) \\ i_\beta(t) \end{bmatrix} = \tag{71}$$

$$= \frac{3}{2k^2}(U_\alpha(t)i_\alpha(t) + U_\beta(t)i_\beta(t)) = ReU_s I_s^* \tag{72}$$

where:

- Λ^{-1} is the inverse Clarke transformation matrix which is expressed as

$$\begin{bmatrix} S_a \\ S_b \\ S_c \end{bmatrix} = \frac{1}{K} \begin{bmatrix} 1 & 0 \\ -\frac{1}{2} & \frac{\sqrt{3}}{2} \\ -\frac{1}{2} & -\frac{\sqrt{3}}{2} \end{bmatrix} \begin{bmatrix} S_\alpha \\ S_\beta \end{bmatrix} = \Lambda^{-1} \begin{bmatrix} S_\alpha \\ S_\beta \end{bmatrix} \tag{73}$$

- U_s is the stationary frame two phase equivalent voltage [V] and is expressed as

$$U_S = U_\alpha(t) + jU_\beta(t) \tag{74}$$

- I_s is the stationary frame two phase equivalent current [A] and is expressed as

$$I_S = I_\alpha(t) + jI_\beta(t) \tag{75}$$

Now combining (70) and (67) and using amplitude invariant transformation, the torque of the PMSM is expressed as

$$T_{PMSM} = \frac{3p}{2\omega_r K^2} Re((U_{s,a} - R_s I_s)I_s^*) = \frac{3p}{2\omega_r} Re(j\omega_r \Psi_s I_s^*) = \frac{3p}{2\omega_r} Im((L_d i_d + L_q i_q + \Psi_{PM})I_s^*$$

$$= \frac{3p}{2\omega_r} Im((L_d i_d + jL_q i_q + \Psi_{PM})I_s^*) = \frac{3p}{2\omega_r} Im((L_d i_d + jL_q i_q)(i_d + ji_q) + \Psi_{PM} I_s)$$

Then the torque output from the PMSM can be written as

$$T_{PMSM} = \frac{3p}{2}(\Psi_d i_q - \Psi_q i_d) = \frac{3p}{2}(\Psi_{PM} i_q + ((L_d - L_q) i_q i_d)) \tag{76}$$

as described in [6] [16], [11]. When operating the machine in the car, there will be a load torque acting in the reverse direction of the rotating mass. The mechanical speed equation of the PMSM can be written as

$$J\frac{d\omega_{PMSM}}{dt} = T_{PMSM} - T_{load} \tag{77}$$

where:

- J is the machine inertia $[kgm^2]$
- T_{load} is the load torque $[Nm]$

3.2.4 Base speed and field weakening

The rated speed is defined as the speed at which the phase voltage has reached its rated value (maximum) and the back EMF in the motor has reached a level to completely level out the applied voltage. The back EMF depends on the flux magnitude and the speed of the machine according to (33). After reaching the base speed, the maximum power output from the motor will remain constant. At voltages below the rated voltage, the motor will operate at its maximum torque per Ampere (MTPA) angle but in order to reach speeds higher than the rated speed, the field in the machine must be reduced. In order to do that, a larger negative current in the d-axis must be applied as can be seen in (66) to reduce the effect of the back EMF, $\omega_r \Psi_{PM}$. The change in angle between the d- and q-axis current will cause the torque to drop due to no longer having the MTPA angle which shown in Figure 12 which a typical torque- and voltage-speed curves for a PMSM.

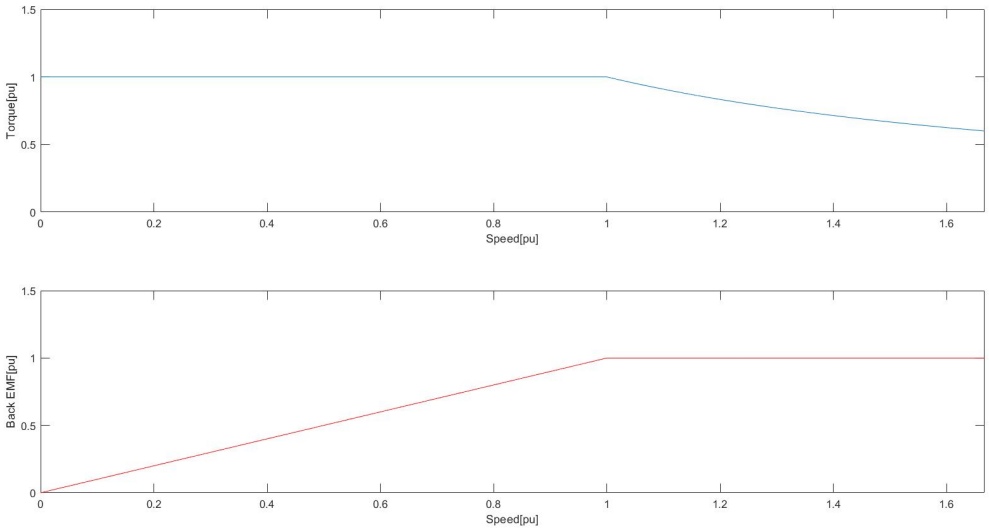

Figure 12: Torque-speed and voltage-speed curve of a PMSM in per-unit values

3.2.5 Maximum torque per Ampere(MTPA)

According to (76), for a given current amplitude I_{mag} there will be an angle β at which the maximum torque is achieved [11], [8]. That is called the MTPA angle which influences the currents according to

$$i_d = I_{mag} cos(\beta) \tag{78}$$

$$i_q = I_{mag} sin(\beta) \tag{79}$$

In order to obtain the current angle, (76) is re-written as

$$T_{PMSM} = \frac{3p}{2}(\Psi_{PM} I_{mag} sin(\beta) + (L_d - L_q) I_{mag}^2 \frac{1}{2} sin(2\beta)) \tag{80}$$

In order to find the maximum torque, the angle-derivative of the torque is set to zero and solved to the angle β

$$\frac{dT_{PMSM}}{d\beta} = \frac{3p}{2}(\Psi_{PM} I_{mag} cos(\beta) + (L_s - L_q) I_{mag}^2 cos(2\beta)) = 0 \tag{81}$$

$$cos(\beta) = -\frac{\Psi_{PM}}{4(L_d - L_q) I_{mag}} - \sqrt{\frac{1}{2} + (\frac{\Psi_{PM}}{4(L_d - L_q) I_{mag}})^2} \tag{82}$$

Now the current magnitude for a specific torque requirement can be calculated as

$$I_{mag} = -\frac{\Psi_{PM}}{2(L_d - L_q)cos(\beta)} + \sqrt{\frac{2}{3p(L_d - L_q)\frac{1}{2}sin(2\beta)}T_{emref} + (\frac{\Psi_m}{2(L_d - L_q)cos(\beta)})^2} \tag{83}$$

where this equation would later be used to calculate the current required to reach a certain torque in the FEM model [11]. The CFS17 motor is designed such that $L_q > L_d$ which means that the current will be in the second quadrant for positive torque and in the third quadrant for negative torque.

3.2.6 Losses

From an electro-magnetic point of view there are three types of losses in a PMSM. There are resistive copper losses in the windings, iron losses in the stator and rotor cores and magnet losses in the magnets. The two latter types of losses are caused by varying magnetic fields in the respective materials. The total resistive losses in a three-phase copper winding is calculated as

$$P_{Res} = 3 \cdot R_s \cdot I_{rms}^2 \tag{84}$$

but it does not however consider the fact that the type of current used is an alternating current (AC) and with that comes more losses. The reason for AC causing more losses is because of the charge distribution within the strands. The reason for this uneven distribution is the skin effect, proximity effect and the possible presence of circulating currents [17], [18]. As the frequency increases, the losses in the copper will increase.
Also, when approximating the losses in a PMSM the winding layout must be considered and especially the wire length. The resistance of a wire with length l_{wire} $[m]$ is calculated using

$$R_{20^o} = \rho_{copper,20^o}\frac{l_{wire}}{A_{wire}} \tag{85}$$

where $\rho_{copper,20^o}$ is the resistivity of copper at 20 degrees. The temperature dependence of a conductor must also be taken into account and is given by

$$R(T) = R_0(1 + \alpha_0(T - T_0)) \tag{86}$$

where:

- $R(T)$ is the resistance as a function of temperature $[\Omega]$
- R_0 is the calculated resistance at temperature T_0 $[\Omega]$
- T_0 is the temperature at which the original resistance is calculated. This is usually at ambient temperature. $[K]$
- α is the temperature coefficient of resistance which determines the rise in resistivity as the temperature increases
- T is the temperature of the material. $[K]$

The iron losses are difficult to calculate by hand. The iron losses consist of three main terms, hysteresis losses, Eddy current losses and excess losses. The hysteresis losses are described by the first term in the Bertotti equation. The second term is the Eddy current losses, and the third term is the excess losses [19]. The loss per kilogram in the iron core is calculated using the Bertotti equation as

$$P_{Fe/kg} = f_m P_0(B_{max}) + \pi^2 \sigma d^2 B_{max}^2 f_m^2/6 + 8\sqrt{\sigma G S V_0} B_{max}^{3/2} f_m^{3/2} \tag{87}$$

where:

- $P_{Fe/kg}$ is the iron losses per kilogram of weight $[W/kg]$
- P_0 is the per electric cycle hysteresis loss $[W/kg]$
- f_m is the magnetizing frequency $[Hz]$
- σ is the conductivity of the material $[S/m]$
- d is the lamination thickness $[m]$
- B_{max} is the peak flux density $[T]$
- G is the mobility coefficient $[m^2/(V \cdot s)]$
- S is the cross-section area of the lamination $[m^2]$
- V_0 is the material characteristic statistical distribution function of the coercive fields.

The FEM software uses this relationship but has different version of (87) which is more commonly used and is expressed as

$$P_{Fe/kg} = P_e + P_h + P_c \tag{88}$$

where:

- P_c is the Eddy current losses $[W]$
- P_e is the excess losses $[W]$
- P_h is the hysteresis losses $[W]$

These losses are then calculated as

$$P_c = k_c \cdot (B_{max} f_m)^2 \tag{89}$$

$$P_e = k_e \cdot (B_{max} f_m)^{1.5} \tag{90}$$

$$P_h = k_h \cdot B_{max}^{\beta_m} f_m \tag{91}$$

where:

- k_c is the Eddy current loss coefficient
- k_e is the excess loss coefficient
- k_h is the hysteresis loss coefficient
- β_m is a measured value that is material specific

When (91), (90) and (89) is applied in time domain, the excess and Eddy current losses is usually fairly accurate, but the hysteresis losses may not be [20].

4 Design and manufacturing considerations

This chapter will cover the practical design considerations which must be considered when designing a PMSM.

4.1 Stator winding and arrangement options

According to (29), the flux generated from the coils has a linear dependency on the current, if the permeability is unchanged. In an ideal case, the flux will behave as a sinusoidal waveform which means that the torque and back EMF will behave in the same way. As a certain flux passes through a coil, a back EMF will be induced according to (33). An increase in the number of turns will lead to an increase in the induced back EMF for a given flux. That means that the motor will enter field weakening at a lower speed provided that the maximum supply voltage is not increased.

There is a certain distance between the machine poles which is called the pole pitch [8], [16]. That is not to be confused with the angle between the poles which sometimes also is called pole pitch [6]. The pole pitch is defined as

$$y_p = \frac{N_{slot}}{N_{pole}} \tag{92}$$

The coil pitch is similar to pole pitch but for coils instead. It depends on the number of winding layers and if distributed or concentrated windings are used. There will be an offset α_a between the fundamental flux and the back EMF which depends on the number of phases and the slot per pole per phase number and is given by

$$\alpha_a = \frac{360}{2N_{phase}q} \tag{93}$$

This angle will influence the harmonics of the flux and the back EMF of the motor. The coil pitch is the distance that a coil will cover i.e. the distance covered by the end windings [8].

4.1.1 Number of turns per phase

In an electric machine there are generally two methods to increase the maximum torque of the machine at base speed. According to (76) an increase in the number of turns will lead to an increase in the torque given that the current remains fixed. The flux of the electric machine is limited due to the eventual saturation of the core whilst the number of turns is limited by the slot area. Also, when increasing the number of turns, the back EMF will increase according to (33). Given that the maximum supply voltage is fixed according to the FSG rules [1], having a too large back EMF will force the machine to enter field weakening at an earlier stage. Due to the winding layout in the CFS17 motor, the motor could experience some problems when entering field weakening. That will be discussed further in the next section. In order the to maintain the torque output of the motor, MMF of the motor should remain constant. That means keeping the number of turns multiplied with the current constant. That can be mathematically expressed as

$$\mathcal{F}_{coil} = N_{turn,phase} \cdot I \tag{94}$$

where $\mathcal{F}_{coil}$ is the coil MMF which is kept constant when re-designing the motor. In order to reduce the copper losses in the machine, the number of turns in the machine should be kept as high as possible to reduce the current needed to reach a certain torque. That is however assuming that the magnet flux will be unchanged which is not completely true unless the rotor layout is changed. Having a higher number of turns will however also lead to higher resistance in the coils and if the fill factor is to remain unchanged, the stator slot area has to be increased. Increasing the slot area could lead to an increase in iron losses due to a possible increase in stator reluctance.

4.1.2 Concentrated and distributed windings

There are two types of winding methods commonly used in PMSMs. Distributed windings and concentrated windings. Distributed windings mean that the one coil windings are not concentrated to a single stator tooth but is instead overlapping with other phases. A distributed winding layout is shown in Figure 14 which is a stator from an old induction machine. Concentrated windings mean that the windings are concentrated to one stator tooth. In Figure 13 the concentrated winding used in the CFS17 PMSM is shown. The main advantages of using concentrated windings are reduction of copper losses due to shorter length of the windings and weight reduction due to the shorter strands [21]. The power density is also higher for a motor with concentrated windings [22], [21]. According to [22] concentrated windings are commonly used for traction applications although that type of winding can cause problem with field weakening and motor flux control. Another problem with the use of concentrated windings was studied by [23], where it was concluded that the use of that arrangement caused an increase in Eddy current losses which was attributed to variations in flux density caused by the slot openings and the variations of flux path length due to the rotation of the rotor.

The problems in field weakening attributed to concentrated windings can lead to increased MMF harmonics which in turn could lead to increased losses in the rotor [24]. At high-speed operation, the possible increase in iron losses may outweigh the possible decrease in copper losses. However, if the losses in the rotor does not increase substantially and the losses mainly increase in the stator core, there could be beneficial effects in terms of cooling since it is generally easier to cool the stator core than the copper windings.

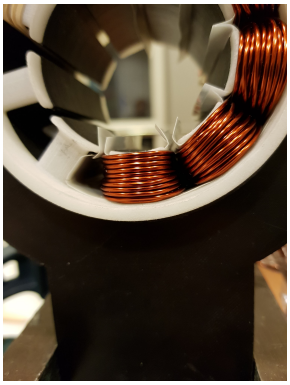

Figure 13: Concentrated winding used in the CFS17 PMSM where the insulating mylar sheets and 3D-printed end winding insulation also can be seen

Figure 14: Distributed windings, from an induction machine stator

4.1.3 Coil connection

As previously mentioned, the number of turns in the coil determines the torque and back EMF in the machine as well as the losses in copper wires. The losses are determined by the current and the wire resistance. In the CFS17 motor, the phase coils were all connected in parallel which means that the number of turns per coil had to be increased in order to obtain the correct number of turns per phase as compared to if they would have been connected in series. The main advantages of having the coils connected in parallel is that the current passing through each coil will be reduced and hence thinner wires can be used which makes the process of winding the stator easier. Such a connection is shown in Figure 15. Alternatively should the wire thickness not be reduced, the total phase resistance is reduced and the copper losses will decrease which could be desirable since a majority of the losses in a PMSM occurs in the windings.

However this requires as mentioned, a greater number of turns per coil and there is a risk of getting an imbalance in the motor due to varying coil inductance or resistance. The varying resistance could be caused by varying strand length in the different coils due to inconsistent windings and the variations in inductance could be caused by different number of turns on each coil. By connecting the coils in series as shown in Figure 14, both of the above-mentioned disadvantages are solved since the current will be the same through all of the coils and also there is less of a risk of having an unequal distribution of the MMF in the magnetic circuit. That is because the lower number of turns needed is lower compared to the parallel coils, the risk of miscounting is reduced. However, the current passing through each coil is increased so the strand size will need to be increased in order to reduce the resistance in the wires. Increasing the strand size will cause problems when winding the motor because the wires are more difficult to shape and package when winding the stator.

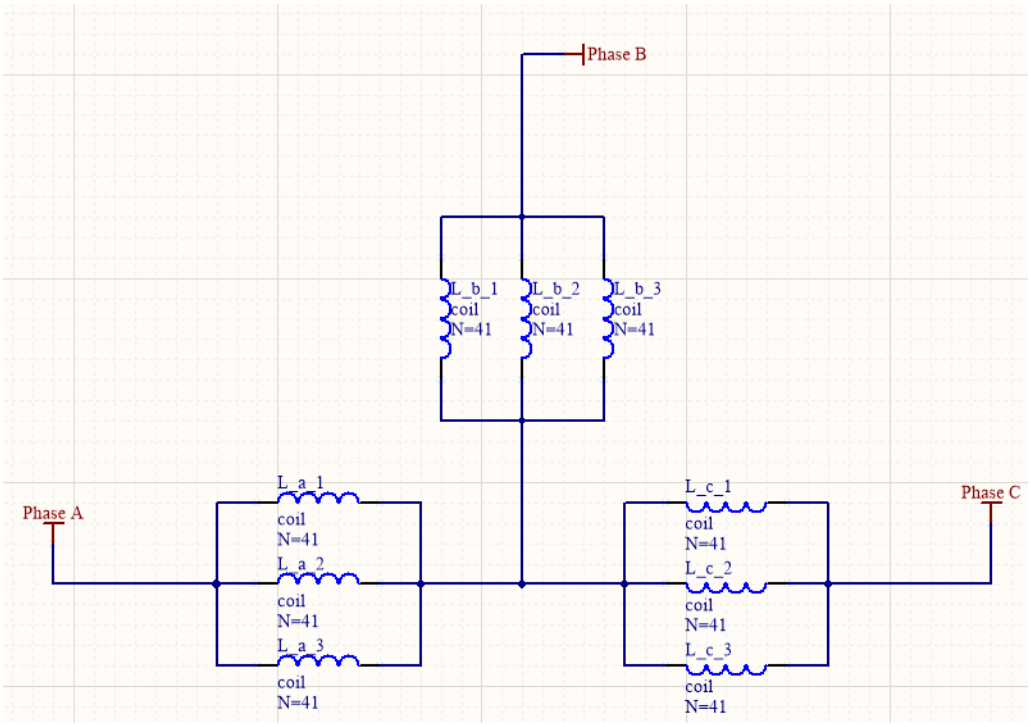

Figure 15: Equivalent circuit for the stator winding using parallel connection of the coils

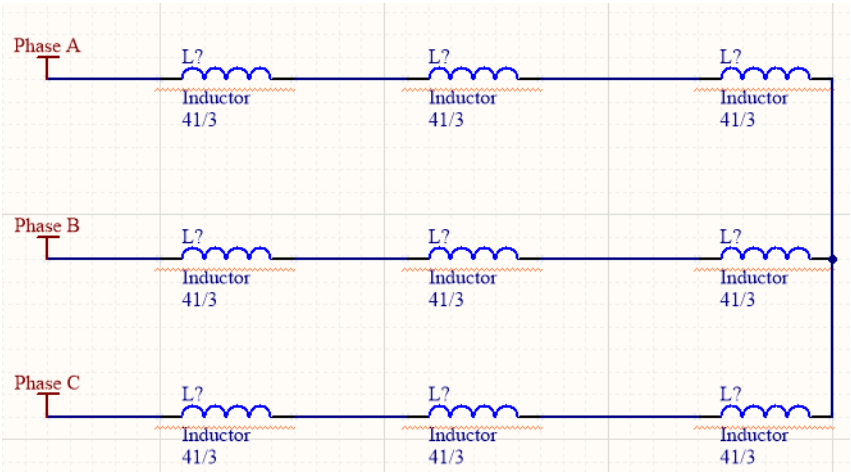

Figure 16: Equivalent circuit for the stator winding using series connection of the coils

4.1.4 Soft iron materials

In any medium, the reluctance is decided by the material geometries and the permeability of the material. In air the permeability is constant and hence relationship between the magnetic flux density and the magnetic field strength will remain constant. In electric machines, different metal alloys are commonly used as cores which encapsulates the magnetic circuit. The materials are defined as ferromagnetic materials which means that the relative permeability is much larger than 1 [7].

These materials with a higher permeability can achieve a much lower reluctance than air. That is however at the cost of not having a constant permeability and as the magnetic field strength increases to a certain level, the core material will saturate. This is called hysteresis which also entails another phenomenon whereas a magnetic field is applied, there will be a corresponding flux density and when it is removed, there will still be a level of flux remaining within the material.

The flux density which remains when there is no magnetic field is called the remanent flux and is denoted B_r. In order to reduce this remanent flux, a negative magnetic field must be applied. The magnetic field strength required to reduce the flux to zero is called the coercive field intensity and is denoted H_c. If a larger negative magnetic field intensity is applied, a flux in the opposite direction will appear and if the field intensity is removed, the flux will drop to its remanent flux level but in the opposite direction [7], [6]. The materials used in the CFS17 motor is M235-35A and Vacodur 48 and their respective BH-curves are shown in Figure 17 and 18 respectively.

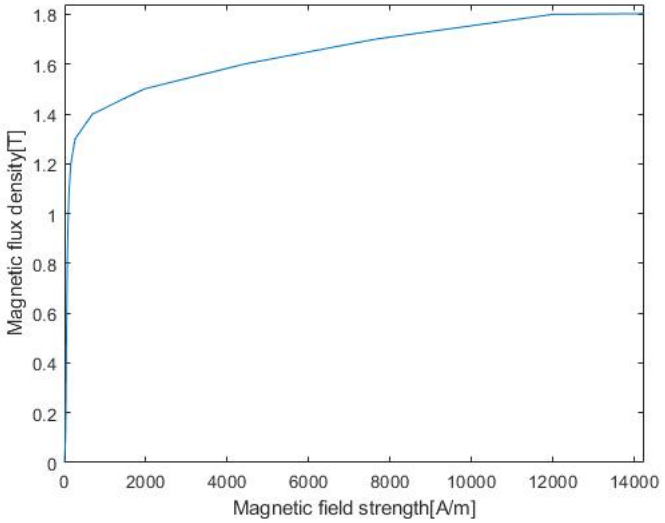

Figure 17: BH curve for the rotor lamination material, M235-35A

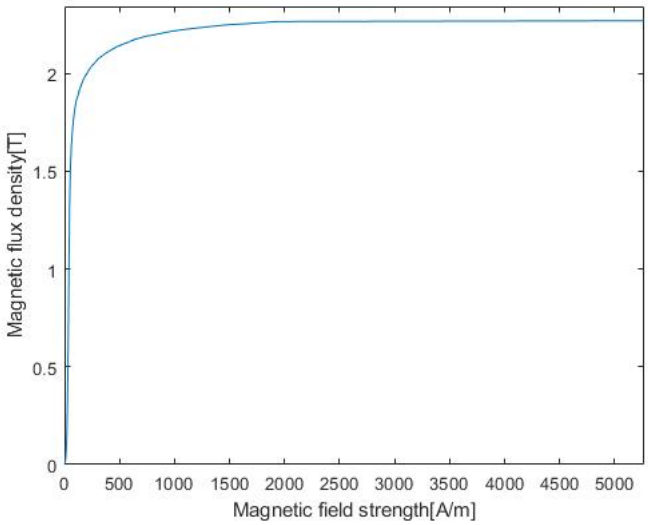

Figure 18: BH-curve for the stator lamination material, Vacodur-48

There is also a second dependency in the ferromagnetic materials which is that of frequency. When the frequency increases, the BH-curve will become more narrow which means that the material will magnetize at a lower field strength and will also saturate at a lower field strength. The stator core in an electric machine is affected by the temperature increase in the machine where according to [25], mainly the relative permeability in the saturation region is affected by temperature increase. That would mean that the maximum torque of the electric machine will decrease as a result of the premature saturation of the stator core.

4.2 Pole-Slot combinations

The number of poles in a PMSM is one of the most important design parameters. Having a large number of poles will reduce the required current/number of turns factor and/or reduce the need of magnet flux linkage. However, having a higher pole number will require a higher electric frequency in order to obtain the same mechanical speed in the machine [8], [11], [26]. The number of poles selected will have a great impact on which slot numbers are viable and vice versa. The restrictions on the pole slot combinations will be determined the structural strength required by the rotor and the physical space restrictions on the outer diameter of the motor. The pole selection will be based on how many poles that the rotor is able to house without compromising its structural integrity. Having a high number of poles comes with the advantage of having more parallel magnetic circuits in the machine which can allow for higher total flux in the machine and hence increase the torque. When designing the motor, the slot number must be specified and one of the most important parameters when designing the PMSM is the number of slots per pole per phase [6], [8], [16] which is calculated using

$$q = \frac{N_{slot}}{N_{pole} N_{phase}} \tag{95}$$

where:

- N_{slot} is the number of stator slots
- N_{pole} is the number of poles in the motor
- N_{phase} is the number of phases used

According to [27], the optimal choice for the number of slots per pole per phase number is 0.5 in order to obtain the lowest working harmonic as the lowest harmonic. Working harmonic is also known as the fundamental harmonic which is the torque producing part of the MMF.

For other pole-slot combinations, there will exist sub-harmonics which will limit the performance of the machine. The reason for this is the addition of unintended fluxes, EMF behaviours and torques which in turn will cause additional losses in the machine. [27], [6]. The key winding factor is defined as

$$W_{w,factor} = \frac{N_{slot}}{N_{Phase} \cdot GCD(2p, N_{slot})} \tag{96}$$

and is a common performance indicator for electrical machines. It indicates if the selected pole-slot combination will lead to a balanced motor for the phases, i.e. if the factor is a positive integer [27] and how many coils per phase the motor will have. The greatest common denominator also indicates if the magnetic forces in the machine is balanced or not. If the magnetic forces are not balanced there can be high levels of magnetic noise in the motor and hence noise in the torque output [28], [27]. In high performance machines, the key winding factor is often low. The general definition of the winding factor is the product of the distribution factor and the winding pitch factor [27]. It is calculated as

$$k_w = k_d \cdot k_p \tag{97}$$

where:

- k_w is the winding factor.
- k_d is the distribution factor.
- k_p is the winding pitch factor.

The distribution factor is the relationship between the sum of the phase phasors and the geometrical sum of the phasors [29]. If q_{ph} is even, the distribution factor is calculated as.

$$k_d = \frac{sin(\frac{q_{ph}}{2}\frac{\alpha_{ph}}{2})}{\frac{q_{ph}}{2}sin(\frac{\alpha_{ph}}{2})} \tag{98}$$

And if q_{ph} is odd, the distribution factor is instead calculated using [29]

$$k_d = \frac{sin(q_{ph}\frac{\alpha_{ph}}{4})}{q_{ph}sin(\frac{\alpha_{ph}}{4})} \tag{99}$$

where:

- q_{ph} is the number of slots per phase and must be an integer.
- α_{ph} is the angle between two adjacent stator tooth $[^o]$

The number of slots per phase is calculated using

$$q_{ph} = \frac{N_{slot}}{N_{phase}GCD(N_{slot}, p)} \tag{100}$$

and the angle between two adjacent slots is defined as

$$\alpha_{ph} = \frac{360^o}{N_{slot}}GCD(N_{slot}, p) \tag{101}$$

Finally the pitch factor is defined as

$$k_p = sin\frac{\frac{360^o p y_p}{N_{slot}}}{2} \tag{102}$$

where y_p is the pole pitch and is covered in the next Section [29], [8].

4.3 Rotor topologies and losses

In PM machines there will be significant space harmonics in the MMF present which will induce Eddy currents inside of the conductive rotor core due to being asynchronous with the rotor speed [30]. The MMF harmonics contribute to the total rotor losses in the rotor where the slot openings also are a contributing factor. That means that having a closed slot design could potentially reduce the losses within the rotor. According to [30] the use of single layer windings has larger rotor losses due to the increase of low order MMF harmonics compared to double layer windings [30]. Another source of low order harmonics in the MMF is the presence of harmonics on the phase currents. The MMF generated in a coil was given in (24) and then the total MMF in the stator is given by

$$\mathcal{F}_{current} = \frac{N_{series}}{N_{parallel}}(i_a N_{turn,coil} + i_b N_{turn,coil} + i_c N_{turn,coil}) \tag{103}$$

where:

- $\mathcal{F}_{current}$ is the total MMF in the stator $[A_{turn}]$
- $N_{parallel}$ is the number of coils connected in parallel
- N_{series} is the number of series connected coils

The current harmonics could be caused by the inverter design and in this project, it is assumed that the current supplied to the machine is an ideal sinusoidal waveform. The harmonics can also be caused by imperfections in the magnetic circuit such as local points with high reluctance [31]. In the old CFS17 PMSM, the motor used internally mounted PMs (IPMs) which compared to surface mounted PMs will lead to lower Eddy current losses. The Eddy current losses are mainly caused by the change in permeance in the air gap caused by the slot openings. The use of IMPs is common within the automotive industry due to the increase in torque density which is caused by an increase of the saliency in the machine [32]. In the rotor there are what is known as flux barriers which are cutouts in the rotor laminations which are usually close to or directly connected to the magnet pockets in which the magnets are inserted. The purpose of those is to reduce the magnet leakage flux and that is done by replacing the ferromagnetic material with air in areas where that flux would otherwise pass through. The leakage flux will mainly be passing through the rotor ribs and the rotor bridge as can be seen in Figure 10 and therefore limiting the amount of ferromagnetic material in the ribs and bridges is desirable from an electro-magnetic point of view.

When designing the rotor, the flux paths of the coil and magnet must be considered since they will not be the same. The flux produced by the coils will flow through the ribs of the rotor which means that they cannot be too small or otherwise there will be significant hysteresis losses. Also, they cannot be too large, otherwise there is a risk of having significant leakage flux from the magnets. In terms of rotor topology, there are several important factors to consider. The magnetic flux produced by the magnets is the first consideration where different topologies will lead to different fundamental flux magnitudes but also different harmonic contents. The cut-outs needed for the magnets in the rotor stack will influence the structural integrity of the rotor and depending on the expected forces acting on the rotor stack. Also, the thermal behaviour of the rotor material is important and especially for high performance machines. As certain materials are heated up, they expand, and that behaviour could be problematic since the airgap between the stator and the rotor is generally small for high performance machines. The CFS17 motor uses a flat magnet rotor design which has the main advantage of being easy to manufacture [33]. The downside with that topology is that it has higher losses when operating the motor in field weakening [34]. According to [35], the torque will be slightly higher in the constant torque range as mentioned previously, the losses will be higher. [36] suggest the use of decentred permanent magnet topology should be used for motors requiring high efficiency and high torque.

In addition to the working torque produced by the machines, there will be other components of the output torque. One such component is the cogging torque which is an undesirable effect caused by the attraction forces between the stator and the permanent magnets which causes torque ripple and could make the motor more difficult to control. The cogging torque also manifests itself as noise and vibrations which is especially prevalent at lower speeds [37]. Cogging torque is mainly caused by the stator and rotor design structure and is attributed to the flux in the air gap. However according to [37], the methods that can be used to reduce the cogging torque in a given machine with surface mounted PMs will reduce the overall performance of the machine. The use of inset mounted magnets is one method to reduce the cogging torque of the machine [38]. Torque ripple is a component of the torque which is present when the magnetic circuit is energized. Ripple torque consist partially of the cogging torque but also by torque components caused by harmonics in the flux of the machine. The torque ripple varies depending on the rotor angle and can be reduced by increasing the number of poles in the rotor.

4.4 Manufacturing and degradation

This section will cover the manufacturing options for the machine and the possible performance effects of each method discussed.

4.4.1 Winding

As previously mentioned, the coil winding method previously used was winding by hand and that is not a time efficient coil winding method. Since the motor will use concentrated windings, the manufacturing options is reduced slightly. Concentrated winding can be wound using a needle-winding machine where a needle is inserted between the coils. Using a needle is usually not preferable for high performance motors due to the gap needed between the two coils which needs to be able to accommodate the needle which would mean that it is not possible to obtain a high fill factor in the machine. One option when using the needle-winding method, whilst still obtaining a high fill factor is to partially wind one coil to the extent that there is enough space for the needle to wind the coil next to it and then extract enough wire out of the machine to wind the remaining coils [39] [40]. The remaining turns is then wound by hand and that might be a way to reduce the manufacturing time.

Another option would be to divide the stator into segments which is wound individually and then is glued together to form the stator. One possible problem with this method would be to ensure that the stator becomes completely symmetrical. That is especially important for the airgap where a varying gap length could cause a failure of the motor. Especially when the rotor temperature increases, and the material expands. The rotor losses will be at its maximum at high speeds which means that the risk of having the temperatures rise to the extent of the material expanding so it comes into contact with the stator. That will result in the rotor welding itself to the stator.

4.4.2 Cutting and bonding stator and rotor laminations

The manufacturing of the stator laminates for large volume motors are generally done through punching of metal sheets but that method is generally quite expensive due to the cost of the equipment. For smaller batches, the laminations are often laser cut or water cut due to the significant reduction in cost [40]. Two other options would be to water cut the stator laminations or to use wire electrical discharge machining. According to [41], the choice in manufacturing procedure has an influence on the motor efficiency and that using wire electrical discharge machining will give the highest motor efficiency. Also, the degradation also is extended some distance into the lamination from the point of cutting. According to [42] this surface extends to 1-1.5 mm when using punching as the lamination cutting method.

Once the stator laminations have been manufactured, they need to be bonded to form the stator core. This could be done in several ways. One option is to weld the stator laminations together which would then cause a short circuit the laminations at the welding point which could lead to higher iron losses due to higher Eddy currents. Another option is to have holes drilled in the laminations and in which bolts are inserted, which clamps the laminations together. Using this will not only cause problems with short circuiting the laminations, but also the flux path is interrupted. That will cause there to be local regions with high flux density which will lead to even higher core losses due to increased hysteresis losses. That can also be achieved when winding the stator where the windings themselves can hold the laminations in place. That would both solve the issue of shorting out the laminations and the local regions with high flux density. It would however add a level of instability in the stator core which could become a problem if the stator is to be press fitted into a cooling jacket. The technique used in the CFS17 motor is to assemble the laminations using a coating on each lamination before they are stacked and then they are cured in place. In the case of the CFS17 motor, since the motor is to be press fitted into a cooling jacket, having the correct positioning on the laminations is important in order to reduce the risk of damaging the stator when pressing. According to [43], when using punching and welding the stator laminations together the losses increase due to degradation of the stator laminations. The performance deviation between different motors manufactured with the same method also increases. However, it was also concluded that the deviation was larger between motor batches and was found to be caused by differences in steel quality.

4.5 Coil insulation and thermal behaviour

The windings used in the stator coils are coated with an insulated coating but that is not sufficient insulation against the stator. Usually on electric machines, sheets of Nomex based or Mylar material is used as insulating material between coils and between windings and the stator which can be seen in Figures 13 and 14. The use of these materials could potentially create a problem in terms of cooling in the machine. The thermal properties of the insulation materials are generally poor as compared to the rest of the motor.

Also, at the ends of the stator, an insulating material is needed when having concentrated windings. In the CFS17 motor, the insulation was 3D-printed which added some length to the motor. The end windings are also usually the point where the highest temperatures are reached due to the reduced cooling surface compared to the other parts of the coils. The end winding insulation used on the CFS17 motor is shown in Figure 19. There are two versions of this end winging where one of them are designed such that it has small engravings on the inside of the ring which has the purpose to guide the ends of the strands to simplify the y-connection.

Figure 19: 3D-printed end winding insulation where cut-outs for the end wires can be seen

4.6 Rotor assembly

The CFS17 motor used NdFeB magnets in the rotor which are glued into the rotor. That rotor is shown in Figure 20. One problem with that was that the curing temperature of the glue was close to the demagnetization temperature of the magnets. As can be seen in Figure 20, there is a cut-out for the rotor shaft and there is a guidance cut-out as well which is important such that the rotor does not start to slip from the shaft. Also, since two separate rotor stacks are used to form one full rotor, it is important that the poles are aligned in order for the PMSM to function properly.

Figure 20: The CFS17 rotor where the cut-out for the guide pin and where the magnets have been glued into the rotor

4.7 Cooling

Electric machines and especially PMSMs using rare earth magnets must not reach too high operating temperatures. If the temperature would reach too high levels, the ferromagnetic material will saturate at an earlier stage and more importantly the magnets could be permanently demagnetized or the winding insulation could be permanently damaged which could lead to short circuits. As the power density of new traction motors increases and they become smaller, the effects of passive cooling are reduced due to smaller cooling surface. It means that active cooling is required to cool those motors [44]. The previous motor had an efficiency of 91 % at the rated power of 13.5 kW. It means that 1.1215 kW in heat losses must be cooled. There will be heat dissipation in both the rotor and the stator. The CFS17 PMSM was cooled by the use of a cooling jacket which the stator is press fitted into. Using a cooling jacket is a form of indirect liquid cooling where the internally generated heat will conduct through the stator core into the inner channels of the cooling jacket where water flows. A simplified model of the cooling system used is shown in Figure 21.

In the industry, one common method for cooling machines is using air cooling by mounting a heat sink on the stator which has a large surface area and mounting a fan on the rotor shaft or via a belt drive which will force air through the stator and cool the rotor [44]. In some cases, a separate motor is used to cool the motor but that solution in not commonly used for automotive applications. Cooling the rotor in a

PMSM is more difficult since liquid cooling would increase the mechanical losses in the stator as well as adding complexity to the design. According to [44], there are options to have internal cooling inside the rotor shaft. One could also use spray oil cooling which then also could be used to cool the copper in the motor. One benefit of using that type of oil cooling would be that there will be no need to pot the motor using epoxy which would also make it possible to replace damaged coil windings. Using oil cooling could also allow for a lower weight cooling jacket since an inner layer will not be needed but also there would likely be a need for an oil pump in order to get sufficient cooling in the entire stator.

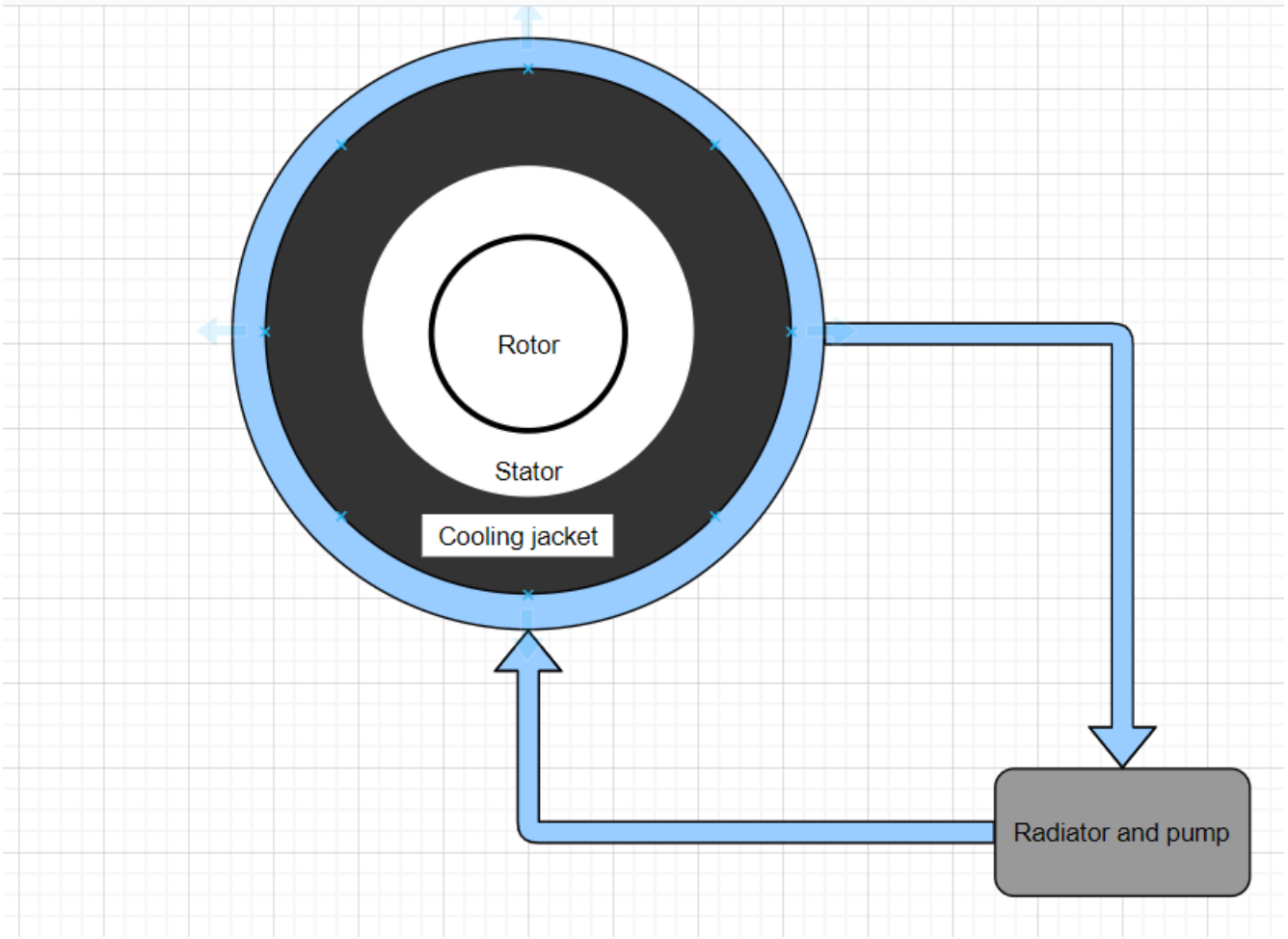

Figure 21: Simplified drawing of the cooling used in the CFS17 motor where the stator, rotor, cooling jacket and water flow path are shown

5 Methodology

The first step when designing a PMSM is to find the performance requirements as specified in the design flow chart shown in Figure 22. The performance requirements were obtained using the 1D-powertrain bicycle model described in Section 2.2, which was used to analyse driving cycles. The driving cycles themselves was speed data gathered at competitions and the events described in Section 2.3 (acceleration, autocross and endurance) was studied. That was the acceleration, autocross and endurance events. After obtaining the rated and maximum speed and torque of the machine, the FEM model of the old CFS17 motor was studied and the simulations was performed on that model to verify that it functioned as expected. Next two design concepts were developed and after evaluating the two, one would be further improved in an iterative design process. The first concept would seek to decrease the stack length whilst the second concept would be focused on reduced the outer stator diameter. The concepts were evaluated based on their maximum torque, phase voltage waveforms and rated operation. After deciding on a concept design to use in the iterative design, the concepts existing problems was investigated and proposed changes for the second iteration was presented and then implemented. The new iteration was then compared to the older versions and if the problems observed previously was not solved or that new problems arise, a new iteration would be made were changes would be implemented to eliminate these problems. When an iteration of the PMSM fulfilled the performance requirements, design goals and practical requirements, it would be compared to the previous versions in terms of cooling capabilities at rated operation and their overall weight would be compared. Also efficiency maps for some motors were obtained to investigate if the motor efficiencies have changed compared to the CFS17 motor. Finally suggestions for manufacturing would be made based on the literature study conducted in Chapter 4.4. Also suggested improvements for future motor design projects was discussed and presented where improvements to the methodology, tools used and future areas of interest would be recommended.

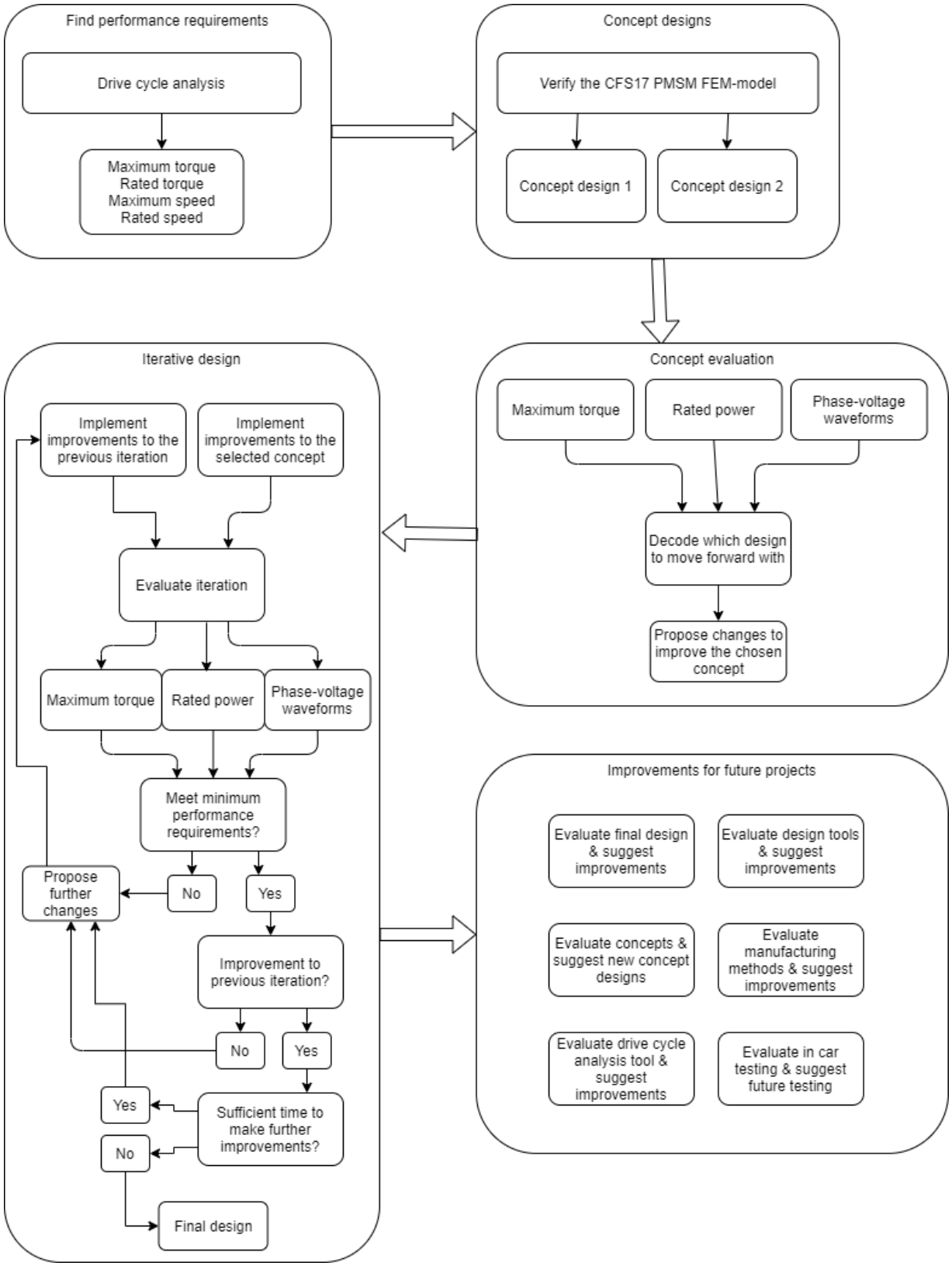

Figure 22: Flow chart of the project work where the design procedure from obtaining the PMSM parameters to the iterative process of designing a new PMSM

5.1 CFS17 PMSM and motor geometry definitions

The CFS17 PMSM was designed using an iron-cobalt alloy as specified in Table 5 where the specification of the motor is shown. The iron-cobalt allows for flux densities above 2 T and having materials which allow for high flux densities will enable the motor to have a high power density compared to motors with materials with lower flux densities. The motor has 9 slots and 3 pole pairs which means that it has half a slot per pole per phase and the lowest working harmonic of the MMF will be producing the torque. Concentrated windings are utilized which will provide advantages in terms of weight and lower copper losses. Each phase has three coils connected in parallel and the main reason for that is that it would not be possible to wind the stator with the thicker wire required to connect the coils in series. Due to the parallel connection of the coils, only a third of the total phase current will pass through each coil and therefore three times more turns are required per coil for the parallel connection to obtain the same MMF.

Table 5: The CFS17 motor specification

CFS17 motor parameters	
Rated power	13.5 kW
Maximum power	32 kW
Efficiency	91 %
Rated speed	11900 rpm
Maximum speed	20000 rpm
Rated torque	10.8 Nm
Maximum torque	24.1 Nm
Stator outer diameter OD_{stator}	90 mm
Stator inner diameter ID_{stator}	50 mm
Stack length L_{stack}	70 mm
Number of slots	9
Winding type	Concentrated
Connection type	Y-connection
Number of parallel branches	3
Number of winding turns	41
Wire material	Copper
Wire diameter	1.12 mm
Number of pole pairs	3
Magnet type	Nd-Fe-B (rare-earth)
Rotor lamination material	M235-35 A
Stator material	Vacodur-48
Cooling method	Water (Cooling jacket)
Slot insulation material	Mylar

The geometrical definitions of the PMSM can be difficult to visualize so in Figure 23 the most important geometry definitions are shown. Usually when defining the geometries of the PMSM, diameters are often used and therefore the rotor shaft, rotor, inner stator and outer stator radius is written in terms of $diameter/2$. The PMSM geometries defined in Figure 23 was in this project used when re-scaling the CFS17 PMSM and to calculate the resistance in the phases. The one parameter which is not pointed out and cannot be in a 2D-model is the stack length which is the length of the motor.

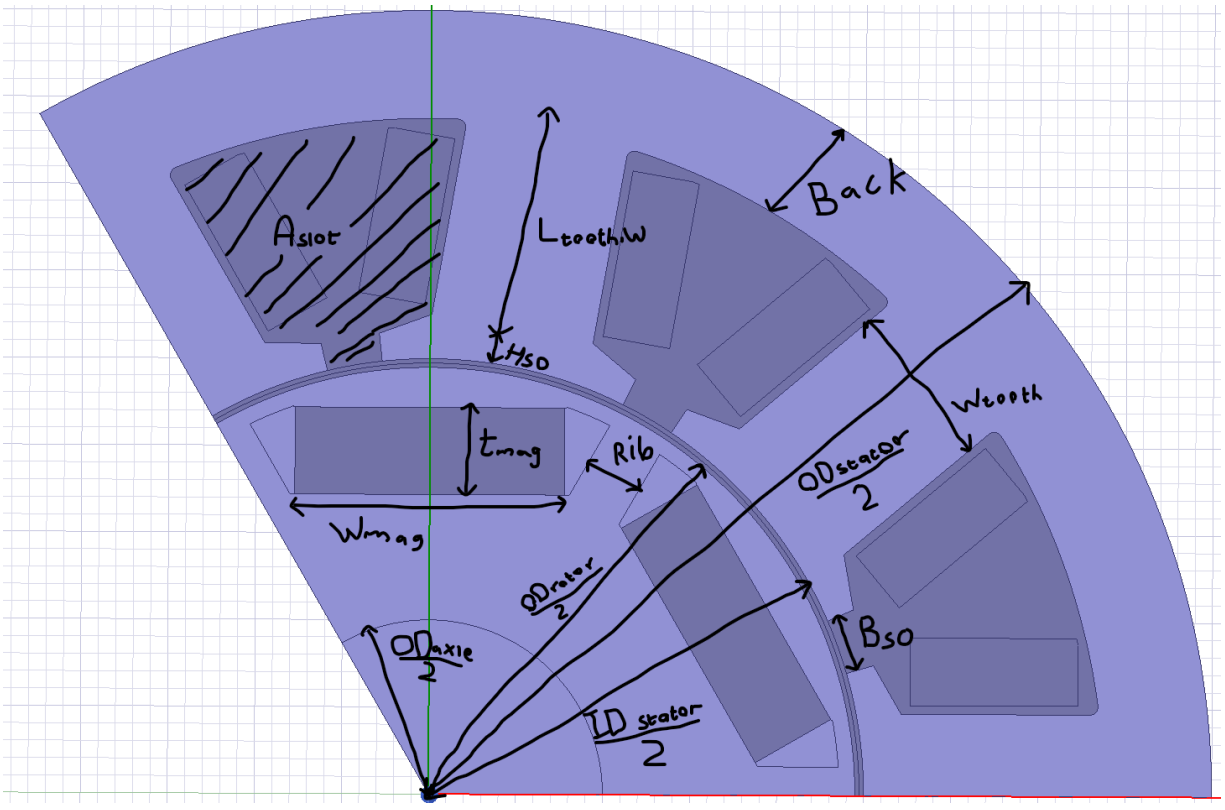

Figure 23: Geometry definitions of the 2D-PMSM illustrated where the specific motor shown is the CFS17 motor.

6 PMSM performance requirements

The power requirements of the new PMSM are found by studying drive cycles and previous testing data. The simulation model used when studying the drive cycles is a simplified powertrain model developed by Stefan Lundberg and Stefan Skoog. The model was used when the specification of the previous PMSM in 2017 was set. Using this drive cycle analysis tool will only provide information on what would be required from a previous car and not a future car. It would therefore be preferable to use a lap time simulation tool where different designs could be tested and their respective effects on the lap times examined. Such a tool of sufficient quality does not exist however, so the drive cycle analysis was the only alternative available.

6.1 Simplified powertrain model and driving cycles

The Simulink powertrain model shown in Figure 24 uses three inputs, longitudinal acceleration, velocity and time. These inputs either origins from old test data obtained from competitions and in-car testing sessions or from lap time simulations of the car. The inputs are sent to the speed controller which as mentioned acts as the driver which tries to follow the speed by sending positive or negative force requests to the powertrain. The powertrain recalculates the force requests to torque requests to the front and rear motors. When accelerating, the torque is distributed using a factor k_{acc} which determines how much of the total torque will be distributed on the rear wheels. The torque distributed to the front motors will therefore be $1 - k_{acc}$. During deceleration, the negative torque request is will be distributed between the motors and the mechanical brakes using k_{brake} where the torque requested from the mechanical then will be $1 - k_{brake}$. The distribution of braking force on the rear wheels is determined by $k_{balance}$ and the torque on the front wheels is given by $1 - k_{balance}$. The model has a built-in ideal slip controller which prevents the wheels from slipping too much and will hence limit the maximum torque that the motors can produce. In addition to that the torque is also limited by the maximum allowed power of 80 kW from the TS. Also the maximum charge power of the battery is set using P_{charge}.

The torque requests are sent to the model of the TS where the power calculations from the battery to the mechanical power on the wheels are computed. In these calculations, the system efficiency and battery voltage are taken into account. Also should the maximum current to the motors be exceeded, the torque to the motors is also limited. The model of the battery will calculate the battery voltage depending on the state of charge (SOC) of the battery. The output from the TS model is sent to the vehicle model which is a 1-D bicycle model which is described in Section 2.2. The parameters used in the model was updated to measured or estimated values from the CFS20 car. The driving cycles are created using testing data previously collected at competitions and at the test tracks. There were processed test data up to date until 2018 which could be used. Some of the drive cycles had to be manually extracted from the test data due to it not having been post processed previously. The speed data was obtained from the estimated speed of the power electronics. Since the speed is estimated on all four wheels an average was taken from three of the values. The fourth estimated speed value was incorrect and hence was not used. The torque balance and the braking balance was set to what was considered as an extreme case operating condition. It is also assumed that 100 % of the braking force is provided by the motors. The extreme case considered used the following parameters.

- k_{acc}=45 %
- k_{brake}=100 %
- P_{charge}=-80 kW
- $k_{balance}$=80 %

The one parameter which were varied during the simulations was the gear ratio and ratios of 1:12, 1:14 and 1:16 were studied. The drive cycles used is listed in Table 6.

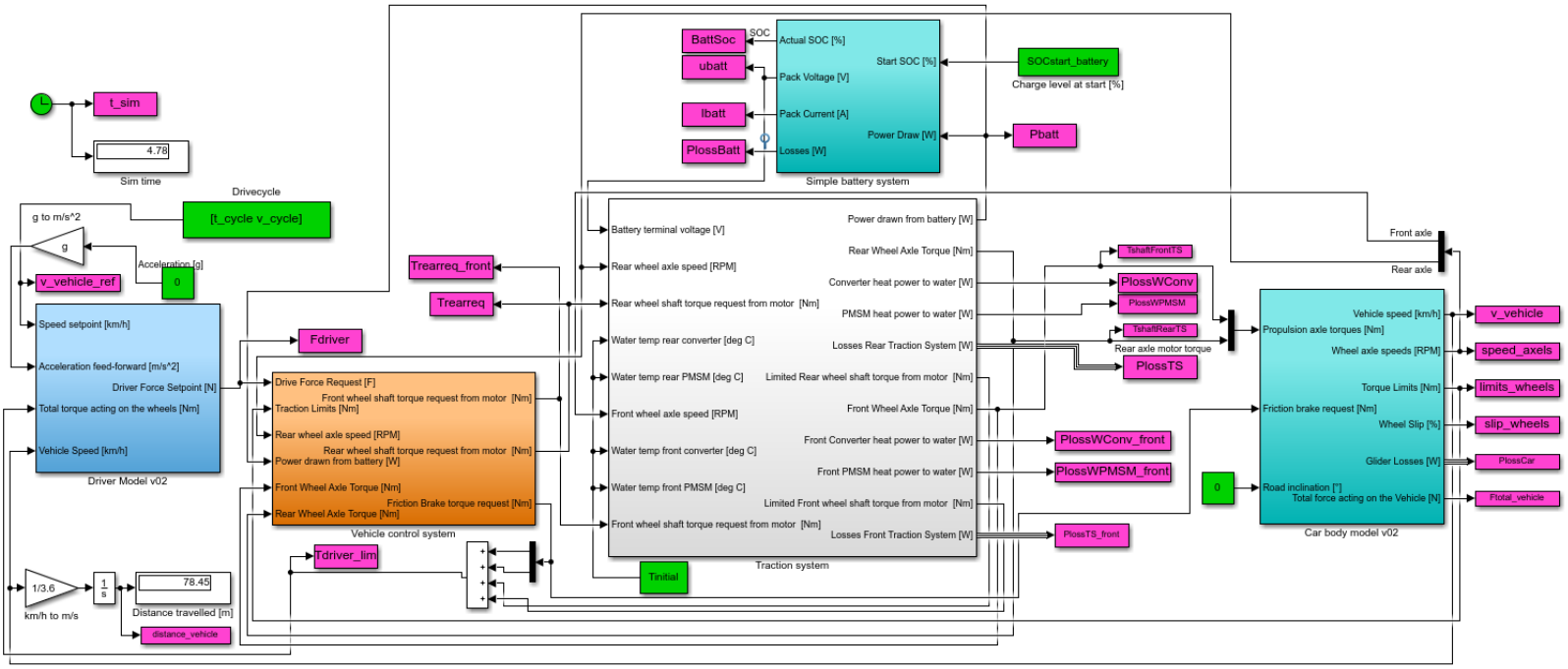

Figure 24: The Simulink 1D-powertrain model used to obtain the PMSM parameters by analysing drive cycles

What should be noted in Table 6 is that many of the drive cycles are obtained from data where a 2WD car was used. The reason that it can be used for a 4WD car is that only the speed and time data is considered. However, the individual tracks will have more impact on the speeds of the vehicle as compared to the powertrain used. Also one optimum lap simulation is used where the grip of the tires is the only limiting factor considered.

Table 6: List of all drive cycles used in the 1D-powertrain model

Name	Year	Original competition	Driving wheels	Distance	Duration	Maximum speed	Average speed
Autocross 1	2016	FSG	2WD	1232 m	95 s	88.4 km/h	47 km/h
Autocross 2	2016	FSG	2WD	1233 m	95 s	88.4 km/h	47 km/h
Autocross 3	2019	FSAC	4WD	386.8 m	31.2 s	74.4 km/h	45 km/h
Autocross 4	2019	FSAC	4WD	159.6 m	13.2 s	68.6 km/h	43.4 km/h
Optimum lap simulation	2017	-	2WD	1259 m	74 s	107.6 km/h	61.4 km/h
Endurance 1	2016	FSG	2WD	11 084 m	749 s	95.2 km/h	53.3 km/h
Endurance 2	2016	FSG	2WD	5154 m	343 s	90.9 km/h	54.1 km/h
Endurance 3	2018	FSG	2WD	11 049 m	736 s	96.5 km/h	54 km/h
Acceleration 1	2019	FSAC	4WD	78.2 m	4.8 s	99.8 km/h	59 km/h
Acceleration 2	2019	FSAC	4WD	99.1 m	6 s	100 km/h	58.7 km/h
Acceleration 3	2019	FSAC	4WD	78.5 m	4.8 s	98.9 km/h	58.4 km/h

In the following sections, a typical measurement for each event will be presented followed by all of the key results from the simulations.

6.2 Drive cycle analysis results

Figure 25, the powerflow plots is shown for the Autocross 2 drive cycle. For the front PMSM it should be noted that higher torque magnitudes are achieved when braking as compared to when accelerating. Also during one lap of the autocross circuit, a braking torque of -20 Nm or more was exceeded six times as can be seen on the purple and black lines in the front PMSM torque plot. These peaks in torque occurred at higher speeds as can be seen in the PMSM speed plot. When comparing the front and rear PMSMs, it can be seen in Table 8 that the RMS torque is higher for the front PMSM and that the peak torque when accelerating is higher for the rear PMSM. In the battery plot it can be seen that the powerflow from the battery to the front and the rear motors will be similar during acceleration and that the front power will be higher for the front motors during braking.

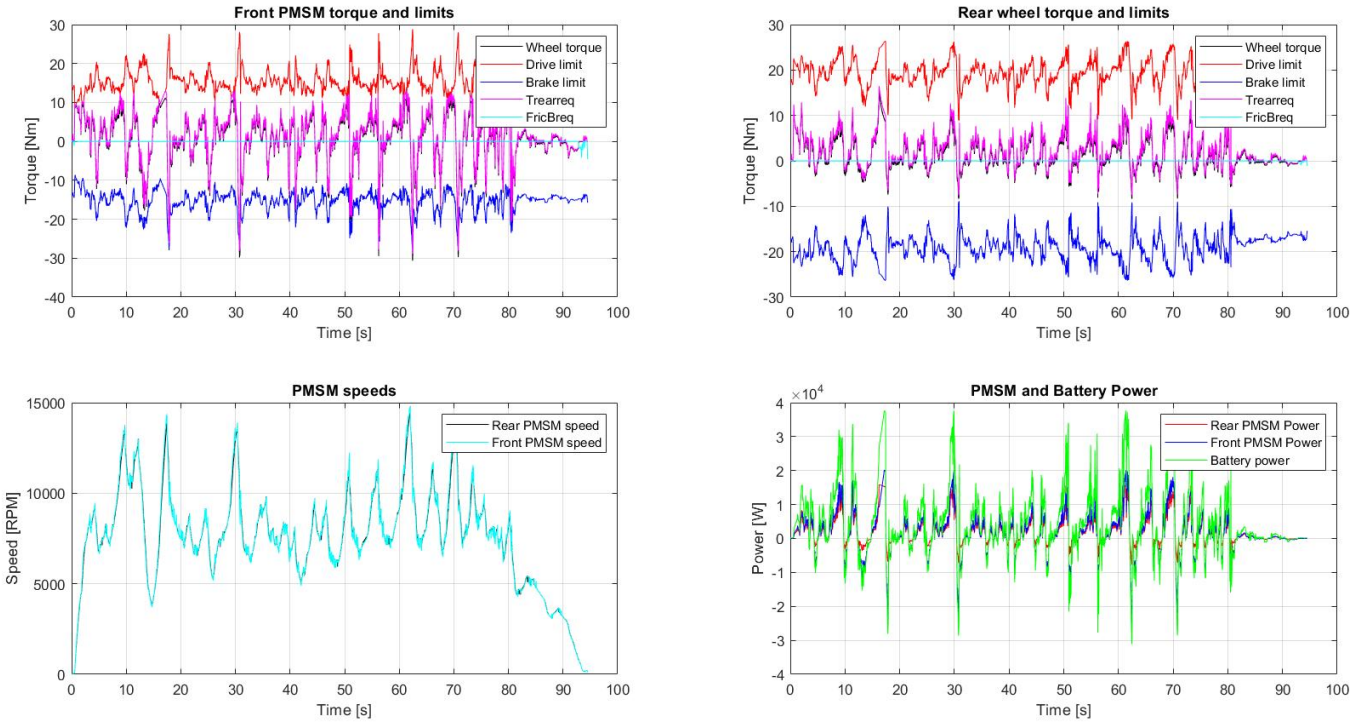

Figure 25: Autocross 2 simulation result using a 1:14 gear ratio where the front and rear PMSM torque, traction limits, references and mechanical brake torque. Also the PMSM speeds and powerflow for one front and rear motors are shown

In Table 7 the results from the simulations using a 1:12 gear ratio. When utilizing a lower gear ratio, the torque should increase and the speed decrease as compared to Table 8 and 9. The endurance event is similar to the autocross event and can be described a large number of back-to-back autocross events without stopping after each lap. In Figure 26 it can be seen on the front PMSM torque plot that the behaviour is similar, both when accelerating and decelerating. The main advantage of studying the endurance drive cycle compared to the autocross drive cycle is that the RMS values will be more accurate. The reason for that is because the endurance run is similar to the autocross in terms of track layout but is much longer and hence more data is obtained. The key numbers for the new PMSM design from the autocross and endurance drive cycles is the RMS torque and the average speed which will determine the required rated power of the machine. The reason that the RMS values are of interest for the motor design is the power losses in the machine where the direction of the powerflow will not have any effect on the

losses. The RMS value is calculated using

$$T_{RMS} = \sqrt{\frac{1}{\tau}\int_{\tau} |T_{PMSM}|^2 dt} \tag{104}$$

where τ is the duration of the cycle and T_{RMS} is the RMS torque. It can also be noted that the results

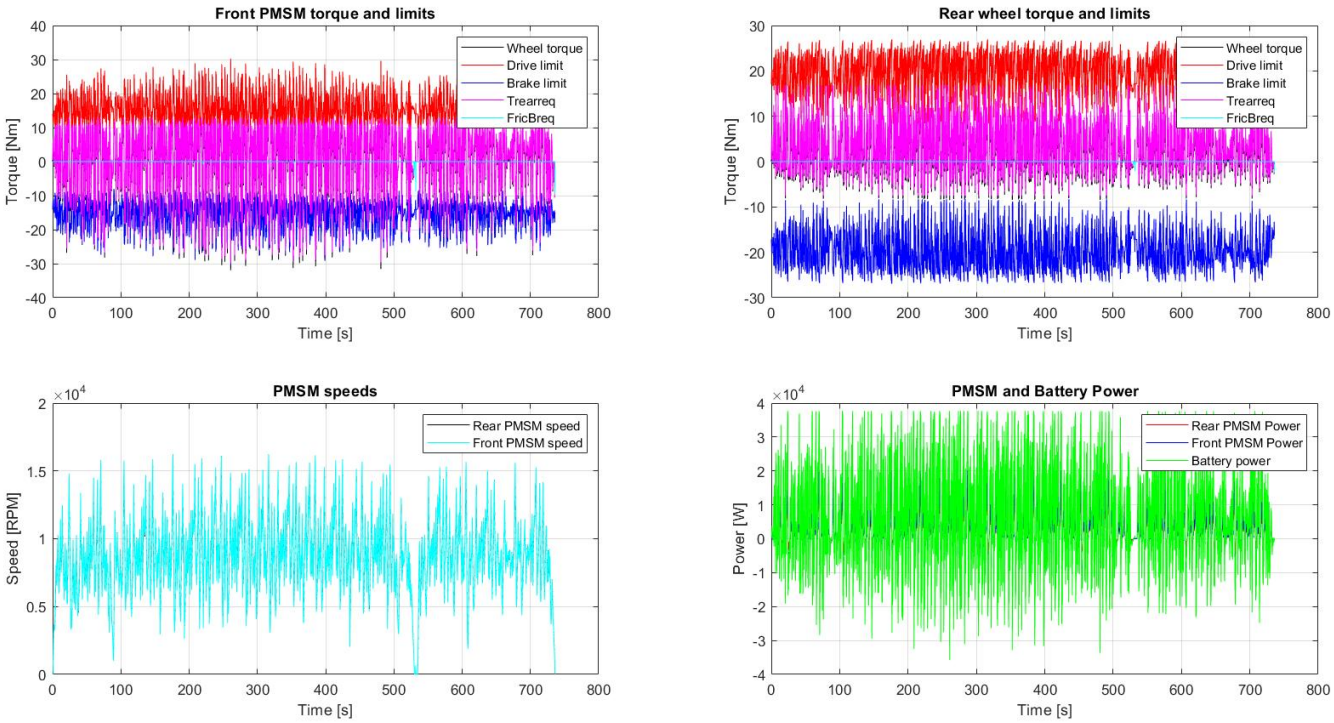

Figure 26: Endurance 3 simulation result using a 1:14 gear ratio where the front and rear PMSM torque, traction limits, references and mechanical brake torque. Also the PMSM speeds and powerflow for one front and rear motors are shown

found in Table 10, 11 and 12 show similar results to that of the autocross and it cannot be concluded that the differences that are there is attributed to the difference between autocross and endurance. The RMS power is however generally lower in the autocross than in the endurance and that could be attributable to the fact that the time from completion of the event until the data-logging stops is a smaller part of the driving cycle in the endurance event. The maximum speed and torque data must however be cross examined with the data from the acceleration events in order to determine which values are the most suitable for the machine. In Figure 27 it can be seen that the torque on the front PMSM is restricted by the torque limitation which is caused by having too low traction on the front tires. Therefore more torque is sent to the rear wheels as can be seen in at around 0.7 s. As the car gains speed, the traction on the tires will increase and hence the torque on the front tires can start to increase and the torque on the rear tires will drop back down such that the specified traction balance is restored.

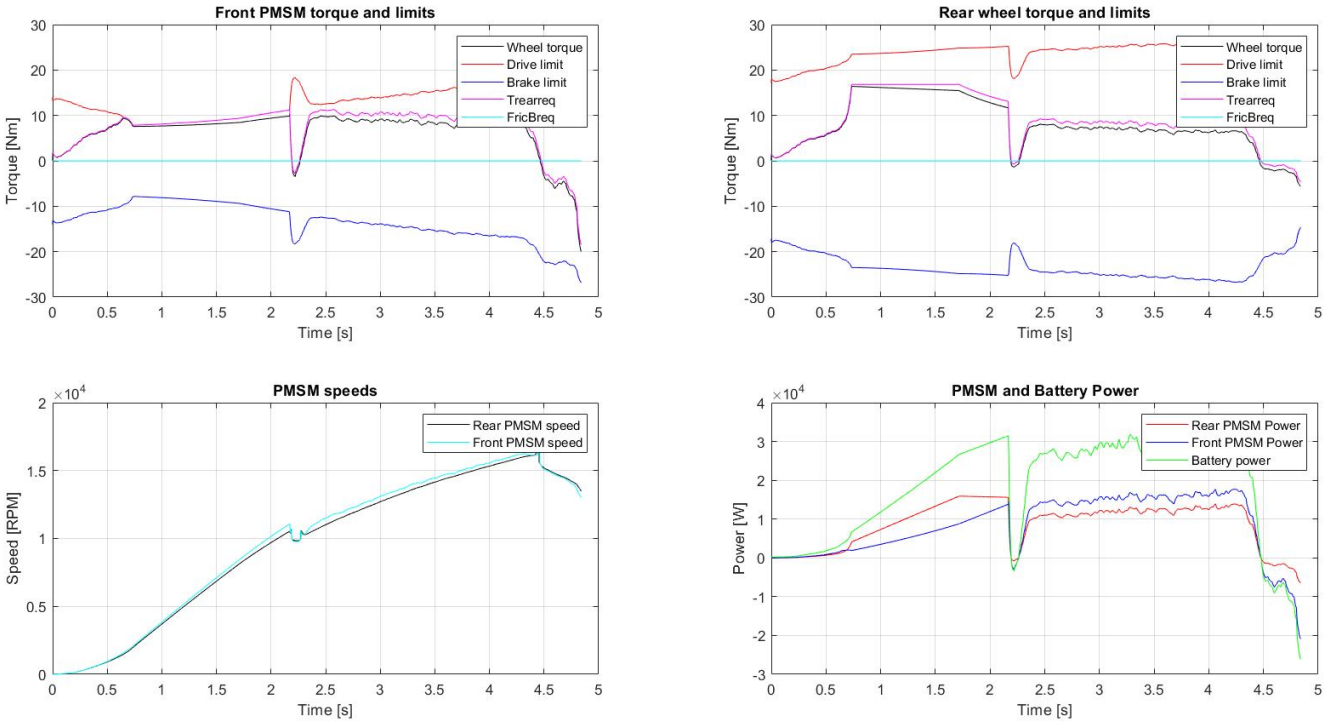

Figure 27: Acceleration 3 simulation results using a 1:14 gear ratio where the front and rear PMSM torque, traction limits, references and mechanical brake torque. Also the PMSM speeds and powerflow for one front and rear motors are shown

The negative torques seen in Table 13, 14 and 15 for Acceleration 1 and Acceleration 3 can be attributed to the deceleration at the end of the event. That is however not the case for Acceleration 2 where at the competition, the car span out which invalidates some of the data from that driving cycle.

6.2.1 Autocross result tables

Table 7: Autocross and Optimum lap simulation drive cycles results with 1:12 gear ratio where the performance requirements for the front and rear PMSMs are shown and the battery powerflow is also shown

Parameters	Autocross 1	Autocross 2	Autocross 3	Autocross 4	Optimum lap simulation
Front PMSM max power	20.5 kW	20.5 kW	14.6 kW	15.7 kW	20.5 kW
Front PMSM min power	-25 kW	-25 kW	-12.2 kW	-12.5 kW	-35.7 kW
Front PMSM RMS power	6.2 kW	6.2 kW	5.1 kW	5.8 kW	12.7 kW
Front PMSM max torque	13.3 Nm	13.3 Nm	12.3 Nm	12.3 Nm	13.3 Nm
Front PMSM min torque	-35.3 Nm	-35.4 Nm	-18.3 Nm	-29.3 Nm	-37.3 Nm
Front PMSM RMS torque	7.32 Nm	7.3 Nm	8.5 Nm	7 Nm	13.5 Nm
Front PMSM max speed	12 675 RPM	12 675 RPM	10 682 RPM	10051 RPM	15 474 RPM
Front PMSM RMS speed	6879 RPM	6880 RPM	6412 RPM	6428 RPM	8868 RPM
Rear PMSM max power	16 kW	16 kW	16 kW	16 kW	15.6 kW
Rear PMSM min power	-7.7 kW	-7.7 kW	-3.6 kW	-3.7 kW	-11.1 kW
Rear PMSM RMS power	4.3 kW	4.4 kW	4 kW	4.0 kW	8.1 kW
Rear PMSM max torque	17.8 Nm	17.8 Nm	18.7 kW	18.7 Nm	19.5 Nm
Rear PMSM min torque	-9.5 Nm	-9.6 Nm	-4.9 Nm	-7.5 Nm	-9.9 Nm
Rear PMSM RMS torque	4.4 Nm	4.4 Nm	5 Nm	6.2 Nm	7.2 Nm
Rear PMSM max speed	12 684 RPM	12 685 RPM	10 689 RPM	9865 RPM	15480 RPM
Rear PMSM RMS speed	6847 RPM	6848 RPM	6392 RPM	6390 RPM	8747 RPM
Battery max power	76.5 kW	76.5 kW	59.3 kW	66.4 kW	76.5 kW
Battery max charging power	-62.3 kW	-62.3 kW	-30 kW	-30.8 kW	-89.6 kW
Battery RMS power	21.7 kW	21.7 kW	19 kW	21.7 kW	42.4 kW

Table 8: Autocross and Optimum lap simulation drive cycles results with 1:14 gear ratio where the performance requirements for the front and rear PMSMs are shown and the battery powerflow is also shown

Parameters	Autocross 1	Autocross 2	Autocross 3	Autocross 4	Optimum lap simulation
Front PMSM max power	20.2	20.2 kW	14.5 kW	15.6 kW	20.2 kW
Front PMSM min power	-25	-24.9 kW	-12 kW	-12.6 kW	-34.9 kW
Front PMSM RMS power	6.2 kW	6.2 kW	5.2 kW	5.7 kW	12.6 kW
Front PMSM max torque	11.2 Nm	11.1 Nm	10.4 Nm	10.4 Nm	11.2 Nm
Front PMSM min torque	-30.6 Nm	-30.6 Nm	-15.5 Nm	-25 Nm	-32.2 Nm
Front PMSM RMS torque	6.2 Nm	6.2 Nm	6 Nm	7.3 Nm	11.4 Mm
Front PMSM max speed	14 788 RPM	14 788 RPM	12462 RPM	11 668 RPM	17896 RPM
Front PMSM RMS speed	8025 RPM	8025 RPM	7482 RPM	7498 RPM	10332 RPM
Rear PMSM max power	15.9 kW	15.9 kW	15.9 kW	15.9 kW	15.4 kW
Rear PMSM min power	-7.7 kW	-7.7 kW	-3.5 kW	-3.7 kW	-11.1 kW
Rear PMSM RMS power	4.4 kW	4.4 kW	4 kW	4.9 kW	8.1 kW
Rear PMSM max torque	15.1 Nm	15.1 Nm	15.9 Nm	15.85 Nm	16.7 Nm
Rear PMSM min torque	-8.3 Nm	-8.4 Nm	-4.3 Nm	-6.52 Nm	-8.7 Nm
Rear PMSM RMS torque	3.8 Nm	3.8 Nm	4.3 Nm	5.3 Nm	6.1 Nm
Rear PMSM max speed	14 799 RPM	14799 RPM	12 471 RPM	11 509 RPM	17 905 RPM
Rear PMSM RMS speed	7886 RPM	7886 RPM	7455 RPM	7452 RPM	10 192 RPM
Battery max power	75 kW	75.3 kW	58.79 kW	65.6 kW	75.4 kW
Battery max charging power	-62 kW	-62.2 kW	-29.6 kW	-31 kW	-88 kW
Battery RMS power	21.9 kW	21.9 kW	19 kW	21.8 kW	42.3 kW

Table 9: Autocross and Optimum lap simulation drive cycles results with 1:16 gear ratio where the performance requirements for the front and rear PMSMs are shown and the battery powerflow is also shown

Parameters	Autocross 1	Autocross 2	Autocross 3	Autocross 4	Optimum lap simulation
Front PMSM max power	19.9 kW	19.9 kW	14.5 kW	15.3 kW	19.9 kW
Front PMSM min power	-24.8 kW	-24.8 kW	-11.9 kW	-12.6 kW	-34.1 kW
Front PMSM RMS power	6.3 kW	6.3 kW	5.2 kW	5.7 kW	12.5 kW
Front PMSM max torque	9.6 Nm	9.6 Nm	9 Nm	8.9 Nm	9.9 Nm
Front PMSM min torque	-27.1 Nm	-27.1 Nm	-13.5 Nm	-21.8 Nm	-28.4 Nm
Front PMSM RMS torque	5.4 Nm	5.4 Nm	6 Nm	6.3 Nm	9.9 Mm
Front PMSM max speed	16 905 RPM	16 905 RPM	14 246 RPM	13 264 RPM	20271 RPM
Front PMSM RMS speed	9170 RPM	9170 RPM	8551 RPM	8566 RPM	11 791 RPM
Rear PMSM max power	15.8 kW	15.8 kW	15.8 kW	15.7 kW	15.2 kW
Rear PMSM min power	-7.7 kW	-7.7 kW	-3.5 kW	-3.7 kW	-11 kW
Rear PMSM RMS power	4.5 kW	4.5 kW	4 kW	4.9 kW	8.2 kW
Rear PMSM max torque	13.1 Nm	13.1 Nm	15.8 Nm	13.7 Nm	14.6 Nm
Rear PMSM min torque	-7.5 Nm	-7.5 Nm	-3.8 Nm	-5.8 Nm	-7.8 Nm
Rear PMSM RMS torque	3.8 Nm	3.3 Nm	3.7 Nm	4.7 Nm	5.4 Nm
Rear PMSM max speed	16 914 RPM	16 914 RPM	14 252 RPM	13 154 RPM	20271 RPM
Rear PMSM RMS speed	9122 RPM	9422 RPM	8518 RPM	8513 RPM	11 633 RPM
Battery max power	74.1 kW	74.1 kW	58.3 kW	64.9 kW	75.1 kW
Battery max charging power	-62 kW	-62.2 kW	-29.2 kW	-31 kW	-86 kW
Battery RMS power	21 kW	22 kW	19.1 kW	21.8 kW	42.1 kW

6.2.2 Endurance result tables

Table 10: Endurance drive cycles results with 1:12 gear ratio where the performance requirements for the front and rear PMSMs are shown and the battery powerflow is also shown

Parameters	Endurance 1	Endurance 2	Endurance 3
Front PMSM max power	20.5 kW	20.2 kW	20.5 kW
Front PMSM min power	-26.8 kW	-24.5 kW	-28.9 kW
Front PMSM RMS power	7.2 kW	6.8 kW	8.7 kW
Front PMSM max torque	13.3 Nm	13.2 Nm	13.3 Nm
Front PMSM min torque	-35.7 Nm	-35 Nm	-37 Nm
Front PMSM RMS torque	8 Nm	6.8 Nm	10.2 Nm
Front PMSM max speed	13 651 RPM	13 030 RPM	13 974 RPM
Front PMSM RMS speed	7627 RPM	7683 RPM	7802 RPM
Rear PMSM max power	16.1 kW	16.1 kW	16.1 kW
Rear PMSM min power	-8.1 kW	-7.5 kW	-8.8 kW
Rear PMSM RMS power	5.2 kW	4.8 kW	6.2 kW
Rear PMSM max torque	18.4 Nm	18.3 Nm	19.1 Nm
Rear PMSM min torque	-9.6 Nm	-9.5 Nm	-9.7 Nm
Rear PMSM RMS torque	4.9 Nm	4.8 Nm	6.4 Nm
Rear PMSM max speed	13 663 RPM	13 045 RPM	13 975 RPM
Rear PMSM RMS speed	7586 RPM	7645 RPM	7734 RPM
Battery max power	76.5 kW	75.5 kW	76.5 kW
Battery max charging power	-61 kW	-62.2 kW	-72 kW
Battery RMS power	25.5 kW	24.3 kW	30.5 kW

Table 11: Endurance drive cycles results with 1:14 gear ratio where the performance requirements for the front and rear PMSMs are shown and the battery powerflow is also shown

Parameters	Endurance 1	Endurance 2	Endurance 3
Front PMSM max power	20.2 kW	20.2 kW	20.2 kW
Front PMSM min power	-26.5 kW	-24.3 kW	-28.6 kW
Front PMSM RMS power	7.3 kW	6.8 kW	8.7 kW
Front PMSM max torque	11.2 Nm	11.2 Nm	11.2 Nm
Front PMSM min torque	-31 Nm	-30.4 Nm	-31.9 Nm
Front PMSM RMS torque	6.8 Nm	6.4 Nm	8.8 Nm
Front PMSM max speed	15 927 RPM	15 213 RPM	16 229 RPM
Front PMSM RMS speed	8898 RPM	8964 RPM	9098 RPM
Rear PMSM max power	15.9 kW	15.9 kW	15.9 kW
Rear PMSM min power	-8.1 kW	-7.6 kW	-8.8 kW
Rear PMSM RMS power	5.2 kW	5 kW	6.3 kW
Rear PMSM max torque	15.6 Nm	15.7 Nm	16.3 Nm
Rear PMSM min torque	-8.4 Nm	-8.4 Nm	-8.5 Nm
Rear PMSM RMS torque	4.2 Nm	4.2 Nm	5.5 Nm
Rear PMSM max speed	15 941 RPM	15 220 RPM	16 240 RPM
Rear PMSM RMS speed	8847 RPM	8918 RPM	9018 RPM
Battery max power	75.3 kW	75.3 kW	75.4 kW
Battery max charging power	-66.2 kW	-62.2 kW	-71.5 kW
Battery RMS power	25.7 kW	24.5 kW	30.6 kW

Table 12: Endurance drive cycles results with 1:16 gear ratio where the performance requirements for the front and rear PMSMs are shown and the battery powerflow is also shown

Parameters	Endurance 1	Endurance 2	Endurance 3
Front PMSM max power	19.9 kW	19.9 kW	19.9 kW
Front PMSM min power	-26.1 kW	-24.2 kW	-28.3 kW
Front PMSM RMS power	7.3 kW	6.9 kW	8.7 kW
Front PMSM max torque	9.6 Nm	9.6 Nm	9.6 Nm
Front PMSM min torque	-27.4 Nm	-26.9 Nm	-28.1 Nm
Front PMSM RMS torque	5.9 Nm	5.6 Nm	7.6 Nm
Front PMSM max speed	18 207 RPM	17 385 RPM	18 493 RPM
Front PMSM RMS speed	10 169 RPM	10 246 RPM	10 392 RPM
Rear PMSM max power	15.8 kW	15.8 kW	15.8 kW
Rear PMSM min power	-8.1 kW	-7.5 kW	-8.8 kW
Rear PMSM RMS power	5.3 kW	5.1 kW	6.4 kW
Rear PMSM max torque	13.5 Nm	13.5 Nm	15.8 Nm
Rear PMSM min torque	-7.5 Nm	-7.4 Nm	-7.6 Nm
Rear PMSM RMS torque	3.7 Nm	3.7 Nm	4.8 Nm
Rear PMSM max speed	18 220 RPM	17 396 RPM	18 496 RPM
Rear PMSM RMS speed	10 107 RPM	10 189 RPM	10 300 RPM
Battery max power	74.2 kW	74.1 kW	74.2 kW
Battery max charging power	-60.4 kW	-62.2 kW	-71 kW
Battery RMS power	26 kW	24.8 kW	30.8 kW

6.2.3 Acceleration result tables

Table 13: Acceleration drive cycles results with 1:12 gear ratio where the performance requirements for the front and rear PMSMs are shown and the battery powerflow is also shown

Parameters	Acceleration 1	Acceleration 2	Acceleration 3
Front PMSM max power	16.2 kW	17.7 kW	17.3 kW
Front PMSM min power	-12.7 kW	-32.7 kW	-21.2 kW
Front PMSM RMS power	9.3 kW	12.9 kW	8.1 kW
Front PMSM max torque	12.2 Nm	12.6 Nm	12.2 Nm
Front PMSM min torque	-11.8 Nm	-37.2 Nm	-23.5 Nm
Front PMSM RMS torque	9.2 Nm	15.7 Nm	9.2 Nm
Front PMSM max speed	14 331 RPM	14 355 RPM	14 195 RPM
Front PMSM RMS speed	9553 RPM	9101 RPM	9506 RPM
Rear PMSM max power	16.1 kW	16.1 kW	16.7 kW
Rear PMSM min power	-3.7 kW	-10.1 kW	-6.4 kW
Rear PMSM RMS power	9.3 kW	10 kW	8.6 kW
Rear PMSM max torque	19 Nm	19.4 Nm	19.2 Nm
Rear PMSM min torque	-3.5 Nm	-9.8 Nm	-6.3 Nm
Rear PMSM RMS torque	11.4 Nm	11.5 Nm	11.4 Nm
Rear PMSM max speed	14 337 RPM	14 363 RPM	14 207 RPM
Rear PMSM RMS speed	9356 RPM	8987 RPM	9324 RPM
Battery max power	64.6 kW	68.3 kW	65.8 kW
Battery max charging power	-31.3 kW	-81.8 kW	-52 kW
Battery RMS power	45.6 kW	46.2 kW	45 kW

Table 14: Acceleration drive cycles results with 1:14 gear ratio where the performance requirements for the front and rear PMSMs are shown and the battery powerflow is also shown

Parameters	Acceleration 1	Acceleration 2	Acceleration 3
Front PMSM max power	16.6 kW	18.1 kW	17.7 kW
Front PMSM min power	-12.4 kW	-32.3 kW	-20.9 kW
Front PMSM RMS power	9.4 kW	13 kW	8.3 kW
Front PMSM max torque	10.3 Nm	10.7 Nm	10.3 Nm
Front PMSM min torque	-10 Nm	-32.1 Nm	-20 Nm
Front PMSM RMS torque	7.9 Nm	13.4 Nm	7.9 Nm
Front PMSM max speed	16 720 RPM	16 741 RPM	16 559 RPM
Front PMSM RMS speed	11 136 RPM	10 608 RPM	11 082 RPM
Rear PMSM max power	15.9 kW	15.9 kW	15.9 kW
Rear PMSM min power	-3.7 kW	-10.1 kW	-6.4 kW
Rear PMSM RMS power	10.6 kW	10.1 kW	10.4 kW
Rear PMSM max torque	16.3 Nm	16.6 Nm	16.4 Nm
Rear PMSM min torque	-3.2 Nm	-8.6 Nm	-5.6 Nm
Rear PMSM RMS torque	9.7 Nm	9.8 Nm	9.7 Nm
Rear PMSM max speed	16 727 RPM	16 757 RPM	16 575 RPM
Rear PMSM RMS speed	10 908 RPM	10 472 RPM	10 869 RPM
Battery max power	63.8 kW	68.7 kW	67.1 kW
Battery max charging power	-30.4 kW	-81.1 kW	-52.1 kW
Battery RMS power	46.1 kW	46.5 kW	45.4 kW

Table 15: Acceleration drive cycles results with 1:16 gear ratio where the performance requirements for the front and rear PMSMs are shown and the battery powerflow is also shown

Parameters	Acceleration 1	Acceleration 2	Acceleration 3
Front PMSM max power	17 kW	18.6 kW	18.2 kW
Front PMSM min power	-11.9 kW	-31.9 kW	-20.5 kW
Front PMSM RMS power	11.5 kW	13 kW	11.4 kW
Front PMSM max torque	9 Nm	9.2 Nm	8.8 Nm
Front PMSM min torque	-8.6 Nm	-28.3 Nm	-17.3 Nm
Front PMSM RMS torque	6.8 Nm	11.7 Nm	6.8 Nm
Front PMSM max speed	19 109 RPM	19 140 RPM	18 931 RPM
Front PMSM RMS speed	12 716 RPM	12 110 RPM	12 656 RPM
Rear PMSM max power	15.8 kW	15.8 kW	15.7 kW
Rear PMSM min power	-3.5 kW	-10.2 kW	-6.4 kW
Rear PMSM RMS power	9.5 kW	10.1 kW	10.5 kW
Rear PMSM max torque	14.2 Nm	14.5 Nm	14.3 Nm
Rear PMSM min torque	-3 Nm	-7.8 Nm	-5.0 Nm
Rear PMSM RMS torque	8.4 Nm	8.6 Nm	8.4 Nm
Rear PMSM max speed	19 117 RPM	19 152 RPM	18 944 RPM
Rear PMSM RMS speed	12 456 RPM	11 951 RPM	12 411 RPM
Battery max power	64.5 kW	70.3 kW	68.7 kW
Battery max charging power	-29.3 kW	-80.5 kW	-51.3 kW
Battery RMS power	46.7 kW	46.8 kW	45.9 kW

6.3 Drive cycle analysis summary and finalized design parameters

The drive cycle data obtained indicate that the largest torque requirements on the front motors will occur in regenerative braking. The largest minimum torques required from the motors according to the drive cycle simulations occurred during the optimum lap simulation where -37.3 Nm was with a 1:12 gear ratio was used. Also a similar value was obtained from the Endurance 3 drive cycle where the minimum torque was -37 Nm. These torque magnitudes are much larger than that of the acceleration simulations where in the acceleration events the maximum torque was 12.6 Nm and was obtained in Acceleration 2. Both in Autocross 1, 2, optimum lap, Endurance 1 and 3 the maximum torque reached when accelerating was 13.3 Nm with a 1:12 gear ration. That is still substantially lower than the minimum torque previously mentioned. In order to determine the maximum torque of required from the motors, torque curves of the optimum lap simulation and Endurance 3 drive cycles must be studied in detail. The plots are shown in Figure 28 and 29 and it can be seen that the torque magnitude exceed 20 Nm a total of 25 times during the optimum lap simulation.

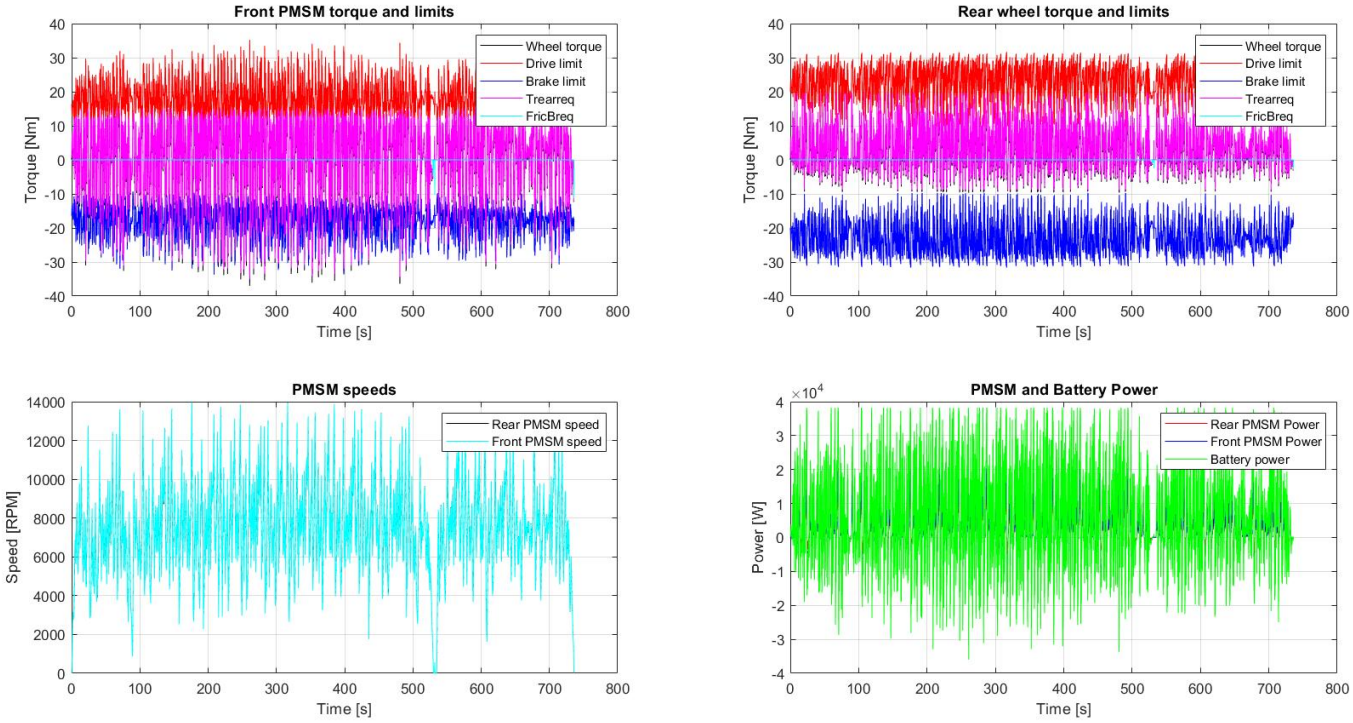

Figure 28: Endurance 3 simulation results using a 1:12 gear ratio where the front and rear PMSM torque, traction limits, references and mechanical brake torque. Also the PMSM speeds and powerflow for one front and rear motors are shown

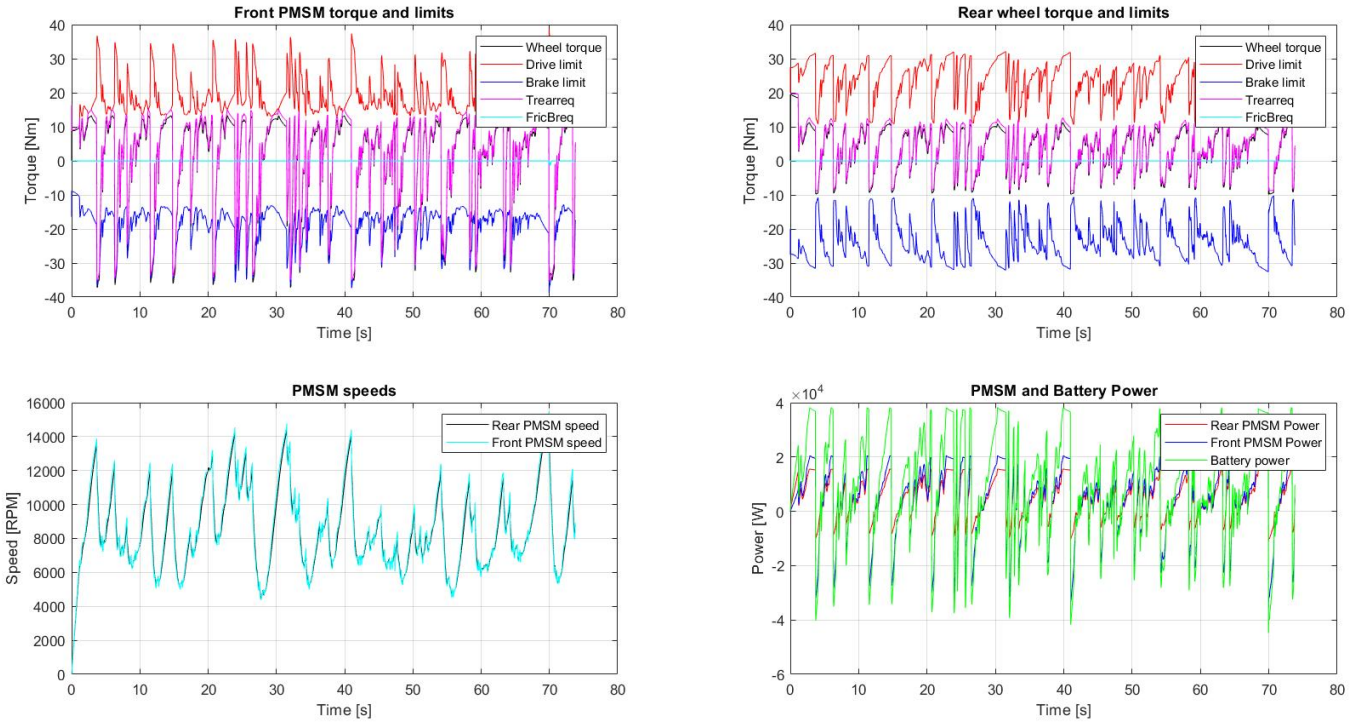

Figure 29: Optimum lap simulation result using a 1:12 gear ratio where the front and rear PMSM torque, traction limits, references and mechanical brake torque. Also the PMSM speeds and powerflow for one front and rear motors are shown

From these results it becomes apparent that the motors would need to be up sized in order to be able to cover all torques. The question now has to be raised weather the large negative torques is necessary or even possible to fully utilize in the real car. The first point that should be discussed is the used gear ratio which currently is 1:14 in the car. However there are plans to change the gear ratio to 1:13 for the 2021 season with a new wheel assembly and then to 1:15 for the 2022 season with a new gearbox design. Therefore it can be concluded that the torque magnitudes required for the 1:12 gear ratio likely is not needed. That does however indicate that studying the requirements between gear ratios of 1:12 to 1:16 would ensure that the requirements for the 2021 and 2022 seasons are covered. The second point which must be discussed is the charging capabilities of the battery. Currently the CFS battery has charging capabilities of about 7.3 kW continuously and a peak power of 14.8 kW according to the cell manufacturer. Comparing that to the results seen in the power plots in Figures 27, 25, 26, 28 and 29, it can be noted that the number is much lower than the power that just one front motor is able to regenerate. Also the plots only show the battery power to one set of PMSMs which means that the actual battery power will be twice as much. In Tables 10, 7, 11, 8, 12 and 9 it is shown that the maximum charging power is much higher than what is specified in the datasheet. In addition to that it can also be seen that the RMS powers also exceed the maximum allowed power. However, there has been instances where the Formula Student teams have been able to up-rate their battery cells which allowed them to charge with higher current and hence is able to regenerate more power. An increase of the charge current of lithium battery cells could however impact the lifetime of the cells due to increased stresses on the cells. It is not possible to speculate about if it is possible to up-rate the specific battery used in the Formula Student 2021 car so in order to avoid having to re-design the motors for future battery packs, it will be assumed that it will be possible to charge it with 80 kW. Another aspect which should be considered is how frequently the front motors reach certain torque levels. In order to do that the time distribution for the torques of the

Endurance 3 and optimum lap simulation drive cycles with a 1:12 gear ratio is shown in Figures 31 and 30.

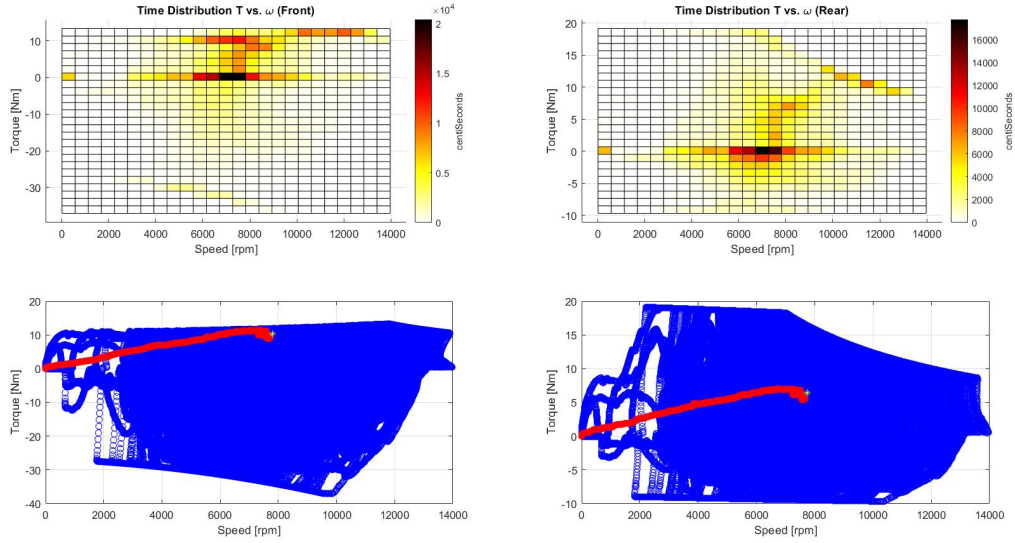

Figure 30: Endurance 3 simulation time distribution map using a 1:12 gear ratio where all of the torque/speed datapoints are shown for the front and rear PMSMs and how much time is spent at each speed/torque combination

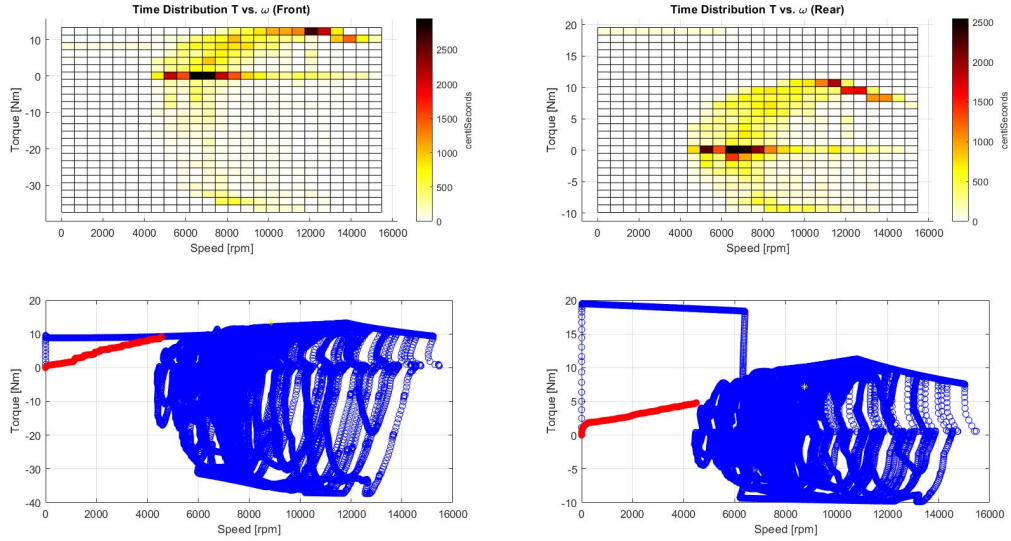

Figure 31: Optimum lap simulation time distribution map using a 1:12 gear ratio where all of the torque/speed datapoints are shown for the front and rear PMSMs and how much time is spent at each speed/torque combination

The time distribution for the torque in the Endurance 3 drive cycle indicates that most of the torques are distributed within 0-20 Nm. In the case of the Optimum lap simulation, the prevalence at higher torques is slightly higher for the larger negative torques. From this it was concluded that a suitable maximum torque for the new front PMSM would be 20 Nm. The required rated torque from the machine will depend on the gear ratio as well and is more difficult to choose. Instead of specifying one specific value, a range is specified for different gear ratios where the motor should achieve a certain efficiency. That would ensure that the motor would not overheat if the gear ratio were changed in the future. When studying the rated power requirements of the PMSM, there is one datapoint which is deviating which is that of the optimum lap simulation where it is much higher than the other drive cycles. Since the optimum lap is of shorter duration than Autocross 1 and Autocross 2 it might be the case that having a lower rated power than what is indicated by the optimum lap simulation. Also it is unlikely that the motor would overheat from being operated at levels slightly higher than what it is rated for a duration less than two minutes. The endurance drive cycles are more important and the drive cycle Endurance 3 indicate that a minimum rated power of 8.7 kW would be required. A safety margin of 2 kW was added to the rated power to ensure that no overheating issues would occur which would equate to a rated power of about 11 kW. The maximum speed of the machine was unchanged compared to the CFS17 PMSM since the driving cycles presented in Table 15 would indicate that the car reaches its maximum speed at around 19 200 RPM. The maximum speed of the old CFS17 PMSM is 20 000 RPM.

Finding the speed at which the motor should enter field weakening is very difficult. The 1-D powertrain model has a built-in field weakening algorithm as can be seen in Figure 30 and 31 and in that may need to be removed in order to see where the motor will enter its constant power region. As mentioned in Section 4.1.2, using concentrated windings can cause some problems with controlling the motor in the field weakening region which would indicate that it would be beneficial to have the rated speed above the RMS speed. The RMS speeds indicated in Tables 9 and 12 that the rated speed should exceed 11 800 RPM. A safety margin of 200 RPM was added which then sets the target rated speed as 12 000 RPM. The rated torque is calculated to 8.7 Nm at the rated speed with the given rated power and the maximum power is calculated to 25 kW. The performance specification which the PMSM will be designed after is specified in Table 16.

Table 16: Performance requirements of the new PMSM obtained from the drive cycle analyses

Parameter	Value
Rated torque	8.7 Nm
Maximum torque	20 Nm
Rated speed	12 000 RPM
Maximum speed	20 000 RPM
Rated power	11 kW
Maximum power	25 kW

7 Design iterations to improve the PMSM and Results

This section will describe the design modifications to the CFS17 PMSM to tailor it to be used as a front motor in the CFS car. The design process will be iterative where changes will be implemented and evaluated and based on the evaluation, further design changes are implemented. The design is looped until a satisfactory PMSM design is achieved which lacks obvious shortcomings which impairs the functionality of the motor. The minimum requirement for a completed design is that the PMSM should fulfil the performance requirement specified in Table 16. Once the requirements have been fulfilled, further iterations can be made to increase efficiency and/or decrease weight.

When initializing the re-design of the CFS17 PMSM, some design parameters should seek to be kept since they would have major impacts on other parameters which may lead to a complete redesign. There are also some parameters which should not be changed on the basis that the performance improvements would not be significant enough to motivate making them. The first parameter which was to remain unchanged was the number of rotor poles. The reason for this is that the mechanical strength of the rotor will be affected by that as discussed in Section 4.2. Since the pole number would be unchanged in order to maintain the number of slots per pole per phase, the slot number would not be changed. That is because it is desirable to have the lowest order harmonic to be the working harmonic and hence the one that is producing torque as discussed in Section 4.2. That also means that the harmonic content in the motor should remain similar to the CFS17 motor. For the same reason as the two parameters above, concentrated windings will be kept with the new design. Concentrated windings will also weigh less compared to distributed. Even though there could be some benefits of having distributed windings in the field weakening region, having higher power density and lower weight is more important for applications within Formula Student. The suspension and wheel assembly group requested that the outer stator diameter should not increase which was because of the issues that would cause with the wheel assembly in terms of packaging. For that reason, the outer diameter must not be increased. After conducting the literature study summarized in Section 4.4, it was found that the potential performance improvements when changing the rotor-magnet topology would not provide enough benefits to be able to motivate investing the time required in order to re-design the entire rotor. However, that could be an area of interest for Chalmers Formula Student. The stator slot opening will influence the harmonics in the flux and the MMF and hence the cogging and ripple torque as well as the harmonics of the phase voltage. Should CFS see any benefit in changing the slot opening an in-depth study will have to be conducted in order to see if it the harmonics could be reduced. The end winding insulation will not be changed due to time restrictions and no study has been conducted in what improvements changing the end winding insulation could bring. The end winding insulation could possibly improve the cooling of the windings but there are changes that could have more significant impacts on the thermal behaviour such as reducing copper losses.

The material of the stator is to remain unchanged since it was changed for the CFS17 motor and it is already using an iron cobalt alloy which allows for high flux densities. Changing to a material with a higher concentration of cobalt could potentially increase the cost of the stator also. The rotor material could be changed in order to reduce the copper losses at higher torques due to a reduction in reluctance at higher magnetic flux which means that the total MMF needed would be reduced and therefore a lower current would be needed. There are however more considerations to be made apart from the magnetic circuit as discussed in section 4.2 such as the mechanical aspect of the rotor such as thermal expansion and strength. For that reason, the rotor material would be kept. The rotor shaft is also a part of the mechanical design, of the motor and the dimensions of that should also remain unchanged since a change in that does not only require a more in-depth mechanical design but it could also have considerable effects on the systems surrounding such as the gearbox, encoder housings and bearings. The slot insulation material will not be changed in this design but could be a subject of interest in the future to improve the cooling of the copper wires in the slots. In order to not increase the difficulty of winding the motor by hand, it was decided that the fill factor would at least not increase. The airgap should also not be changed since the machine is operating at high speed and hence, reducing the airgap could lead to decreased reliability as seen in Section 4.3. Increasing the airgap would however lead to lower power density in the motor. For

that reason, the airgap will be kept the same. All of the locked parameters are presented in Table 17.

Table 17: Locked design parameters of the new PMSM design which should not be changed

Parameter	Must be
Number of Pole pairs p	=3
Number of slots N_{slot}	=9
Winding type	Concentrated
Outer stator diameter OD_{stator}	$\leq$ 90 mm
Rotor topology	Flat IPM
Stator and rotor material	Unchanged
Slot opening width	Unchanged
End Winding insulation	Unchanged
Fill factor	$\leq$ 0.4
Airgap length l_{gap}	= 0.5 mm

7.1 FEM modelling of the CFS17 motor in Ansys maxwell

The original FEM model of the CFS17 motor was provided by AROS Electronics and is shown in Figure 4a. The model is controlled by selecting the mechanical speed in the motion setup and feeding the coils with an ideal sinusoidal current with a specified amplitude, dq-angle and frequency. The simulation duration is also specified. The angle is given relative to the q-axis which means that setting the angle to zero would mean that the q-axis current is the full supplied current magnitude.

When making changes in the FEM model, the core loss calculation will be reset and hence will need to be manually set in order for the calculation output to be correct. The 2D-model used will also not provide accurate results and correction factors are required to be used in the post processing of the results. The model uses current excitation which means that the input phase currents are manually set in the model. The current waveform used was an ideal sinusoidal wave without any harmonics which will not be the case in reality since the motor will be supplied using a PWM drive. The additional high-frequency current harmonics present when using a PWM drive will cause additional iron and magnet losses [45]. The proximity and skin effects are also not taken into account which means that the copper losses could be underestimated. Also, the magnet segmentation is not accounted for in the Eddy current loss calculation which means that the Eddy current losses in the magnets can be overestimated [46]. In order to account for the above mentioned inaccuracies, a correction factor of 1.7 was used on the stator iron losses after consultation with Johan Åström. Since magnet losses can be significantly influenced by the supply and that the magnet segmentation is not accounted for, no correction factor was used for the total rotor losses (iron and magnet losses).

When conducting the simulations, the interesting data obtained is the losses of the machine, the phase voltage and the power output. Also, the location of the losses is of interest. The first simulations performed was a performance analysis at rated power in order to estimate the efficiency of the motor. The results from this simulation is presented in Chapter 8.1.2. The second simulation conducted is a maximum power simulation where the expected maximum torque is obtained, the phase voltage at base speed and the efficiency. This simulation is performed at 11 900 RPM for all motors. The cogging torque was also checked by running the motor at a 11 900 RPM without feeding the motor with any current. The final simulations performed running the motor at a number of speeds and torques to obtain the efficiency map of the motor. One problem with obtaining the efficiency maps was that it was very time consuming and hence could not be done for all of the motor concepts. In the end, three efficiency maps were obtained and all the data from those simulations will be presented in under the respective motors.

7.1.1 Peak torque operation of the CFS17 PMSM

The peak torque operation of the CFS17 motor was investigated in order to obtain the maximum torque that the motor could be operated at and to study the phase voltage waveforms. A RMS current of 125 A and a current angle β of 90^o was used for the CFS17 motor. Since the maximum torque is of the CFS17 motor is known, the current just had to be tuned to reach the specified torque. Using a current angle of 90^o means that the full current magnitude will be in the q-direction as stated in (78) and (79). In Figure 32, the torque curve at 11 900 RPM is plotted where a total of 2.38 electric cycles. What also should be seen is that the torque is not constant and that is caused by the variation in machine flux. The flux varies due to the varying MMF from the coils since it is supplied with AC and the varying reluctance as a result of the different rotor positions. The peak-to-peak torque ripple was in this case about 30 % of the average torque of the machine. One important aspect to note from these plots is that the average torque will depend on if full electric periods are plotted or not. In this project it was not and hence there may be some deviations in the torque between different speeds. For that reason it is important that simulations which are to be compared to each other is to be done at the same speed.

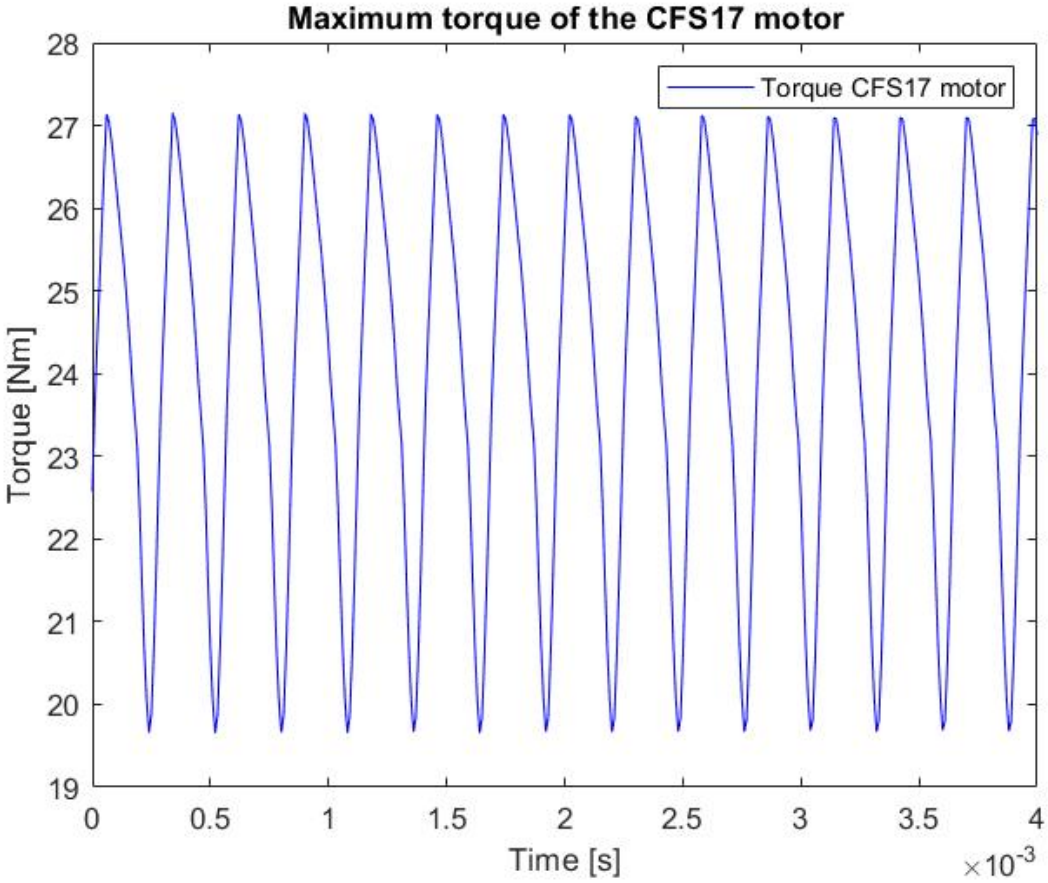

Figure 32: CFS17 motor operating at 11 900 RPM while being supplied with a phase current of 125 A RMS and a current angle of 90^o where it produces an average torque of 24.1 Nm

In the Figure 33, the phase voltage from the three phases is plotted for 2.38 electric periods. The voltage consists of the induced voltage caused by the change in flux linkage and the resistive voltage drop. This voltage is described in (35), (36) and (37).

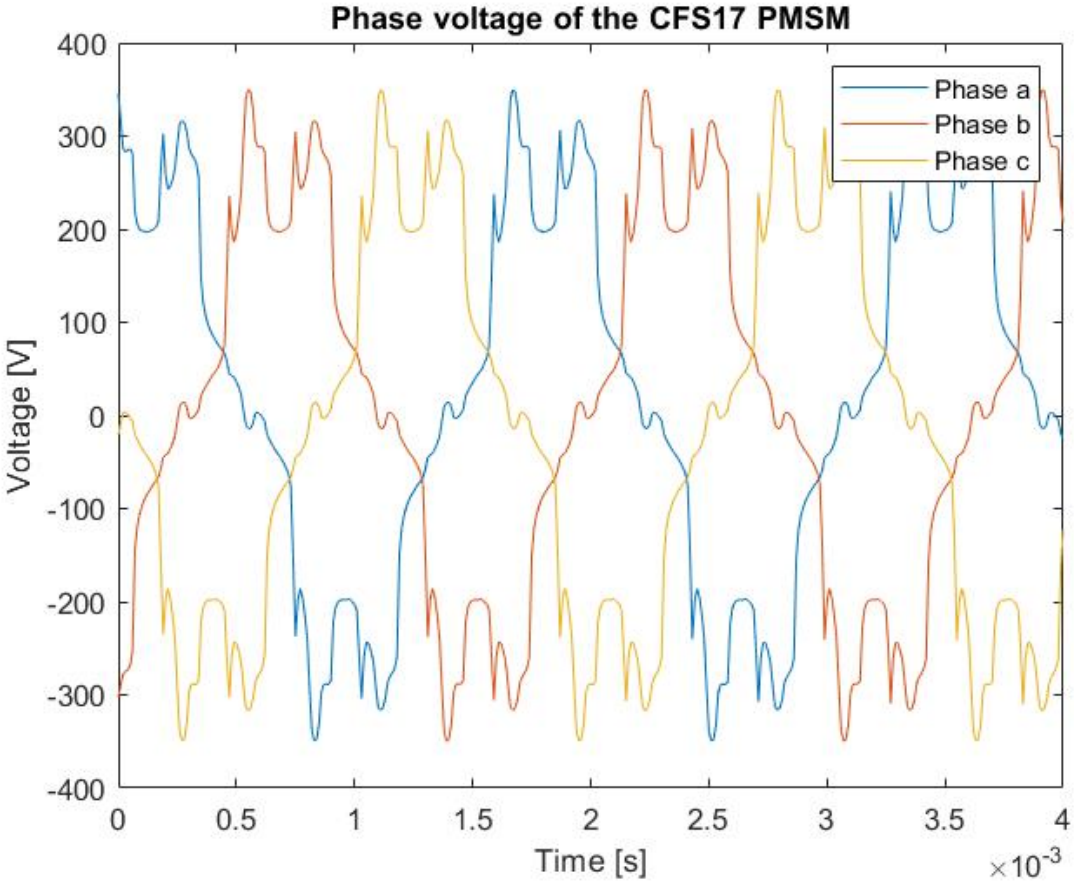

Figure 33: Phase voltage from the three phases of the CFS17 PMSM when operating at 11 900 rpm and 24.1 Nm

What can be noted in this Figure 33 is also that the waveforms are not sinusoidal and there seem to be significant harmonic content in the voltage. In order to get a better view of the fundamental component of the voltage and the harmonic content, an FFT was performed which is shown in Figure 34. It can be noted from the FFT plot that the first large peak in the voltage occurs at approximately 3 kHz which also where the 5:th harmonic is expected to be. The second peak occurs at about 4.2 kHz which is where the 7:th order harmonic is expected to occur. The magnitude of the fundamental of the CFS17 PMSM is 265.4 V, for the 5:th harmonic it is 63 V and for the 7:th harmonic it is 31.68 V.

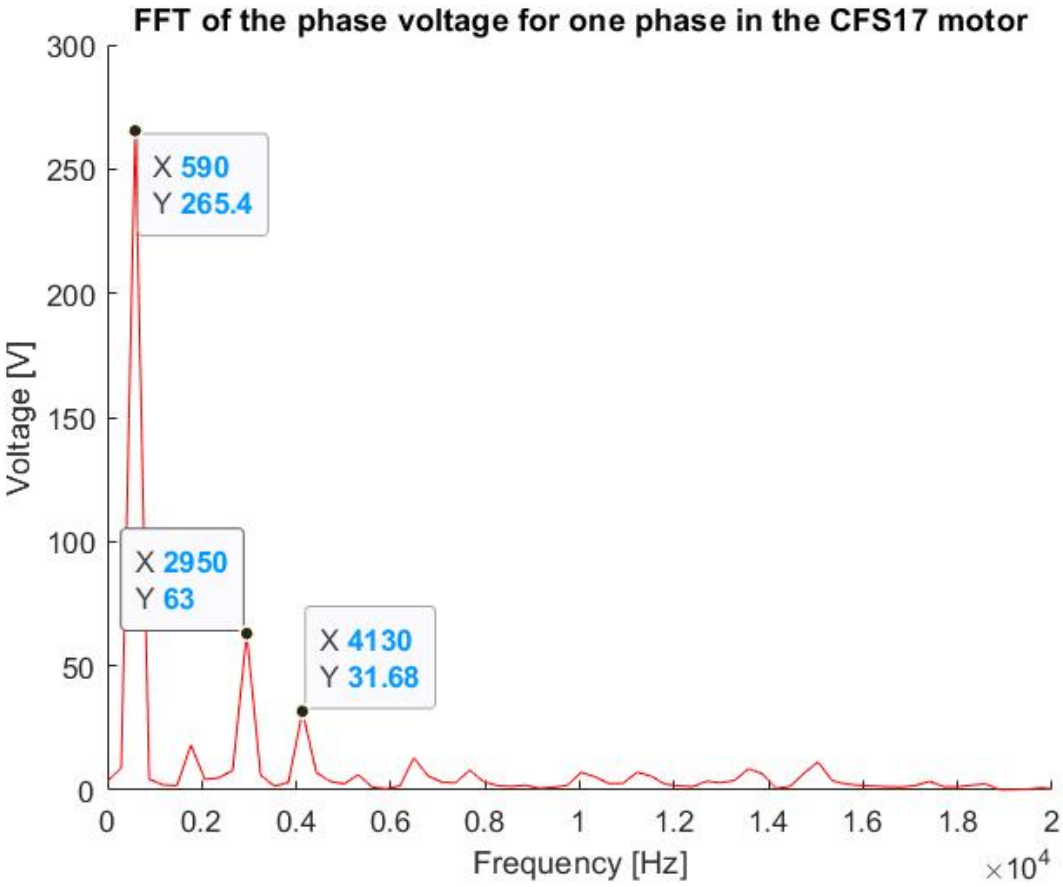

Figure 34: FFT of the phase voltage from one of the phases in Figure 33 coming from CFS17 PMSM when operating at 11 900 RPM and 24.1 Nm

Additionally, in the torque plot shown in Figure 32 it can be seen that there may be some cogging torque present. These indications become more prevalent at lower torque magnitudes. As mentioned, the cogging torque is one part which is causing the ripple torque during operation. The cogging torque can be investigated by running the model at a constant speed but setting the current magnitude to zero. The results from the FEM model show that the cogging torque is slightly lower than 1 % of the maximum torque of the machine as can be seen in Figure 35. Since mechanical vibrations is not of great concern for a Formula style racing car, this lever of cogging torque is deemed as acceptable.

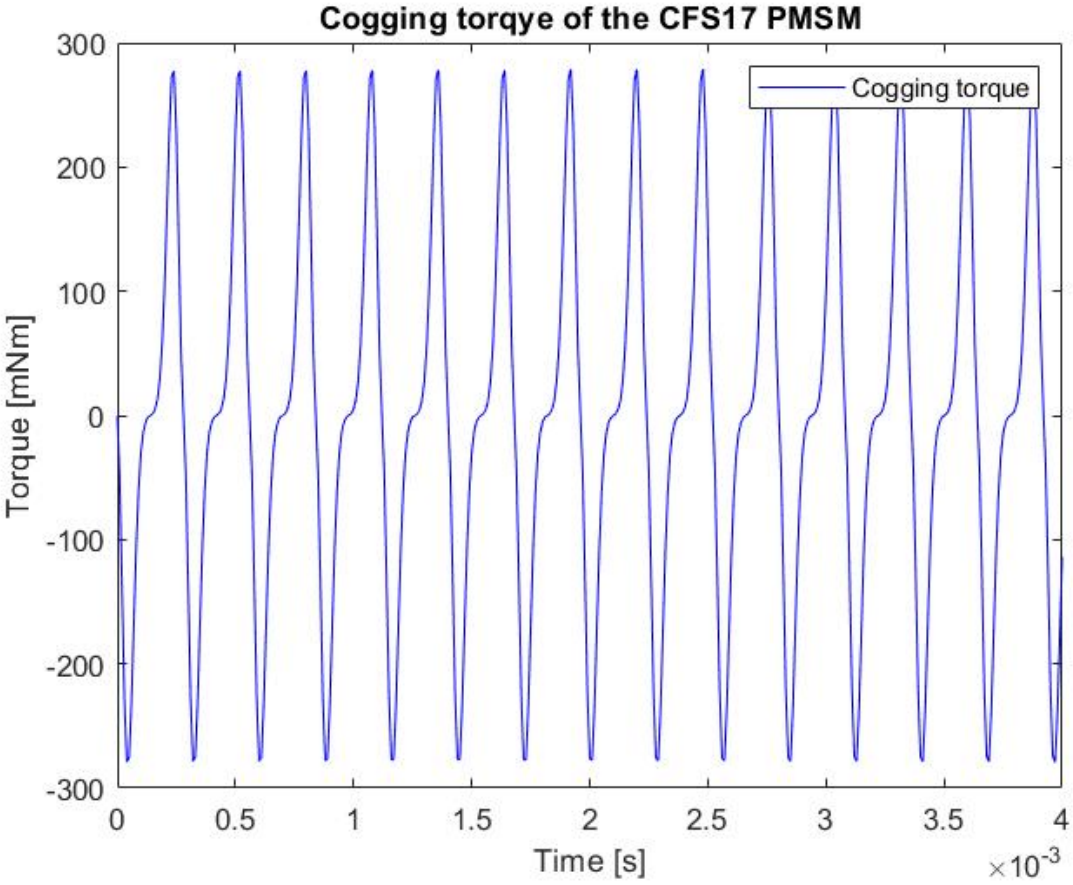

Figure 35: Cogging torque of the CFS17 motor operating at 11 900 RPM where the supply current has been set to zero

7.1.2 Losses for the CFS17 PMSM

Due to some inconsistencies in the old power loss data from the FEM model compared to what the model gave when running it with a newer version of the software, the data was updated in order to get a more accurate comparison between the versions. The temperature of the motor was set to 150^o C because that is the temperature at which the CFS17 motor should reach equilibrium at rated operation and also the temperature where the magnets in theory will demagnetize. Using a higher temperature will mainly affect the windings where the resistance will increase as shown in (86). The higher wire resistance will give a better indication of the actual resistance which will be experienced when the motor run for a long duration. These data points would also be used to obtain the efficiency maps of the different design concepts. In Tables 18, 19, 20, 21, 22 the loss data are presented. The first thing that can be noted is that the current magnitudes are independent of the speed of the machine. That is because the current which is fed to the motor will only influence the torque as seen in (76). From that it can be concluded that the torque will mainly influence the copper losses in the machine so as the torque increase, the copper losses increase. What also should be noted is that the stator iron and rotor iron losses increase as the speed increases and that is caused by the increase in magnetizing frequency as stated in (89), (91) and (90). The Eddy current losses have the highest speed dependence where it is proportional to the frequency squared and hence will increase faster that the excess or hysteresis losses. When the current angle is changed, the current magnitude needs to be changed in order to maintain the torque of the machine. The current magnitude and the angle will influence the flux density in the machine therefore the iron losses will also be influenced by the current angle. The current angle at which the lowest current is achieved for a given torque is not the same across the torque span. In Table 22 and 21 it can be noted that the lowest current is achieved at 15^o for 16 Nm and at 35^o for 20 Nm and that is due to the MTPA being non-linear and the angle will gradually increase at higher torques.

Table 18: Speed sweep at 6 Nm for three current angles for the CFS17 PMSM where the copper, stator iron and rotor iron losses were obtained

Speed	Current angle	Current magnitude	Copper losses	Iron losses	Rotor losses
5000	15^o	30.76 A	120 W	121 W	18 W
5000	35^o	32.53 A	134 W	106 W	15 W
5000	45^o	35.78 A	162.6 W	102 W	15 W
8000	15^o	30.76 A	120 W	265 W	39 W
8000	35^o	32.53 A	134 W	234 W	34 W
8000	45^o	35.78 A	162.6 W	227 W	28 W
11000	15^o	30.76 A	120 W	422 W	67 W
11000	35^o	32.53 A	134 W	380 W	59 W
11000	45^o	35.78 A	162.6 W	376 W	57 W
14000	15^o	30.76 A	120 W	612 W	104 W
14000	35^o	32.53 A	134 W	551 W	91 W
14000	45^o	35.78 A	162.6 W	549 W	75 W
16000	15^o	30.76 A	120 W	752 W	132 W
16000	35^o	32.53 A	134 W	647 W	115 W
16000	45^o	35.78 A	162.6 W	583 W	95 W
18000	15^o	30.76 A	120 W	914 W	119 W
18000	35^o	32.53 A	134 W	823 W	144 W
18000	45^o	35.78 A	162.6 W	820 W	139 W
20000	15^o	30.76 A	120 W	1077 W	200 W
20000	35^o	32.53 A	134 W	975 W	174 W
20000	45^o	35.78 A	162.6 W	975 W	168 W

Table 19: Speed sweep at 12 Nm for three current angles for the CFS17 PMSM where the copper, stator iron and rotor iron losses were obtained

Speed	Current angle	Current magnitude	Copper losses	Iron losses	Rotor losses
5000	15^o	59.82 A	455 W	162 W	26 W
5000	35^o	62.22 A	492 W	151 W	21 W
5000	45^o	66.47 A	561 W	153 W	21 W
8000	15^o	59.82 A	455 W	356 W	55 W
8000	35^o	62.22 A	492 W	340 W	47 W
8000	45^o	66.47 A	561 W	351 W	48 W
11000	15^o	59.82 A	455 W	572 W	98 W
11000	35^o	62.22 A	492 W	562 W	80 W
11000	45^o	66.47 A	561 W	599 W	82 W
14000	15^o	59.82 A	455 W	841 W	153 W
14000	35^o	62.22 A	492 W	830 W	123 W
14000	45^o	66.47 A	561 W	889 W	124 W
16000	15^o	59.82 A	455 W	1029 W	198 W
16000	35^o	62.22 A	492 W	1031 W	156 W
16000	45^o	66.47 A	561 W	1123 W	158 W
18000	15^o	59.82 A	455 W	1251 W	242 W
18000	35^o	62.22 A	492 W	1256 W	195 W
18000	45^o	66.47 A	561 W	1367 W	197 W
20000	15^o	59.82 A	455 W	1478 W	297 W
20000	35^o	62.22 A	492 W	1491 W	235 W
20000	45^o	66.47 A	561 W	1631 W	236 W

Table 20: Speed sweep at 14 Nm for three current angles for the CFS17 PMSM where the copper, stator iron and rotor iron losses were obtained

Speed	Current angle	Current magnitude	Copper losses	Iron losses	Rotor losses
5000	15^o	70 A	622 W	174 W	29 W
5000	35^o	72.1 A	661 W	162 W	23 W
5000	45^o	78.63 A	785 W	168 W	24 W
8000	15^o	70 A	622 W	383 W	62 W
8000	35^o	72.1 A	661 W	365 W	51 W
8000	45^o	78.63 A	785 W	389 W	54 W
11000	15^o	70 A	622 W	615 W	113 W
11000	35^o	72.1 A	661 W	602 W	87 W
11000	45^o	78.63 A	785 W	665 W	92 W
14000	15^o	70 A	622 W	908 W	175 W
14000	35^o	72.1 A	661 W	894 W	134 W
14000	45^o	78.63 A	785 W	990 W	140 W
16000	15^o	70 A	622 W	1114 W	223 W
16000	35^o	72.1 A	661 W	1110 W	169 W
16000	45^o	78.63 A	785 W	1251 W	178 W
18000	15^o	70 A	622 W	1356 W	276 W
18000	35^o	72.1 A	661 W	1356 W	212 W
18000	45^o	78.63 A	785 W	1528 W	222 W
20000	15^o	70 A	622 W	1607 W	341 W
20000	35^o	72.1 A	661 W	1610 W	256 W
20000	45^o	78.63 A	785 W	1824 W	266 W

Table 21: Speed sweep at 16 Nm for three current angles for the CFS17 PMSM where the copper, stator iron and rotor iron losses were obtained

Speed	Current angle	Current magnitude	Copper losses	Iron losses	Rotor losses
5000	15^o	81.5 A	843 W	184 W	29 W
5000	35^o	83 A	875 W	174 W	25 W
5000	45^o	89.8 A	1024 W	185 W	27 W
8000	15^o	81.5 A	843 W	407 W	63 W
8000	35^o	83 A	875 W	395 W	56 W
8000	45^o	89.8 A	1024 W	429 W	60 W
11000	15^o	81.5 A	843 W	656 W	114 W
11000	35^o	83 A	875 W	654 W	95 W
11000	45^o	89.8 A	1024 W	736 W	102 W
14000	15^o	81.5 A	843 W	970 W	178 W
14000	35^o	83 A	875 W	974 W	147 W
14000	45^o	89.8 A	1024 W	1099 W	157 W
16000	15^o	81.5 A	843 W	1195 W	226 W
16000	35^o	83 A	875 W	1212 W	186 W
16000	45^o	89.8 A	1024 W	1388 W	199 W
18000	15^o	81.5 A	843 W	1458 W	280 W
18000	35^o	83 A	875 W	1483 W	233 W
18000	45^o	89.8 A	1024 W	1695 W	249 W
20000	15^o	81.5 A	843 W	1729 W	346 W
20000	35^o	83 A	875 W	1762 W	281 W
20000	45^o	89.8 A	1024 W	2025 W	298 W

Table 22: Speed sweep at 20 Nm for three current angles for the CFS17 PMSM where the copper, stator iron and rotor iron losses were obtained

Speed	Current angle	Current magnitude	Copper losses	Iron losses	Rotor losses
5000	15^o	109 A	1506 W	213 W	32 W
5000	35^o	104 A	1376 W	207 W	30 W
5000	45^o	113.4 A	1626 W	229 W	33 W
8000	15^o	109 A	1506 W	477 W	68 W
8000	35^o	104 A	1376 W	469 W	67 W
8000	45^o	113.4 A	1626 W	531 W	75 W
11000	15^o	109 A	1506 W	782 W	122 W
11000	35^o	104 A	1376 W	783 W	114 W
11000	45^o	113.4 A	1626 W	915 W	128 W
14000	15^o	109 A	1506 W	1160 W	190 W
14000	35^o	104 A	1376 W	1169 W	177 W
14000	45^o	113.4 A	1626 W	1370 W	195 W
16000	15^o	109 A	1506 W	1442 W	242 W
16000	35^o	104 A	1376 W	1456 W	224 W
16000	45^o	113.4 A	1626 W	1728 W	247 W
18000	15^o	109 A	1506 W	1763 W	299 W
18000	35^o	104 A	1376 W	1783 W	282 W
18000	45^o	113.4 A	1626 W	2110 W	311 W
20000	15^o	109 A	1506 W	2095 W	370 W
20000	35^o	104 A	1376 W	2122 W	339 W
20000	45^o	113.4 A	1626 W	2522 W	372 W

7.2 Design concept 1, reduction in stack length

The first version of the new motor was to reduce the stack length. That would mean that the flux density distribution in the motor would be unchanged since the reluctance would be equally increased in all parts of the machine for a given flux. The first version of the stack length reduction model only changed the length and did not change the winding layout or the magnets in the rotor. That means that for a given current, the total flux in the stator will decrease and hence a lower phase voltage is obtained and a lower torque is produced. In general the torque produced by a given machine will scale linearly to the stack length of the machine since the stack length will influence the reluctance of each part in the machine equally as specified in (26). That is because the cross-section area of the flux path will be equally influenced by the change of stack length for all parts of the machine. So in order to obtain the correct torque of the new PMSM concept according to the new specification in Table 16 the stack length can be reduced by 17 %. That in practice means that decreasing the stack length from 70 mm to 58.1 mm. The stack length was set to 59 mm for the first concept to have some safety margin. The original FEM model seen in Figure 23 of the CFS17 motor was used when designing this new version of the motor, but with the reduced stack length.

The first problems that did arise when editing the model was that the BH-curves of the materials used was removed when a newer version of the software was used and hence, they had to be manually added again in order to be able to run any simulations. Also, it was important to extrapolate the curves to cover higher levels of flux density than what is defined in the material datasheets. The reason for that is that there could occur point in the model where that high levels of flux density is achieved and if there is no defined point in the BH-curve for that flux density, the simulation will not be able to run. The maximum torque that the motor can produce under the same operating conditions as in Figure 32 is shown in Figure 36. As can be seen, the average torque is reduced to 20.3 Nm which just above the desired torque of 20 Nm which is expected since a safety margin was added onto the calculated 58.1 mm. It should also be noted that the torque was 1.5 % higher than what was desired which is roughly the same as percentage that was added on as a safety margin. From that it should be noted that there should be some room for further changes should it be desired and that very minor changes to the flux path can have a large impact on the torque that the machine is able to produce.

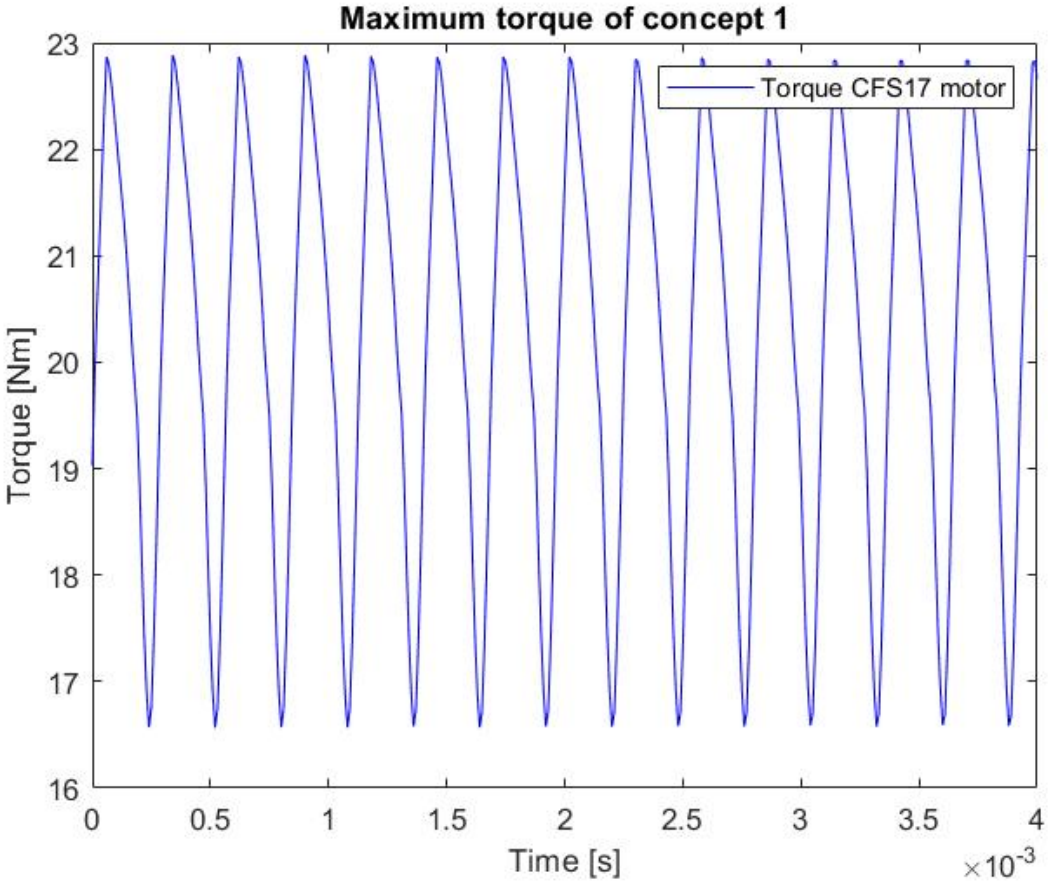

Figure 36: Iteration 1 of the PMSM with a reduced stack length operating at 11 900 RPM while being supplied with a phase current of 109 A RMS and a current angle of 90^o where it produces an average torque of 20.3 Nm

Due to the reduction in overall flux in the machine, the phase voltage is reduced which can be seen in Figure 37. The voltage depends according to (35), (36) and (37) on the restive voltage drop over the copper and on the rate of change of the flux linkage in the machine. Since the wire length has been reduced, the copper resistance will be reduced according to (85), the restive voltage drop will be reduced. Also the overall flux in the machine is reduced which means that the voltage drop caused by the rate of change in the flux linkage will also be scaled linearly with the flux since the number of turns is not changed. In order to get a better view of the phase voltage an FFT was again conducted which can be seen in Figure 38.

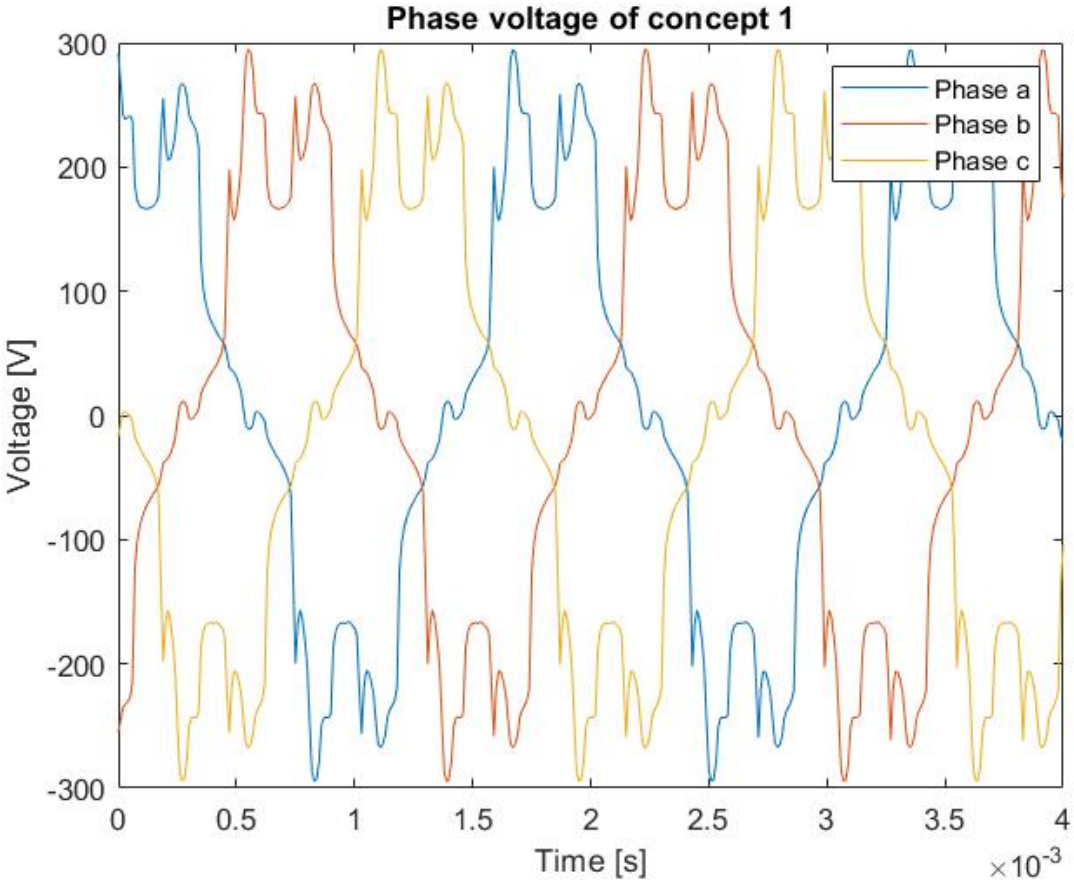

Figure 37: Phase voltage from the three phases of iteration 1 of the PMSM with reduced stack length when operating at 11 900 rpm and 20.3 Nm

The fundamental part of the phase voltage reaches a magnitude of 224 V which means that the voltage has been reduced by 15.6 %. That is almost the same as the reduction in the stack length which was of 15.7 %. the 5:th order harmonic was reduced by 15.7 % to 53.1 V and the 7:th order by 15.4 % to 26.7 V. From that it can be seen that the voltage scales in about the same manner as that of the torque given that the number of coil turns are unchanged.

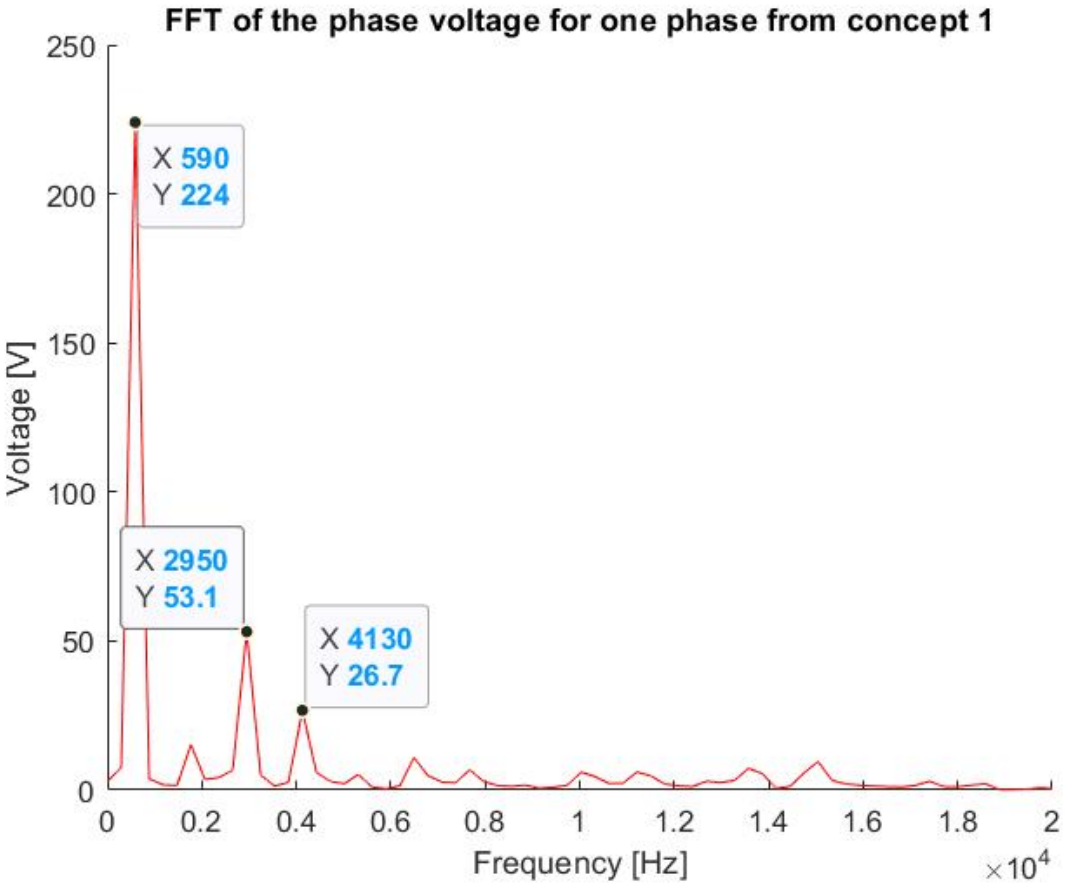

Figure 38: FFT of the phase voltage from one of the phases in Figure 37 coming from iteration 1 of the PMSM with reduced stack length when operating at 11 900 rpm and 20.3 Nm

Next the cogging torque was examined in order to see how it was affected by the reduction in stack length. The cogging torque is shown in Figure 39 where it can be noted that the magnitude of the cogging torque peak-to-peak ripple is reduced from 546 mNm to 470 mNm which is a decrease of 14 %.

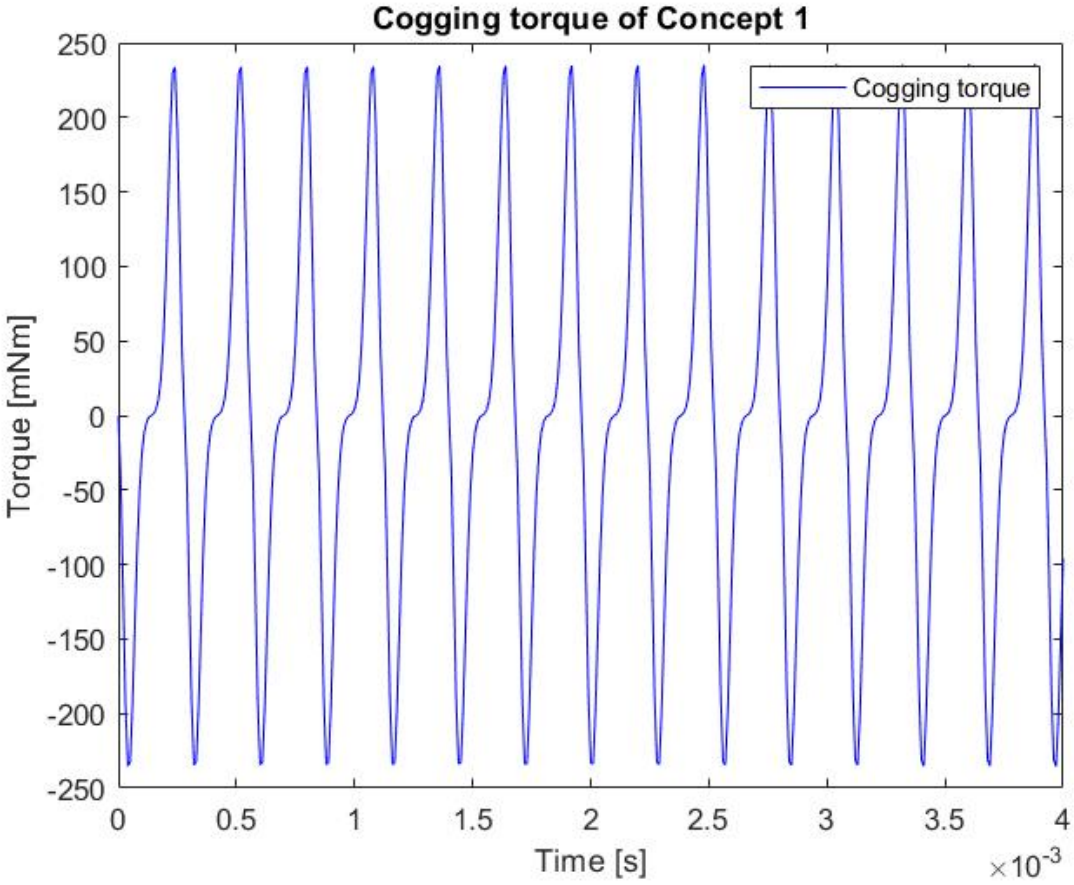

Figure 39: Cogging torque of iteration 1 of the PMSM with the reduced stack length operating at 11 900 RPM where the supply current has been set to zero

7.3 Design concept 2, reduction in outer diameter of the stator

This design concept focused on reducing the outer diameter of the stator rather than shortening the stack length. Reducing the outer stator diameter will have the same effect it terms of increasing the reluctance of the flux path and hence a lower flux will flow. If this concept could considerably reduce the outer diameter of the stator, there would not only be benefits in terms of weight reduction in the motor but also in terms of packaging in the wheel assembly. The diameter however cannot be linearly scaled as the stack length could but rather it is the stator back which is to be linearly scaled. The number of stator turns was increased to 47 turns to solve the issues experienced with losses in concept 1. That meant that the slot area had to be increased compared to the CFS17 PMSM in order to maintain the fill factor which is a priority to ensure that the new motor does not become more difficulty to manufacture. The wire diameter was kept due to the significant copper losses experienced in concept 1 and reducing the wire diameter would increase the copper losses. That created problems with scaling the stator back since the change in slot area also will impact the stator back. Figure 40 shows the final 2D-model used in the simulations.

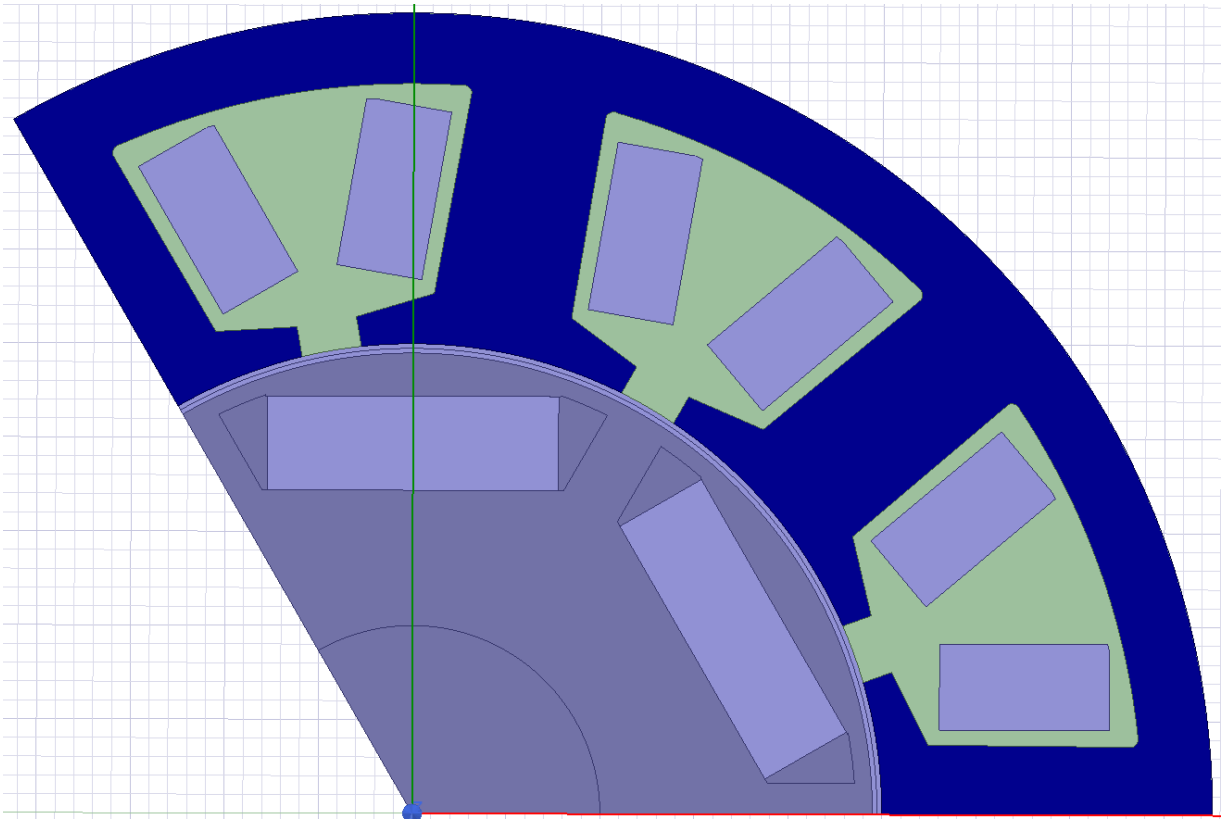

Figure 40: 2D-model of concept 2 with the reduced outer diameter and increased number of turns

After implementing the changes to the stator, the average maximum torque was lower than that of concept 1. In addition to that, the peak-to-peak torque ripple as seen in Figure 41 was increased to 9.3 Nm which is 50 % of the average maximum torque of the machine.

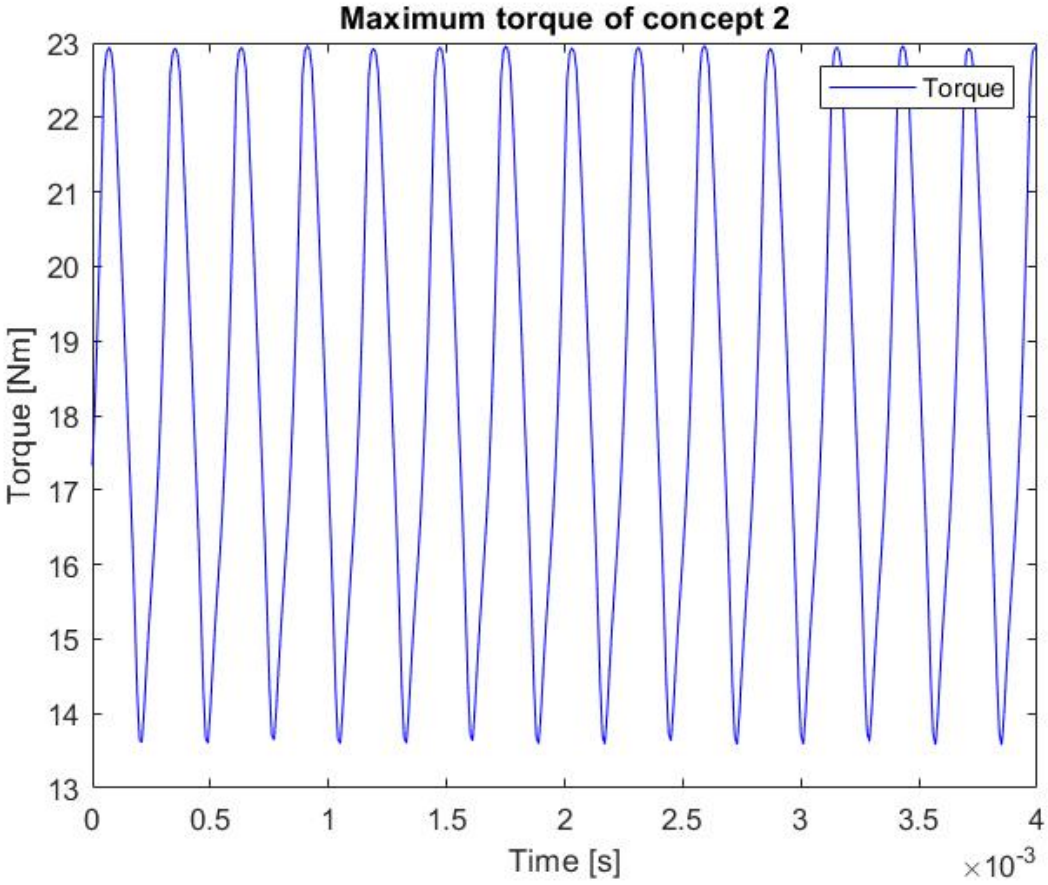

Figure 41: PMSM with reduced outer stator diameter operating at 11 900 RPM while being supplied with a phase current of 109 A RMS and a current angle of 90^o where it produces an average torque of 18.6 Nm

The phase voltage shown in Figure 42 did not reach the desired magnitude and the harmonic content was significant as can be seen in the FFT plot in Figure 43.

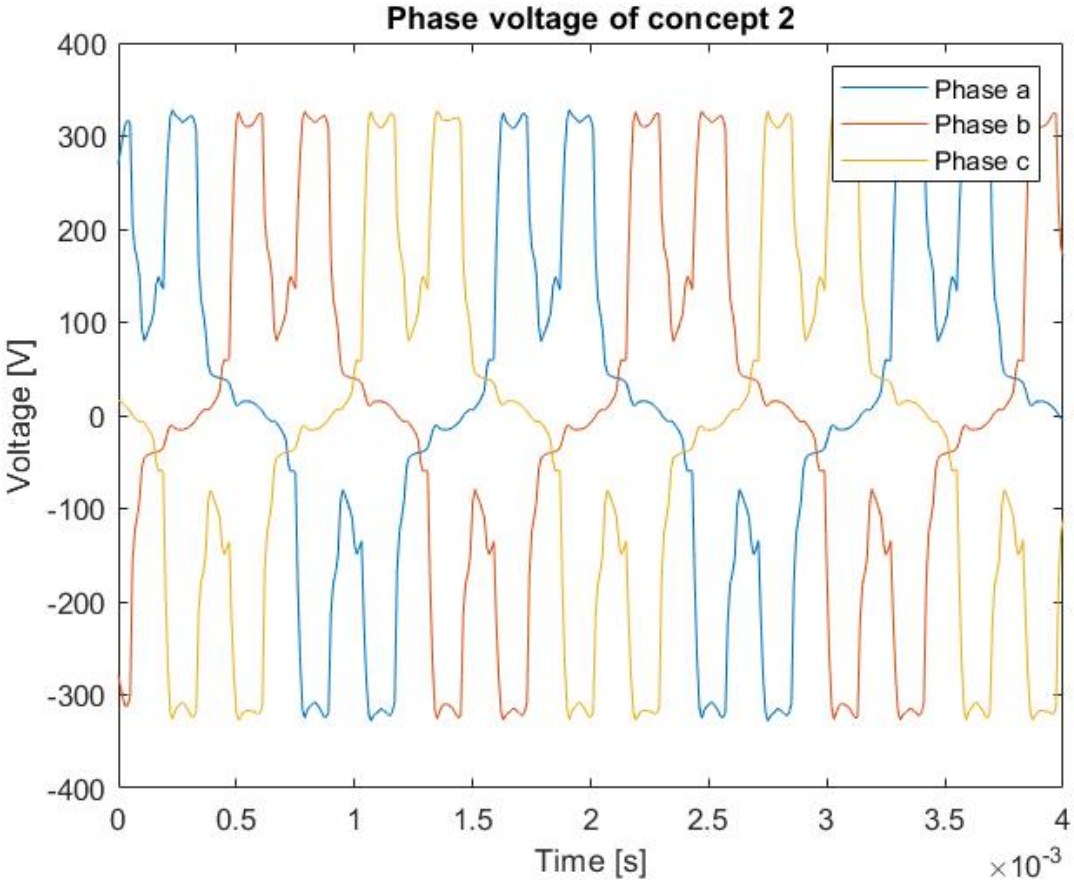

Figure 42: Phase voltage from the three phases of the PMSM with reduced outer stator diameter when operating at 11 900 rpm and 18.6 Nm

The fundamental part of the phase voltage reached a magnitude of 238 V with the 5:th harmonic reaching a magnitude of 101.3 V and the 7:th reached 57.62 V. Comparing those values to that of concept 1, it can be noted that the 5:th order harmonic is almost twice the magnitude for the second concept. That is also the case for the 7:th order harmonic.

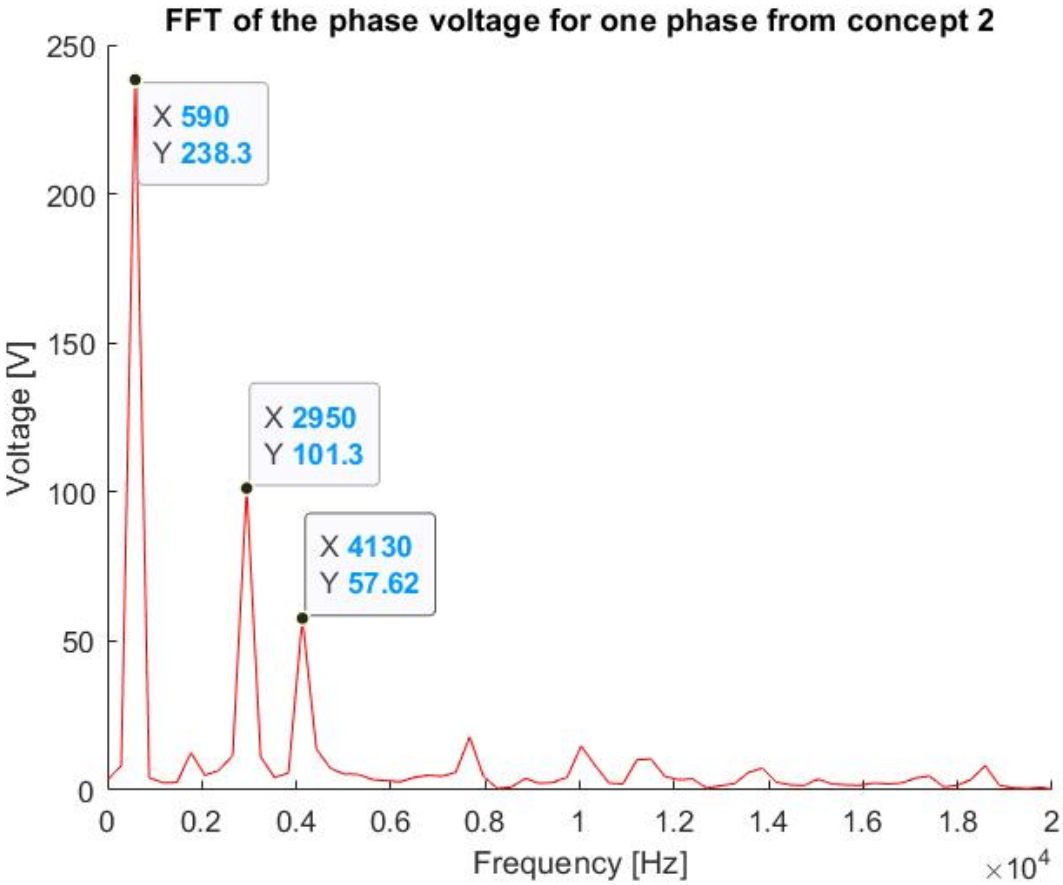

Figure 43: FFT of the phase voltage from one of the phases in Figure 42 coming from the PMSM with reduced outer stator diameter when operating at 11 900 rpm and 18.6 Nm

Since there were significant changes to the slot design there could be changes in the cogging torque. It can also be seen in Figure 44 that the peak-to-peak ripple is 550 mNm. That is a higher cogging torque than that of the original CFS17 motor.

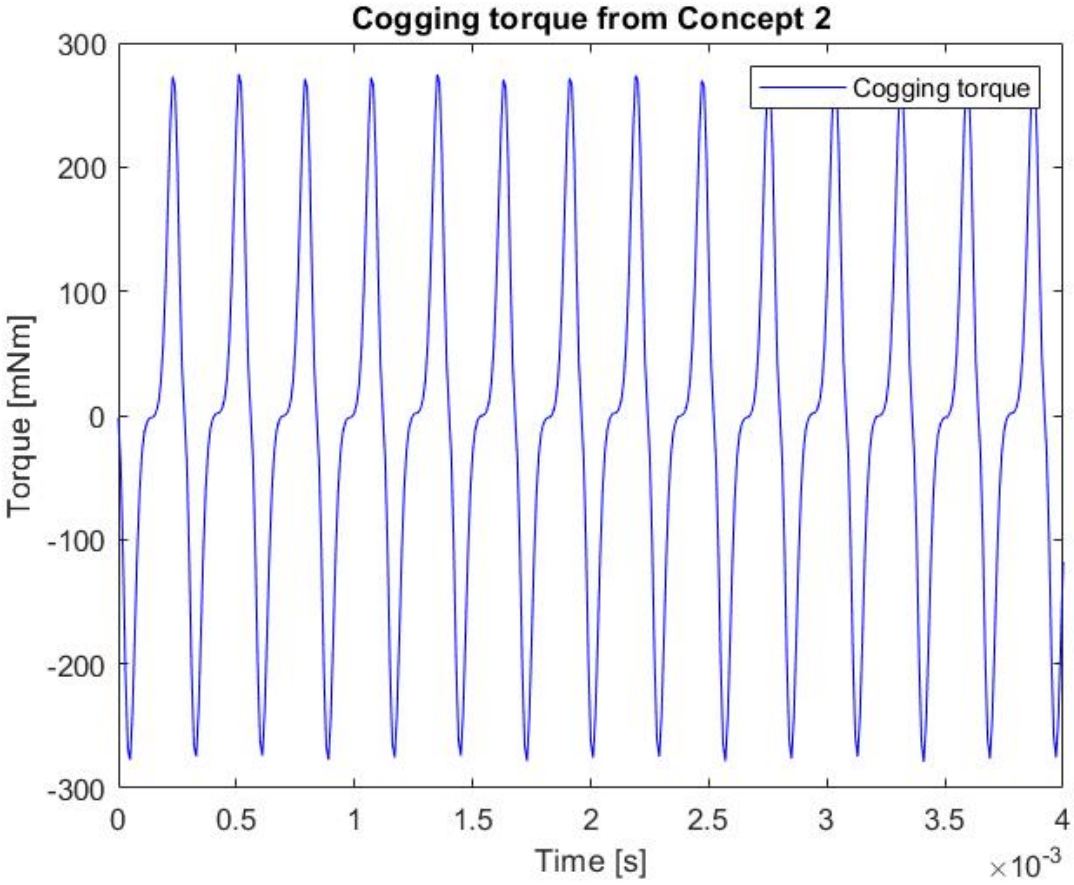

Figure 44: Cogging torque of the PMSM with the reduced outer stator diameter operating at 11 900 RPM where the supply current has been set to zero

7.4 Evaluation of concepts

The first parameter of comparison is the maximum torque of the machines where concept 1 is able to produce 20.3 Nm whilst concept 2 was only able to produce 18.6 Nm. The fundamental harmonic of the phase voltage reached in concept 1 was 317.3 V compared to 338 V in the second concept. The 5th and 7th order harmonics of concept 2 was however significantly larger than that of concept 1. Due to these severe phase voltage harmonics and time constraints, it was decided that the first concept would be further improved whilst the second concept would be scrapped.

7.4.1 Losses and proposed modifications to concept 1

With the decrease in stack length compared to the CFS17 motor, the overall flux in the machine will decrease as a result of a increased reluctance. This version required a higher current than the CFS17 motor to produce the same torque. The shorter stack will lead to a reduced wire length and hence the resistance will be lower. However with the current magnitude maintained, the copper losses will be higher at lower torques since the losses depend on the current squared. For comparing losses of the different concepts, one data point was selected at close to the rated operation point. These data points for the different motors are presented in the next chapter in Table 33 and 34. The reason that only one data point was selected for this concept was that this specific design is not of sufficient quality to move forward with without further modifications.

Due to a reduction in flux in the machine, the phase voltage will also decrease for the same current which means that the motor will enter field weakening at a higher speed. That means that the current will be unnecessarily high during all stages of operation and the copper losses across the entire speed range will be higher. One way of solving this problem is to add more coil turns in the stator which will increase the total flux in the motor and will lead to an increase of phase voltage.

7.5 Iteration 2, reduction in stack length with increased number of turns

The second version of the reduced stack length has a higher number of turns which would increase the phase voltage. The number of turns was increased from 41 turns per coil to 46 turns per coil. The number of turns selected was based on the how the phase voltage magnitudes had changed from Figure 34 and 38. Unfortunately the values was misread and therefore number selected turned out to be too low. Having increased the number of turns without decreasing the wire diameter, will force an increase of the slot area. The reason for not decreasing the wire diameter is for practical reasons where the old CFS17 motor uses 1.12 mm and CFS has several kg of that wire type in house. Also that would eliminate the risk of the wrong wire diameter being used when winding, especially if several different motor types would be manufactured in parallel. In a PMSM, the stator tooth is generally the location where the maximum flux density is achieved. That means that when increasing the slot area, reducing the width of the stator tooth should be avoided since that would cause higher iron losses in the machine. Instead, the slots were made larger by reducing the cross-section of the stator yoke since that would lead to a lower increase of iron losses.

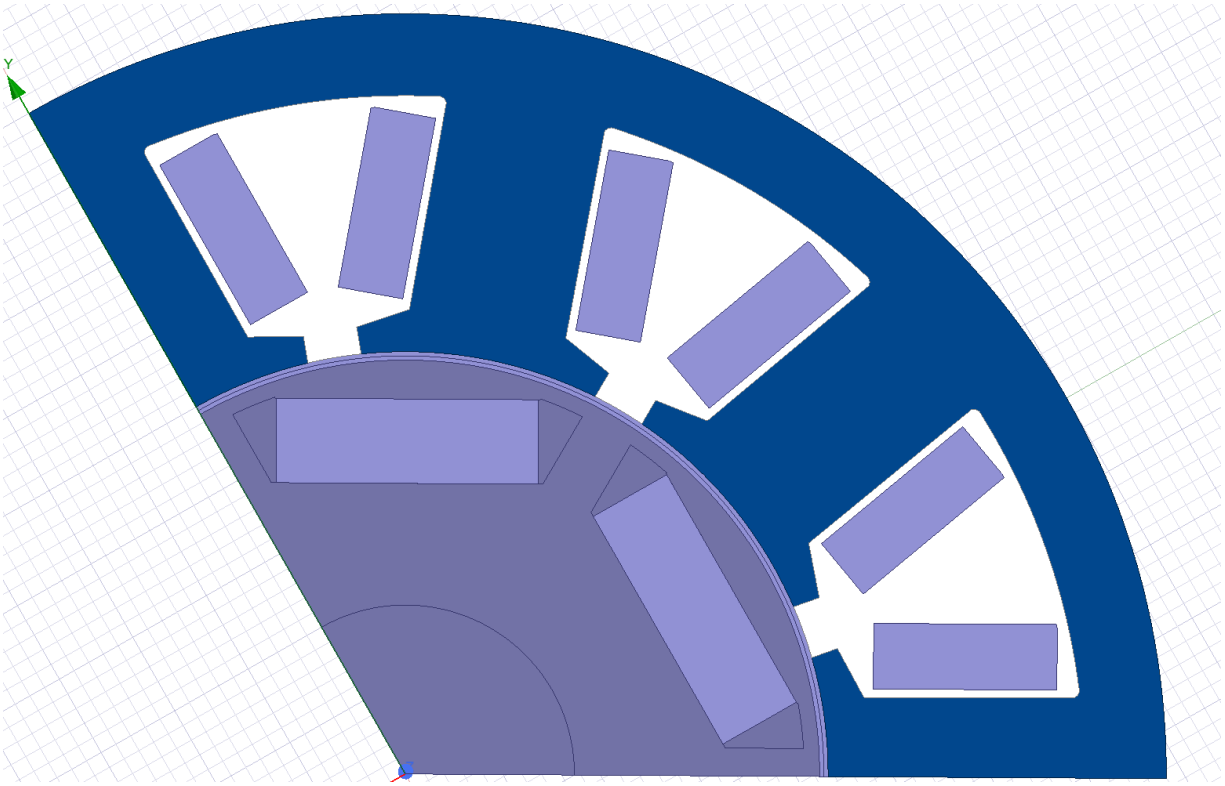

Figure 45: PMSM iteration 2 with a reduced stack length where the slot area has been increased as compared to Figure 23

After implementing this change, the maximum torque decreased as compared to iteration 1 as can be seen in Figure 46. The peak-to-peak ripple torque in this machine is approximately 40 % of the total torque produced as compared to that of the CFS17 motor and iteration 1 where it was only 30 %. One possible reason for this increase in stator core reluctance due to the higher required slot area which will lead to decrease in total flux of the machine.

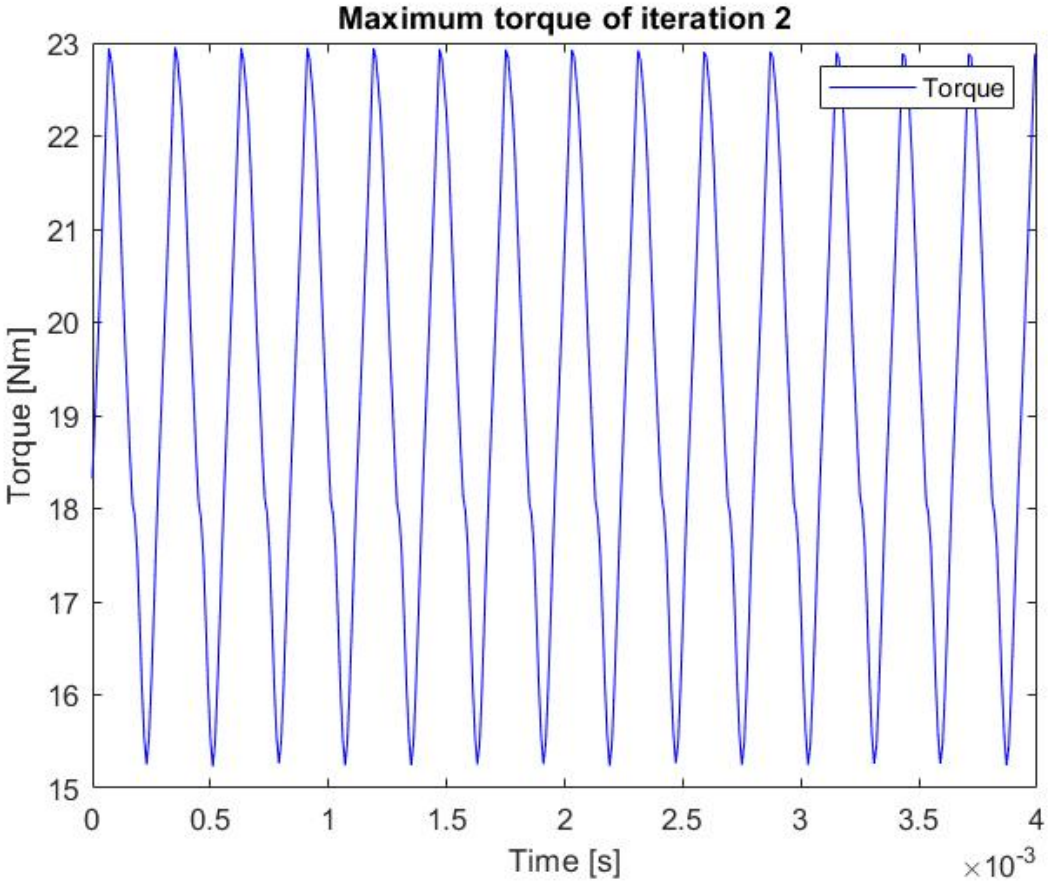

Figure 46: Iteration 2 of the PMSM with the reduced stack length operating at 11 900 RPM while being supplied with a phase current of 111 A RMS and a current angle of 90^o where it produces an average torque of 19.4 Nm

The phase voltage can be seen in Figure 47 where it can be seen that the waveforms has been significantly changed as compared to concept 1 and the CFS17 PMSM as can be seen in Figures 33 and 37.

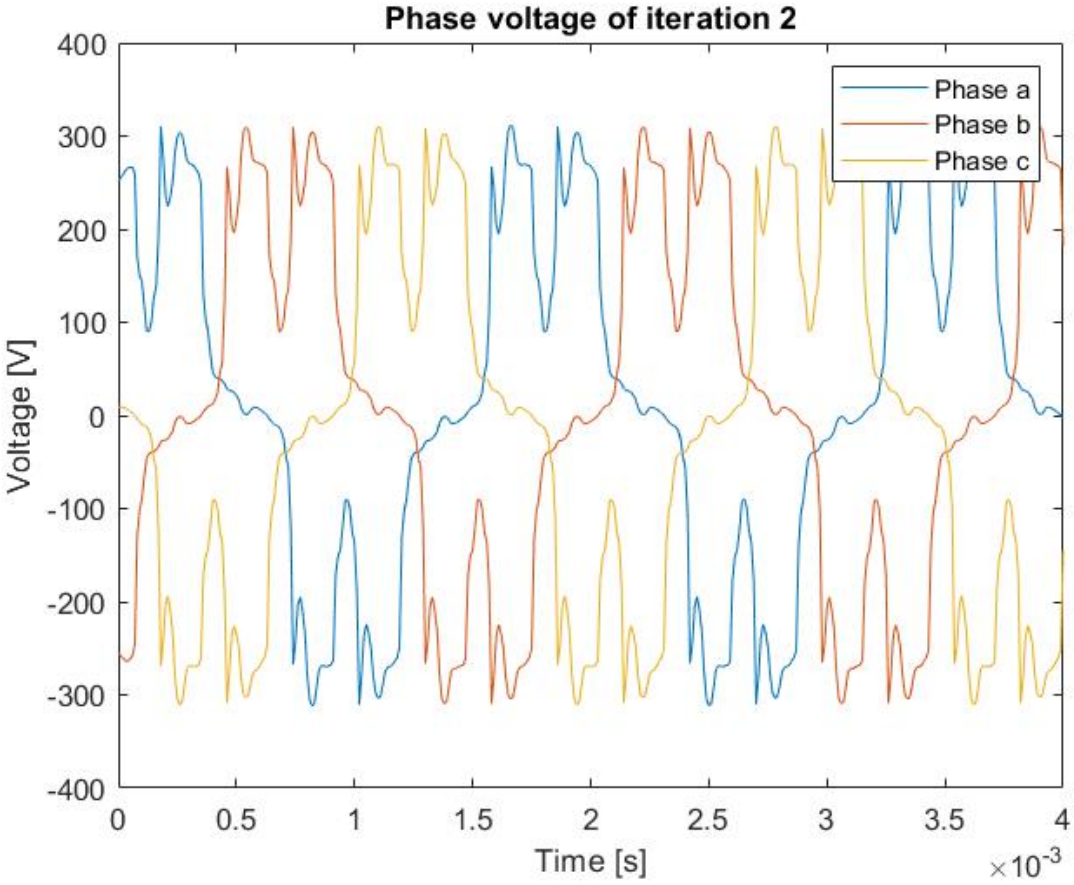

Figure 47: phase voltage from the three phases of iteration 2 of the PMSM with reduced stack length when operating at 11 900 rpm and 19.4 Nm

The FFT plot in Figure 48 also indicates large changes as compared to Figures 34 and 38. The fundamental is increased from concept 1 by 7.4 % to 240.6 V. That was not expected since the number of turns was increased by 12 %. This behaviour can be explained by the reduction in tooth width and stator back width which caused the reluctance of the fluxpath to increase as shown in (26). The 5:th harmonic was significantly increased and reached a magnitude of 84.53 V which is a 59 % increase from concept 1 and 33 % higher than the harmonic of the CFS17 motor. Also the 7:th order harmonic increases but that was only by 7 % to 28.91 V as compared to that of concept 1.

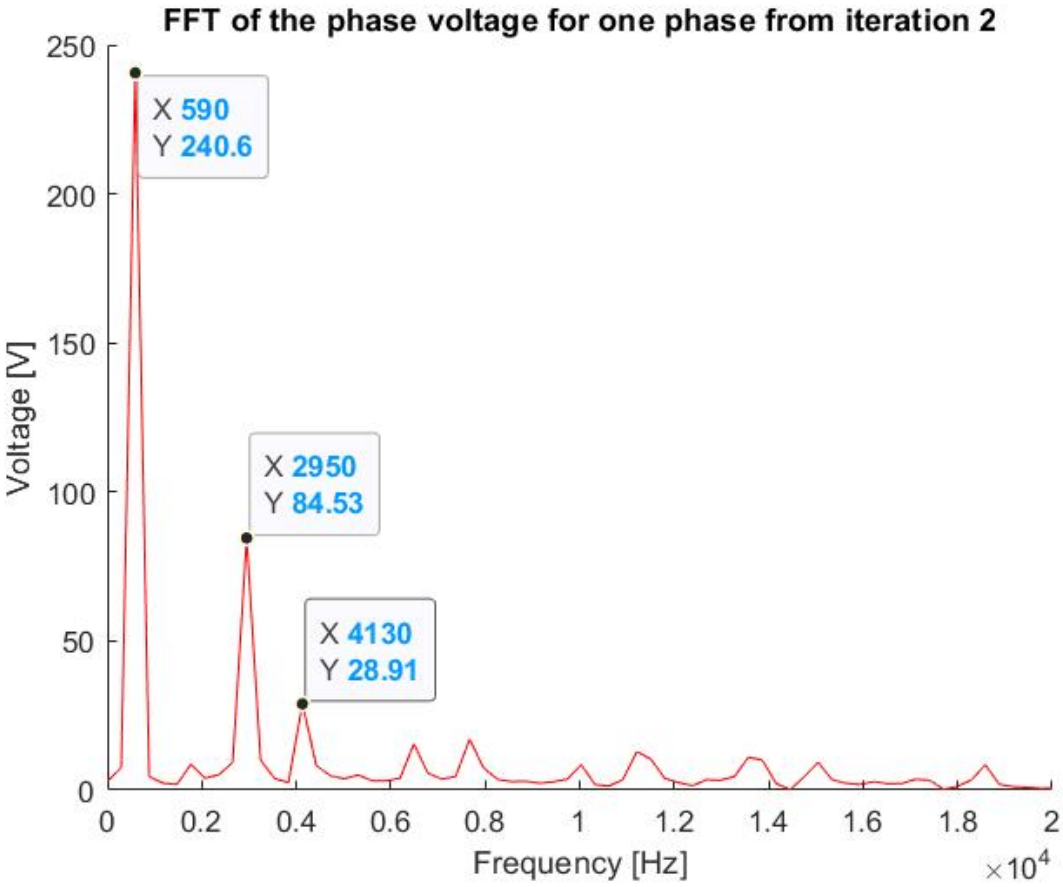

Figure 48: FFT of the phase voltage from one of the phases in Figure 47 coming from iteration 2 of the PMSM with reduced stack length when operating at 11 900 rpm and 19.4 Nm

Since there were changes required on more of the stator geometries, the cogging torque could be changed in an unexpected way. The peak-to-peak ripple as can be seen in Figure 49 is 472 mNm which is an increase of 0.4 % from concept 1. That is likely attributed to the small changes in slot geometries.

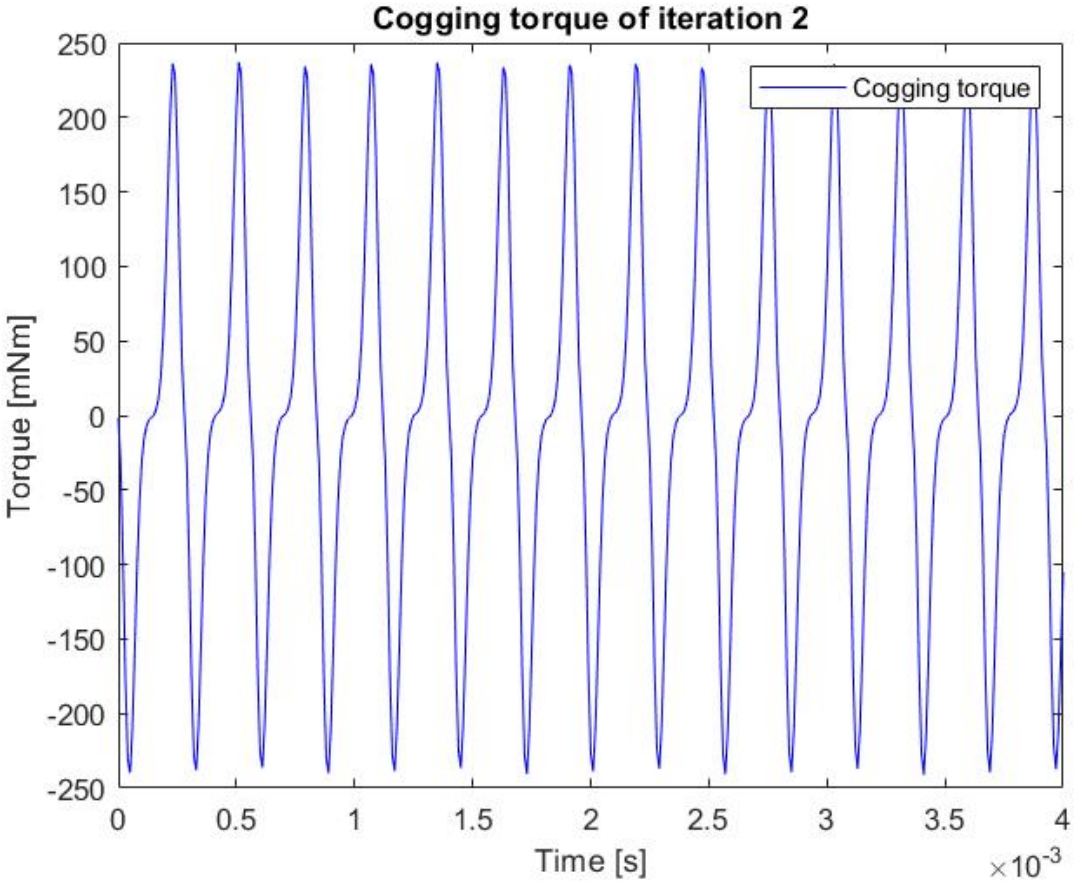

Figure 49: Cogging torque of iteration 2 of the PMSM with the reduced stack length operating at 11 900 RPM where the supply current has been set to zero

More simulations were conducted on this motor in order to in detail check the losses across the entire motor map and the results are shown in Section 7.5.1.

7.5.1 Losses

Table 23, 24, 25, 26 and 27 show the losses in the machine at different torques and speeds when providing the motor with an ideal sinusoidal current. What should be seen here is that the current required to obtain the same torque is higher for iteration 2 as compared to the CFS17 motor. Also the losses are generally higher for iteration 2. One interesting point which can be seen is that for 6 Nm, the iron losses are lower for iteration 2 as compared to the CFS17 motor for current angles of 35^o and 45^o. The rotor iron losses are however higher for iteration 2 which is not desirable due to the cooling issues of the rotor which are described in Section 4.7. The lowest current magnitude obtained is for torques up to 14 Nm is at 15^o which was not the case for the CFS17 motor where that angle had the lowest current magnitude up to 16 Nm.

Table 23: Speed sweep at 6 Nm for three current angles for PMSM iteration 2 with reduced stack length where the copper, stator iron and rotor iron losses were obtained

Speed	Current angle	Current magnitude	Copper losses	Iron losses	Rotor losses
5000	15^o	33.5 A	139.1 W	123.5 W	20 W
5000	35^o	34.6 A	150.2 W	103.8 W	18 W
5000	45^o	36.3 A	165.3 W	98.2 W	17 W
8000	15^o	33.5 A	139.1 W	268 W	43 W
8000	35^o	34.6 A	150.2 W	227.5 W	39 W
8000	45^o	36.3 A	165.3 W	217.5 W	38 W
11000	15^o	33.5 A	139.1 W	430 W	75 W
11000	35^o	34.6 A	150.2 W	375 W	68 W
11000	45^o	36.3 A	165.3 W	365 W	65 W
14000	15^o	33.5 A	139.1 W	628 W	116 W
14000	35^o	34.6 A	150.2 W	545 W	105 W
14000	45^o	36.3 A	165.3 W	535 W	100 W
16000	15^o	33.5 A	139.1 W	774 W	148 W
16000	35^o	34.6 A	150.2 W	678 W	134 W
16000	45^o	36.3 A	165.3 W	668 W	128 W
18000	15^o	33.5 A	139.1 W	964 W	184 W
18000	35^o	34.6 A	150.2 W	818 W	166 W
18000	45^o	36.3 A	165.3 W	802 W	159 W
20000	15^o	33.5 A	139.1 W	1140 W	223 W
20000	35^o	34.6 A	150.2 W	970 W	202 W
20000	45^o	36.3 A	165.3 W	956 W	193 W

Table 24: Speed sweep at 12 Nm for three current angles for PMSM iteration 2 with reduced stack length where the copper, stator iron and rotor iron losses were obtained

Speed	Current angle	Current magnitude	Copper losses	Iron losses	Rotor losses
5000	15^o	64 A	514 W	165 W	29 W
5000	35^o	65 A	530 W	145 W	23 W
5000	45^o	71.3 A	638 W	148 W	24 W
8000	15^o	64 A	514 W	365 W	63 W
8000	35^o	65 A	530 W	324 W	51 W
8000	45^o	71.3 A	638 W	339 W	54 W
11000	15^o	64 A	514 W	586 W	114 W
11000	35^o	65 A	530 W	533 W	87 W
11000	45^o	71.3 A	638 W	576 W	92 W
14000	15^o	64 A	514 W	865 W	177 W
14000	35^o	65 A	530 W	795 W	135 W
14000	45^o	71.3 A	638 W	859 W	142 W
16000	15^o	64 A	514 W	1067 W	226 W
16000	35^o	65 A	530 W	988 W	170 W
16000	45^o	71.3 A	638 W	1085 W	180 W
18000	15^o	64 A	514 W	1302 W	279 W
18000	35^o	65 A	530 W	1209 W	213 W
18000	45^o	71.3 A	638 W	1326 W	224 W
20000	15^o	64 A	514 W	1542 W	345 W
20000	35^o	65 A	530 W	1437 W	257 W
20000	45^o	71.3 A	638 W	1584 W	269 W

Table 25: Speed sweep at 14 Nm for three current angles for PMSM iteration 2 with reduced stack length where the copper, stator iron and rotor iron losses were obtained

Speed	Current angle	Current magnitude	Copper losses	Iron losses	Rotor losses
5000	15^o	76 A	725 W	176 W	30 W
5000	35^o	77 A	743.7 W	162 W	26 W
5000	45^o	83 A	865 W	167 W	28 W
8000	15^o	76 A	725 W	391 W	64 W
8000	35^o	77 A	743.7	361 W	57 W
8000	45^o	83 A	865 W	382 W	62 W
11000	15^o	76 A	725 W	633 W	115 W
11000	35^o	77 A	743.7	599 W	98 W
11000	45^o	83 A	865 W	652 W	105 W
14000	15^o	76 A	725 W	935 W	178 W
14000	35^o	77 A	743.7	894 W	151 W
14000	45^o	83 A	865 W	980 W	161 W
16000	15^o	76 A	725 W	1158 W	228 W
16000	35^o	77 A	743.7	1112 W	191 W
16000	45^o	83 A	865 W	1231 W	205 W
18000	15^o	76 A	725 W	1414 W	281 W
18000	35^o	77 A	743.7	1362 W	240 W
18000	45^o	83 A	865 W	1484 W	256 W
20000	15^o	76 A	725 W	1679 W	347 W
20000	35^o	77 A	743.7	1621 W	289 W
20000	45^o	83 A	865 W	1764 W	307 W

Table 26: Speed sweep at 16 Nm for three current angles for PMSM iteration 2 with reduced stack length where the copper, stator iron and rotor iron losses were obtained

Speed	Current angle	Current magnitude	Copper losses	Iron losses	Rotor losses
5000	15^o	90 A	1016 W	191.5 W	30 W
5000	35^o	88 A	971.4 W	182 W	29 W
5000	45^o	95.3 A	1139 W	191 W	31 W
8000	15^o	90 A	1016 W	424 W	66 W
8000	35^o	88 A	971.4 W	407 W	64 W
8000	45^o	95.3 A	1139 W	437 W	70 W
11000	15^o	90 A	1016 W	685 W	118 W
11000	35^o	88 A	971.4 W	676 W	109 W
11000	45^o	95.3 A	1139 W	749 W	119 W
14000	15^o	90 A	1016 W	1028 W	183 W
14000	35^o	88 A	971.4 W	1010 W	168 W
14000	45^o	95.3 A	1139 W	1120 W	184 W
16000	15^o	90 A	1016 W	1278 W	234 W
16000	35^o	88 A	971.4 W	1258 W	213 W
16000	45^o	95.3 A	1139 W	1415 W	233 W
18000	15^o	90 A	1016 W	1562 W	289 W
18000	35^o	88 A	971.4 W	1539 W	267 W
18000	45^o	95.3 A	1139 W	1730 W	192 W
20000	15^o	90 A	1016 W	1858 W	357 W
20000	35^o	88 A	971.4 W	1833 W	322 W
20000	45^o	95.3 A	1139 W	2068 W	350 W

Table 27: Speed sweep at 20 Nm for three current angles for PMSM iteration 2 with reduced stack length where the copper, stator iron and rotor iron losses were obtained

Speed	Current angle	Current magnitude	Copper losses	Iron losses	Rotor losses
5000	15^o	128 A	2055 W	244.8 W	33 W
5000	35^o	111.3 A	1554 W	223 W	32 W
5000	45^o	121.5 A	1851 W	255 W	39 W
8000	15^o	128 A	2055 W	546 W	72 W
8000	35^o	111.3 A	1554 W	499 W	71 W
8000	45^o	121.5 A	1851 W	581 W	90 W
11000	15^o	128 A	2055 W	912 W	128 W
11000	35^o	111.3 A	1554 W	835 W	121 W
11000	45^o	121.5 A	1851 W	1001 W	151 W
14000	15^o	128 A	2055 W	1360 W	197 W
14000	35^o	111.3 A	1554 W	1250 W	188 W
14000	45^o	121.5 A	1851 W	1498 W	234 W
16000	15^o	128 A	2055 W	1693 W	252 W
16000	35^o	111.3 A	1554 W	1564 W	238 W
16000	45^o	121.5 A	1851 W	1888 W	296 W
18000	15^o	128 A	2055 W	2066 W	311 W
18000	35^o	111.3 A	1554 W	1918 W	298 W
18000	45^o	121.5 A	1851 W	2312 W	373 W
20000	15^o	128 A	2055 W	2455 W	383 W
20000	35^o	111.3 A	1554 W	2288 W	361 W
20000	45^o	121.5 A	1851 W	2767 W	447 W

7.5.2 Proposed modifications to iteration 2

This version proved to have higher iron losses in the stator and the rotor compared to the previous version, but it also had significantly lower copper losses. When comparing it to the old motor, it should be noted that the iron losses are overall similar, but the rotor losses are significantly higher in this version. The reason for this could be because of the flux paths in the rotor. The flux from the magnets and the flux from the coils will not have the same flux path in the rotor. The flux from the magnets will flow into and out from the cross-section of the magnet poles whilst the flux from the coils will flow in between the rotor ribs which will have a higher flux density than the previous motor. Since there is now a higher reluctance in the flux path, the magnet flux will decrease since the MMF from the magnets are unchanged. That means that a larger portion of the total flux must be produced by the coils which means that a higher current is needed. That will increase the copper losses and it will also increase the amount of flux that will flow in the rotor ribs. The increase in flux through those ribs caused the increase in rotor losses. That problem could be solved by increasing the magnet thickness which was done in the next version of the motor.

7.6 Iteration 3, reduction in stack length with increased number of turns and increased magnet thickness

The third iteration of the reduced stack length was a late change in the project. The magnet thickness marked in Figure 50 was changed to the maximum thickness that the current ribs would allow spacing for. The ribs are important for the structural strength of the rotor and can therefore not be reduced that much. The increase in magnet volume did not exceed the volume of the old magnets and hence it would not increase the cost of magnets. There are two possible problems with this design. The first is that larger cut-outs in the rotor are required which could cause problems with structural integrity of the rotor. The second problem is that there is less space in the rotor cut-outs for mounting the magnets and that is because the new magnet thickness prevents any extension of the flux barrier cut-outs.

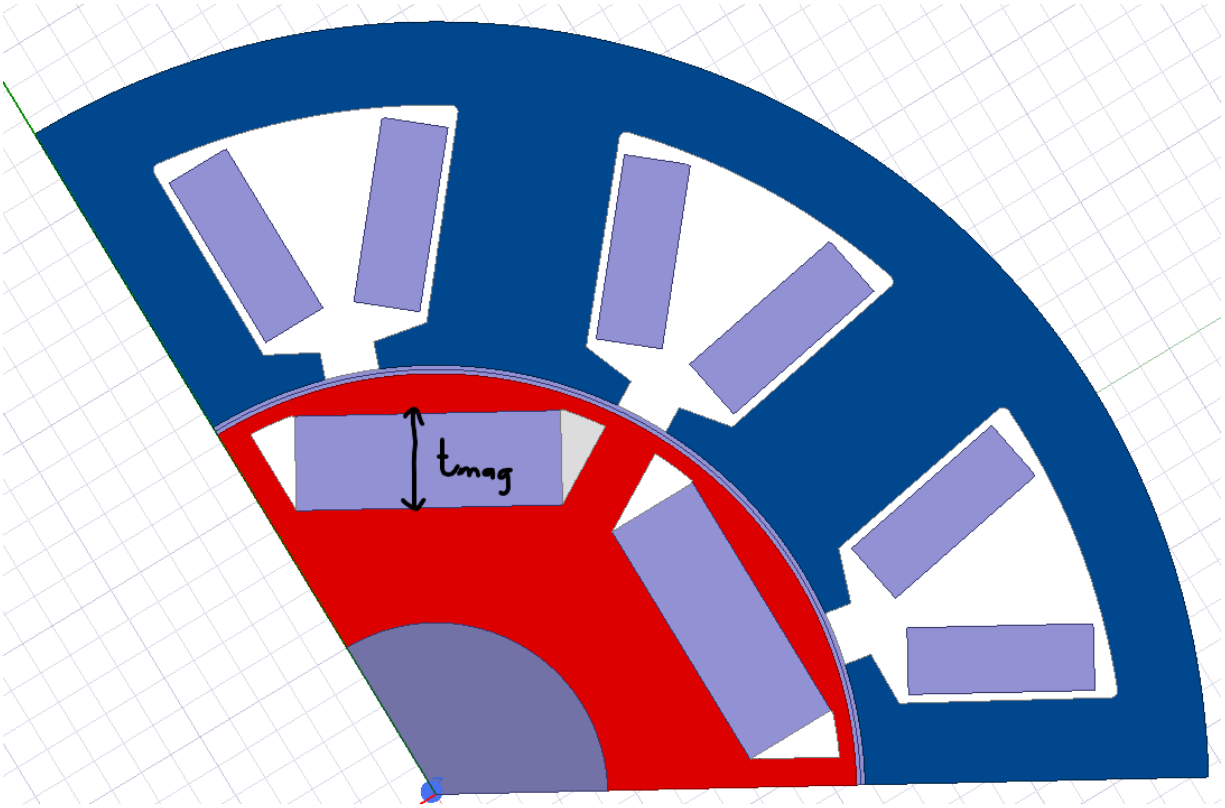

Figure 50: 2D-model of iteration 3 with the shortened stack length, increased number of turns and increased magnet thickness

This increase in magnet thickness did lead to an increase in overall torque which is attributed to the increase in overall MMF in the motor. In Figure 51, it can be seen that the torque is increased from 19.4 Nm to 19.7 Nm which is an increase of 1.5 %. Those 1.5 % was not proportional to the increase in magnet thickness and the reason for that is that for the maximum torque, the motor is operating at higher flux densities and hence the material will be more saturated. That can be seen in Figure 18. The peak-to-peak ripple for this motor was 7.9 Nm which is about 40 % of the average torque that the motor produces. That is approximately the same as for the second iteration but more than the concept design where it was about 30 % of the average torque.

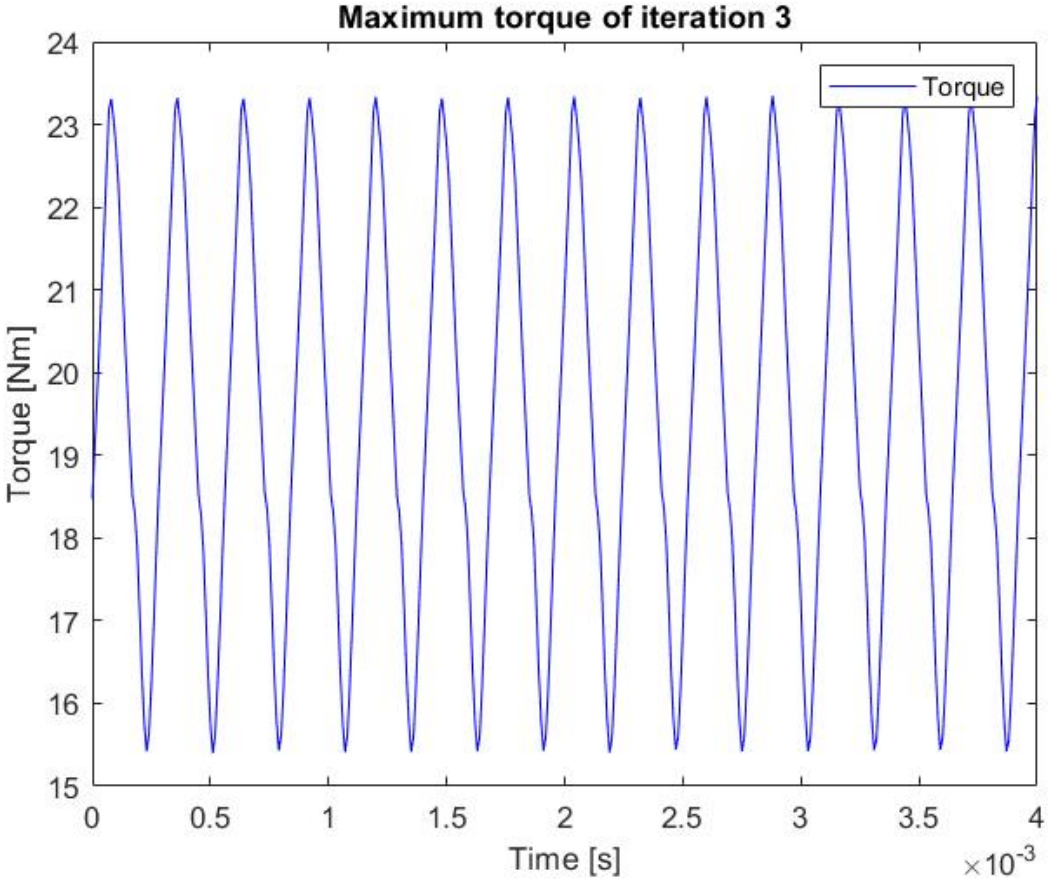

Figure 51: Iteration 3 of the PMSM with the reduced stack length operating at 11 900 RPM while being supplied with a phase current of 111 A RMS and a current angle of 90^o where it produces an average torque of 19.7 Nm

However, the phase voltage was still not of the same magnitude as the CFS17 motor as could be seen in Figure 53 and the significant magnitudes of the 5:th and 7:th harmonic was also still present as can be seen in Figure 52 and 53.

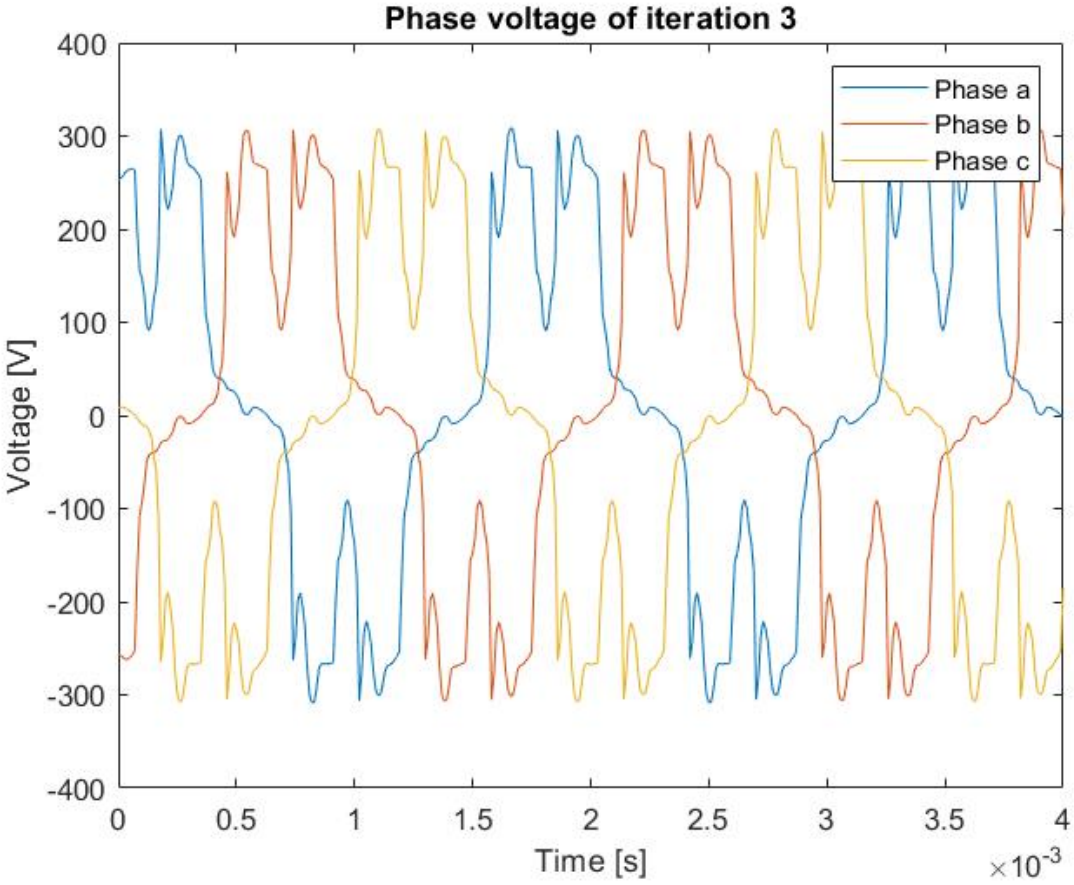

Figure 52: Phase voltage from the three phases of iteration 3 of the PMSM with reduced stack length when operating at 11 900 rpm and 19.7 Nm

The fundamental component of the voltage was unchanged and remained at 240.5 V and the 5:th and 7:th harmonics was decreased by about 2 V compared to iteration 2.

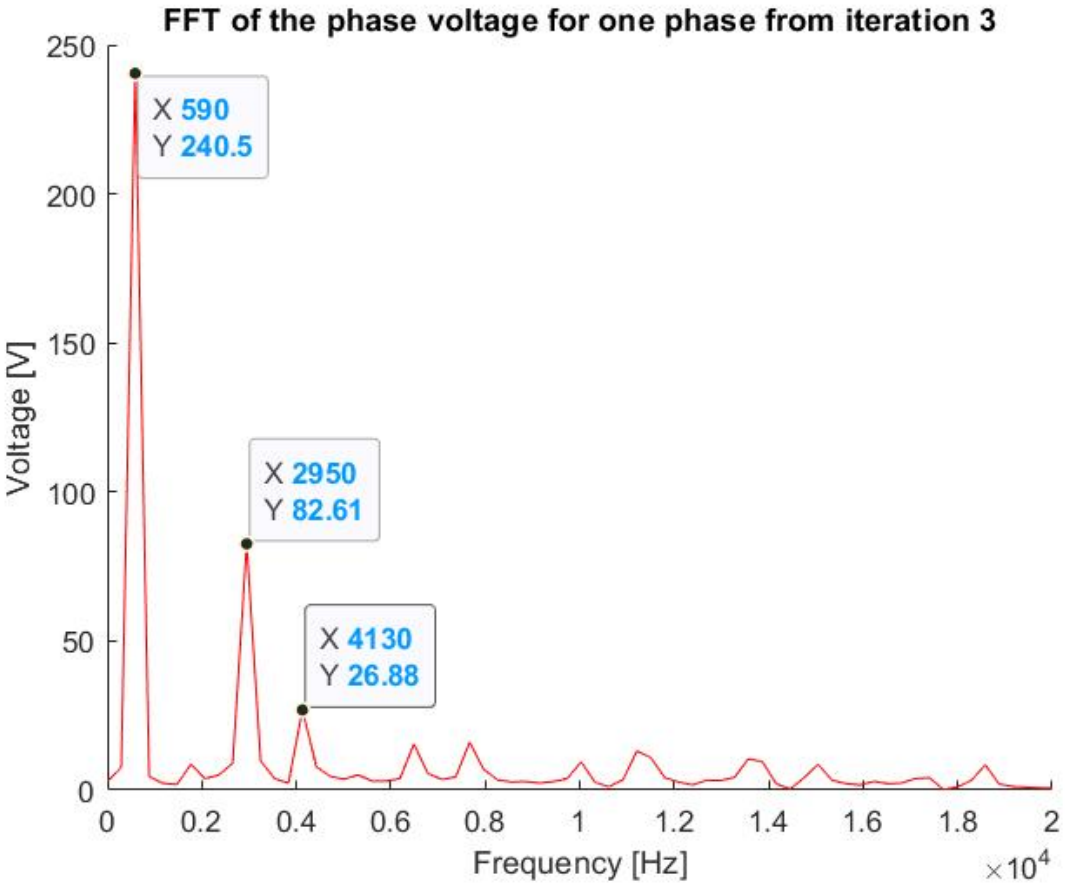

Figure 53: FFT of the phase voltage from one of the phases in Figure 52 coming from iteration 3 of the PMSM with reduced stack length when operating at 11 900 rpm and 19.7 Nm

The cogging torque peak-to-peak ripple did increase to 481.8 mNm compared to the 472 mNm of iteration 2 which can probably be attributed to the larger magnets where the attraction forces between the stator and rotor has increased.

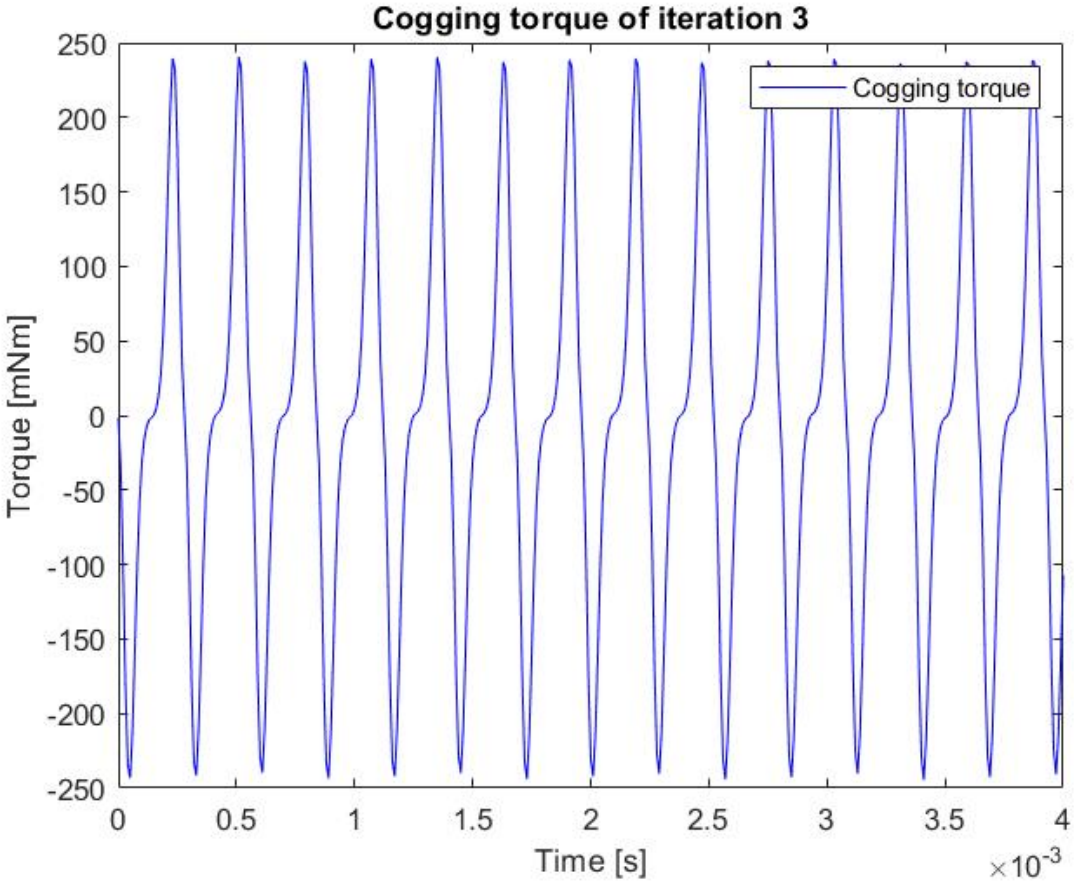

Figure 54: Cogging torque of iteration 3 of the PMSM with the reduced stack length operating at 11 900 RPM where the supply current has been set to zero

7.6.1 Proposed changes to iteration 3

Due to the remaining phase voltage issues, a final iteration of this motor was required. Since it was concluded early that a fourth version of the would be needed, no data for the efficiency maps was obtained. The reason for that is that the time restrictions would not allow for it. After studying the flux densities in different parts of the stator, it could be concluded that the flux density in the stator yoke was much higher than what was expected. That means that there is a much higher risk of having small local saturations which could contribute to higher levels of harmonics in the phase voltage.

7.7 Iteration 4, reduced stack length with increased number of turns, increased magnet thickness and altered stator back/tooth width ratio

In the final version of the shortened stack shown in Figure 55, the number of coil turns was again increased to 50 turns in order to obtain the correct phase voltage magnitude. Also, it was attempted to find the optimal relationship between the width of the stator tooth and the width of the stator yoke. The changes implemented forced a slight increase in the stack length in order for the motor to still be able to produce the same torque output.

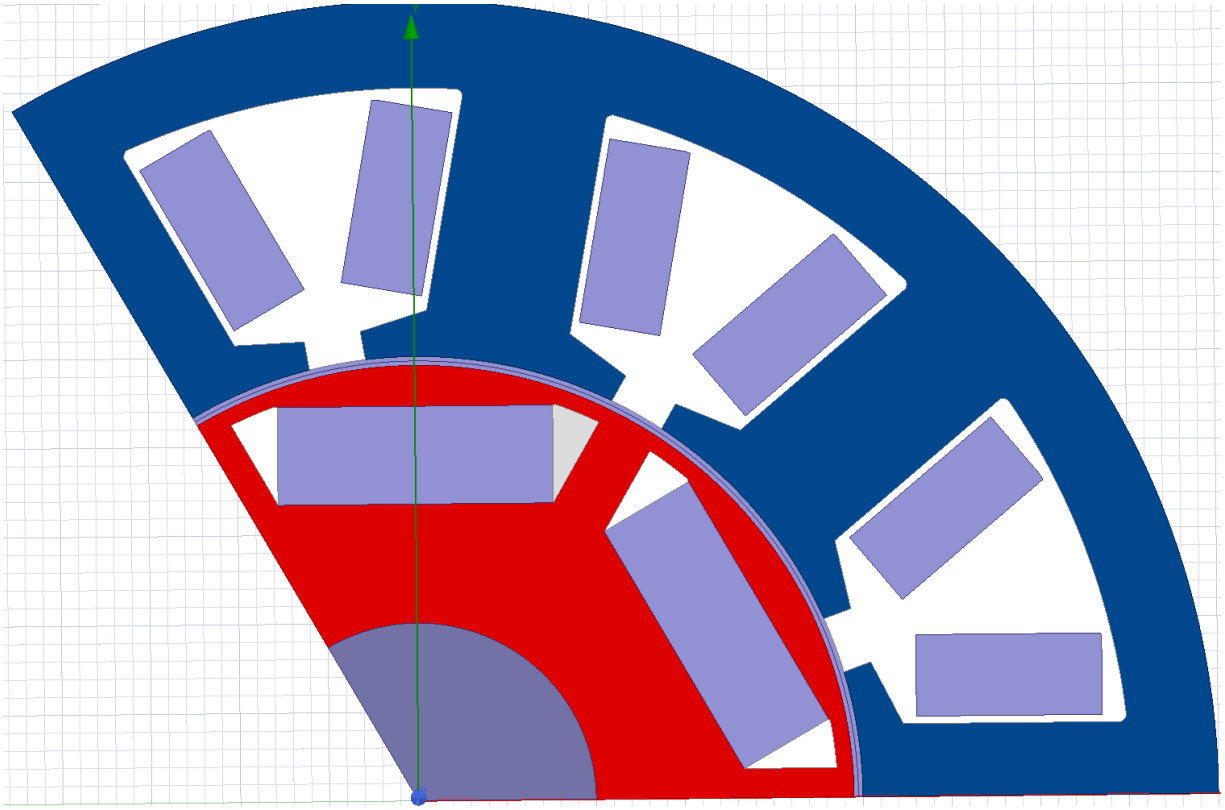

Figure 55: Final version with the shortened stack length

The maximum average torque produced by the motor remained unchanged with the implementation of these changes. However the peak-to-peak torque ripple changed where it was now 35.5 % of the average torque which was a 5 % decrease from iteration 3 as can be seen in Figure 56. It is however still more than that of the CFS17 motor.

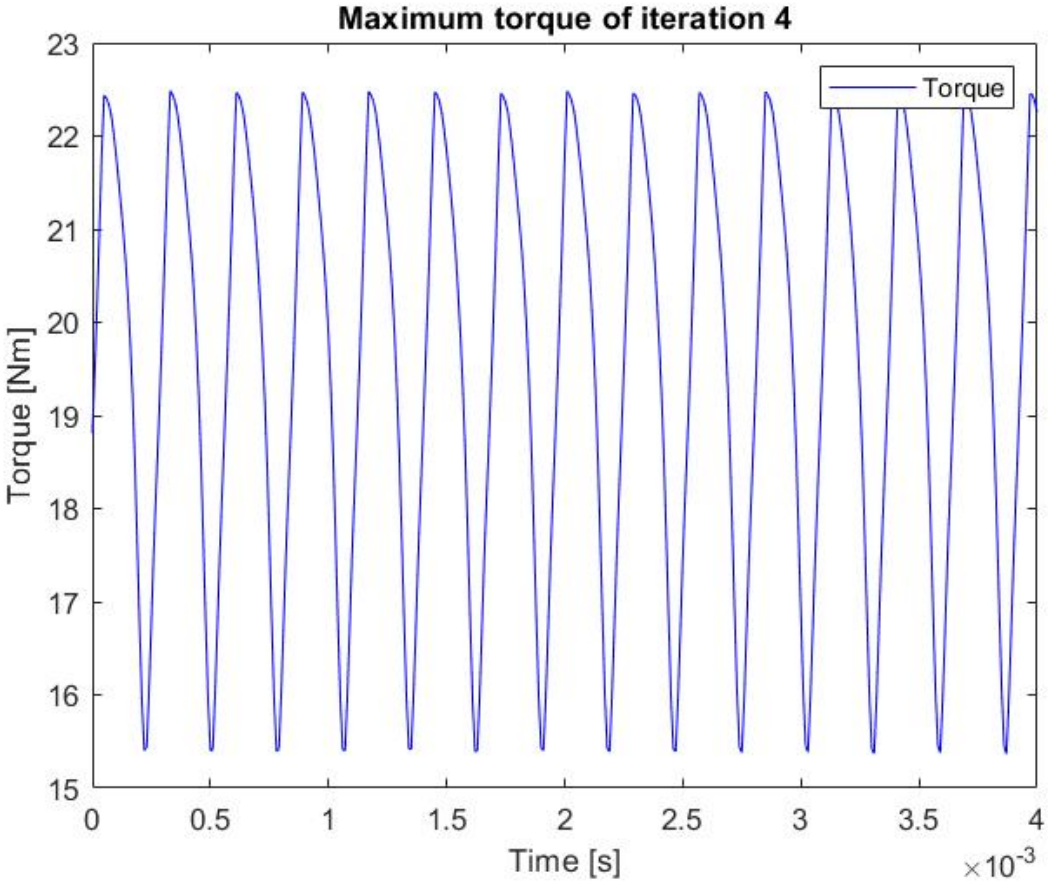

Figure 56: Iteration 4 of the PMSM with the reduced stack length operating at 11 900 RPM while being supplied with a phase current of 111 A RMS and a current angle of 90^o where it produces an average torque of 19.7 Nm

The changes made, had significant impact on the phase voltage waveform as can be seen in Figure 57. The FFT of the voltage indicated that the 5:th order harmonic was reduced to 70.12 V as can be seen in Figure 58 compared to iteration 3. That is however 11.3 % higher than that of the CFS17 motor. Also the fundamental increased to 262.6 V which is very close to that of the CFS17 motor which was one of the main goals with this iteration.

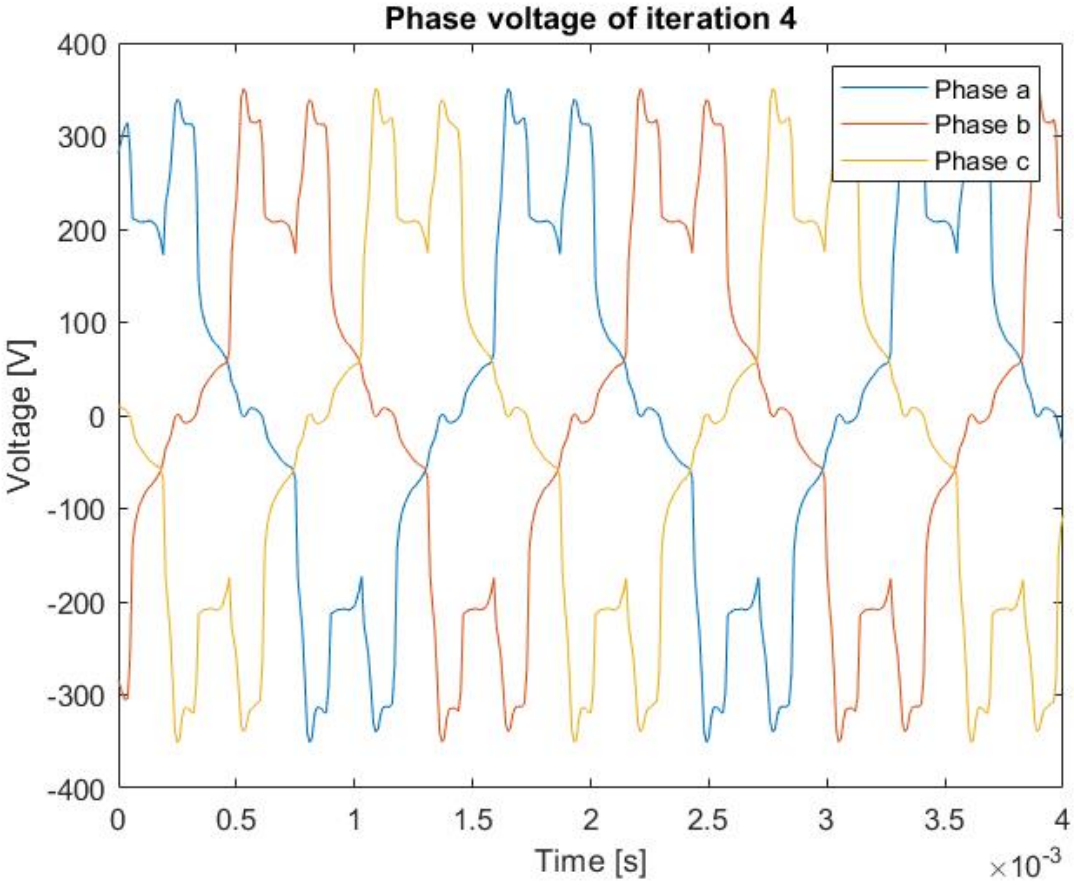

Figure 57: Phase voltage from the three phases of iteration 4 of the PMSM with reduced stack length when operating at 11 900 rpm and 19.7 Nm

The FFT plot did however also indicate that the 7:th order harmonic increased to 42.75 V which is 34 % higher than the CFS17 motor.

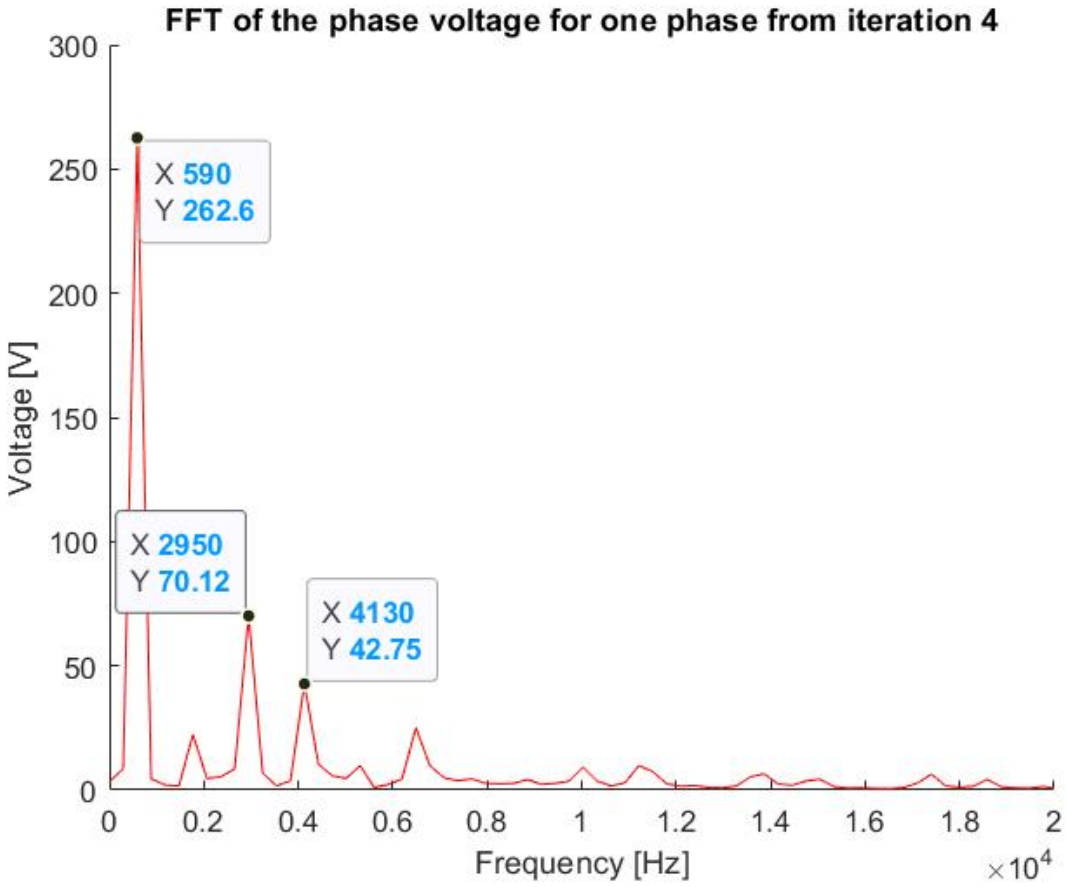

Figure 58: FFT of the phase voltage from one of the phases in Figure 57 coming from iteration 4 of the PMSM with reduced stack length when operating at 11 900 rpm and 19.7 Nm

The cogging torque peak-to-peak ripple of iteration 4 increased to 520 mNm which can probably be attributed to the change in geometries in the slot.

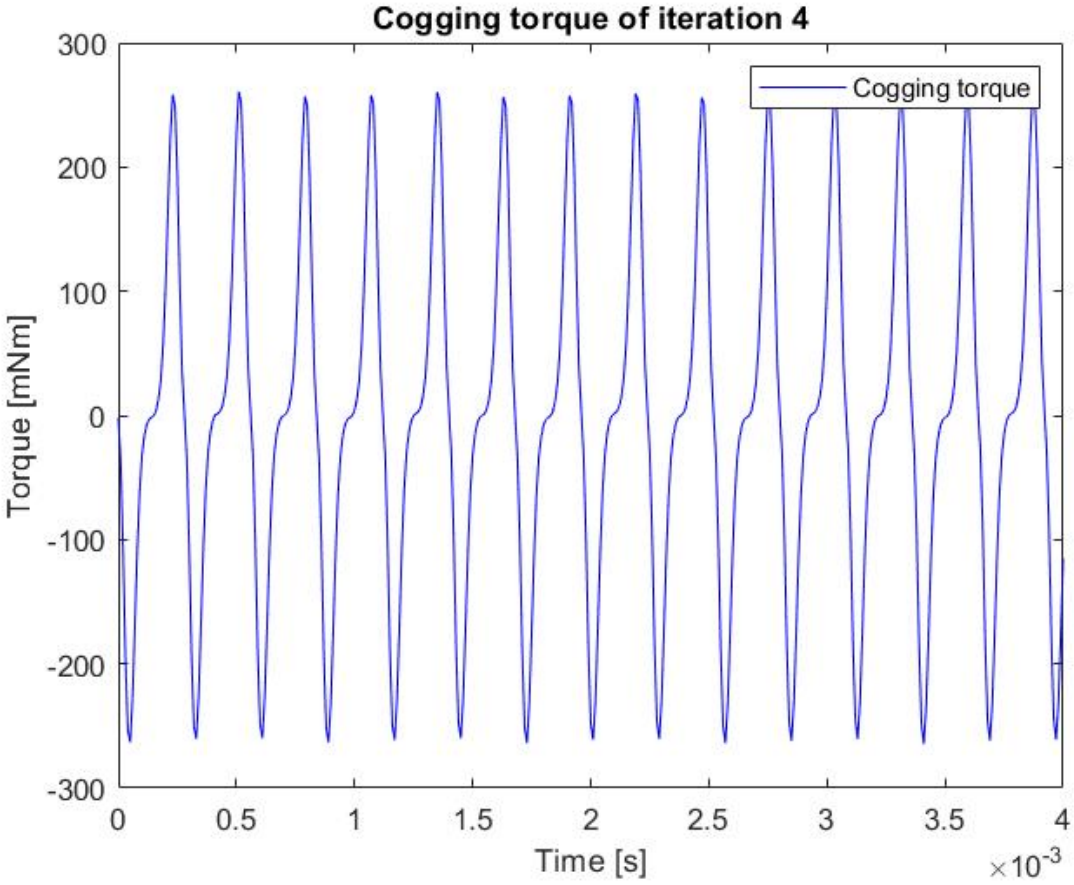

Figure 59: Cogging torque of iteration 4 of the PMSM with the reduced stack length operating at 11 900 RPM where the supply current has been set to zero

7.7.1 Losses

For this motor, a full sweep of the operation points was performed which would be used to obtain the efficiency maps. The data is presented in Tables 28, 29, 30, 31, 32. It can be noted that the current magnitudes for lower torques are lower than the currents in the CFS17 PMSM. The rotor losses and iron losses are slightly higher and that might be attributable to the higher flux densities in the machine. It should however be said that the loss magnitudes are very similar in the stator and rotor.

Table 28: Speed sweep at 6 Nm for three current angles for PMSM iteration 4 with reduced stack length where the copper, stator iron and rotor iron losses were obtained

Speed	Current angle	Current magnitude	Copper losses	Iron losses	Rotor losses
5000	15^o	27.7 A	117 W	128 W	18 W
5000	35^o	29 A	128 W	109 W	16 W
5000	45^o	32 A	156 W	105 W	16 W
8000	15^o	27.7 A	117 W	277 W	40 W
8000	35^o	29 A	128 W	237 W	36 W
8000	45^o	32 A	156 W	231 W	36 W
11000	15^o	27.7 A	117 W	441 W	70 W
11000	35^o	29 A	128 W	385 W	63 W
11000	45^o	32 A	156 W	384 W	61 W
14000	15^o	27.7 A	117 W	640 W	108 W
14000	35^o	29 A	128 W	557 W	96 W
14000	45^o	32 A	156 W	558 W	94 W
16000	15^o	27.7 A	117 W	787 W	137 W
16000	35^o	29 A	128 W	690 W	123 W
16000	45^o	32 A	156 W	694 W	120 W
18000	15^o	27.7 A A	117 W	955 W	171 W
18000	35^o	29 A	128 W	830 W	153 W
18000	45^o	32 A	156 W	833 W	150 W
20000	15^o	27.7 A	117 W	1127 W	208 W
20000	35^o	29 A	128 W	983 W	185 W
20000	45^o	32 A	156 W	990 W	181 W

Table 29: Speed sweep at 12 Nm for three current angles for PMSM iteration 4 with reduced stack length where the copper, stator iron and rotor iron losses were obtained

Speed	Current angle	Current magnitude	Copper losses	Iron losses	Rotor losses
5000	15^o	57 A	494 W	160 W	24 W
5000	35^o	56 A	477 W	150 W	21 W
5000	45^o	61 A	566 W	150 W	22 W
8000	15^o	57 A	494 W	354 W	53 W
8000	35^o	56 A	477 W	336 W	47 W
8000	45^o	61 A	566 W	344 W	48 W
11000	15^o	57 A	494 W	570 W	94 W
11000	35^o	56 A	477 W	548 W	80 W
11000	45^o	61 A	566 W	578 W	48 W
14000	15^o	57 A	494 W	836 W	146 W
14000	35^o	56 A	477 W	812 W	123 W
14000	45^o	61 A	566 W	856 W	126 W
16000	15^o	57 A	494 W	1036 W	185 W
16000	35^o	56 A	477 W	1006 W	156 W
16000	45^o	61 A	566 W	1080 W	160 W
18000	15^o	57 A	494 W	1264 W	231 W
18000	35^o	56 A	477 W	1231 W	195 W
18000	45^o	61 A	566 W	1321 W	199 W
20000	15^o	57 A	494 W	1497 W	284 W
20000	35^o	56 A	477 W	1460 W	135 W
20000	45^o	61 A	566 W	1574 W	239 W

Table 30: Speed sweep at 14 Nm for three current angles for PMSM iteration 4 with reduced stack length where the copper, stator iron and rotor iron losses were obtained

Speed	Current angle	Current magnitude	Copper losses	Iron losses	Rotor losses
5000	15^o	69 A	724 W	171 W	25 W
5000	35^o	66 A	662 W	164 W	23 W
5000	45^o	70.5 A	756 W	165 W	24 W
8000	15^o	69 A	724 W	381 W	55 W
8000	35^o	66 A	662 W	367 W	52 W
8000	45^o	70.5 A	756 W	378 W	54 W
11000	15^o	69 A	724 W	618 W	97 W
11000	35^o	66 A	662 W	601 W	88 W
11000	45^o	70.5 A	756 W	639 W	92 W
14000	15^o	69 A	724 W	906 W	152 W
14000	35^o	66 A	662 W	892 W	136 W
14000	45^o	70.5 A	756 W	950 W	141 W
16000	15^o	69 A	724 W	1126 W	193 W
16000	35^o	66 A	662 W	1107 W	173 W
16000	45^o	70.5 A	756 W	1198 W	179 W
18000	15^o	69 A	724 W	1370 W	240 W
18000	35^o	66 A	662 W	1357 W	216 W
18000	45^o	70.5 A	756 W	1466 W	223 W
20000	15^o	69 A	724 W	1624 W	296 W
20000	35^o	66 A	662 W	1610 W	296 W
20000	45^o	70.5 A	756 W	1747 W	268 W

Table 31: Speed sweep at 16 Nm for three current angles for PMSM iteration 4 with reduced stack length where the copper, stator iron and rotor iron losses were obtained

Speed	Current angle	Current magnitude	Copper losses	Iron losses	Rotor losses
5000	15^o	83 A	1047 W	189 W	27 W
5000	35^o	75 A	855 W	178 W	25 W
5000	45^o	82.5 A	1035 W	189 W	28 W
8000	15^o	83 A	1047 W	420 W	58 W
8000	35^o	75 A	855 W	398 W	56 W
8000	45^o	82.5 A	1047 W	431 W	62 W
11000	15^o	83 A	1035 W	688 W	102 W
11000	35^o	75 A	855 W	654 W	95 W
11000	45^o	82.5 A	1035 W	732 W	106 W
14000	15^o	83 A	1047 W	1007 W	159 W
14000	35^o	75 A	855 W	972 W	147 W
14000	45^o	82.5 A	1035 W	1090 W	162 W
16000	15^o	83 A	1047 W	1257 W	202 W
16000	35^o	75 A	855 W	1208 W	186 W
16000	45^o	82.5 A	1035 W	1373 W	206 W
18000	15^o	83 A	1047 W	1526 W	251 W
18000	35^o	75 A	855 W	1481 W	233 W
18000	45^o	82.5 A	1035 W	1679 W	258 W
20000	15^o	83 A	1047 W	1808 W	309 W
20000	35^o	75 A	855 W	1758 W	281 W
20000	45^o	82.5 A	1035 W	2003 W	309 W

Table 32: Speed sweep at 20 Nm for three current angles for PMSM iteration 4 with reduced stack length where the copper, stator iron and rotor iron losses were obtained

Speed	Current angle	Current magnitude	Copper losses	Iron losses	Rotor losses
5000	15^o	115 A	2011 W	235 W	29 W
5000	35^o	100 A	1520 W	221 W	29 W
5000	45^o	103.5 A	1629 W	236 W	33 W
8000	15^o	115 A	2011 W	523 W	65 W
8000	35^o	100 A	1520 W	492 W	65 W
8000	45^o	103.5 A	1629 W	536 W	74 W
11000	15^o	115 A	2011 W	875 W	112 W
11000	35^o	100 A	1520 W	820 W	111 W
11000	45^o	103.5 A	1629 W	917 W	125 W
14000	15^o	115 A	2011 W	1284 W	175 W
14000	35^o	100 A	1520 W	1230 W	175 W
14000	45^o	103.5 A	1629 W	1370 W	193 W
16000	15^o	115 A	2011 W	1605 W	222 W
16000	35^o	100 A	1520 W	1532 W	217 W
16000	45^o	103.5 A	1629 W	1726 W	243 W
18000	15^o	115 A	2011 W	1942 W	277 W
18000	35^o	100 A	1520 W	1880 W	272 W
18000	45^o	103.5 A	1629 W	2112 W	305 W
20000	15^o	115 A	2011 W	2298 W	339 W
20000	35^o	100 A	1520 W	2236 W	328 W
20000	45^o	103.5 A	1629 W	2521 W	367 W

7.8 Other concepts

There were other concepts designed and built but the results from those models were either inconclusive or not good enough to be able to motivate further investigation. There was a concept where a new rotor design was made. It utilized a smaller rotor which had smaller magnets and used a flat-PM topology. That motor had lower magnet flux which meant that the flux from the coils had to be higher in order to obtain the same total flux. This motor in particular, required a significantly higher coil flux which meant that the number of turns had to be increased significantly. That created problems with slot area and in the end, it ended up not being smaller or lighter than the concept where the width of the flux path was reduced.

A FEM model skeleton for a 10-pole motor was built but was not further investigated and due to insufficient time, it could not be completed and tested. However, for future projects, the completion of that model could be of interest. Especially when having a new in-house designed and built inverter.

8 Final design

This section will display the performance criteria of the machines and compare the different concepts. Also, the final choice of motor concept will be made.

8.1 Comparison of motors

There were three main comparisons done on the motors. The first was to compare them at rated operation where the results are presented in Section 8.1.1. The second one was to compare them at maximum power which is shown in Section 8.1.2 and finally the weight of the motors was compared which is shown in Section 8.1.3. Also efficiency maps were obtained for three motors and are shown in Section 8.1.4.

8.1.1 Rated operation and efficiency

The simulations at the expected rated operation point were performed in order to estimate what the rated efficiency of the motor would be and what the relative losses to the new cooling surface of the stator would be. The cooling surface is calculated using the outer diameter of the stator and stack length according to

$$A_{cooling} = OD_{stator}\pi L_{stack} \tag{105}$$

where $A_{cooling}$ is the cooling surface. That will be the contact surface between the stator and the cooling jacket which can be seen in Figure 21. That could give an early indication on what cooling requirements are needed for the new motor and if the current cooling system is sufficient. The simulations were performed using the same dq-current angle due to problems when performing MTPA calculations on the models. The dq-current angle was set to 125^o for all of the motors since that in general produced results with high efficiency for all of the motors.

Table 33: Operation at close to the rated torque and speed of the CFS17 motor, iteration 1 and 2 of the PMSM with reduced stack length where the efficiency and relative loss to cooling surface is shown

Motor	CFS17 motor	Concepts 1	Iteration 2
Current magnitude	55.9 A	55.9 A	48 A
Torque	10.8 Nm	9.1 Nm	8.7 Nm
Speed	11 900 RPM	11 900 RPM	11 900 RPM
Copper losses	396.7 W	350 W	289 W
Stator losses	611.3 W	515 W	521 W
Rotor losses	88 W	88 W	86 W
Efficiency	92.5 %	92.2 %	92.4 %
Power loss magnitude	1.01 kW	885 W	824 W
Relative loss -			
- to cooling surface	1	0.96	1.03
Relative loss corrected for 11 kW	1.23	0.99	1.02

Table 34: Operation at close to the rated torque and speed of iteration 3 and 4 of the PMSM with reduced stack length and Concept 2 with reduced outer stator diameter where the efficiency and relative loss to cooling surface is shown

Motor	Iteration 3	Concept 2	Iteration 4
Current magnitude	47 A	40 A	43.2 A
Torque	8.6 Nm	8.5 Nm	9.2 Nm
Speed	11 900 RPM	11 900 RPM	11 900 RPM
Copper losses	277 W	266 W	284 W
Stator losses	506 W	592 W	549 W
Rotor losses	83 W	80 W	82 W
Efficiency	92.5 %	91.9 %	92.6 %
Power loss magnitude	804 W	857 W	848 W
Relative loss -			
- to cooling surface	1.06	0.99	1.09
Relative loss corrected for 11 kW	1	0.96	1.14

One important aspect to consider when studying these results is that all of the simulations were done at the same current angle of 125^o which is not the MTPA angle of the CFS17 motor and likely not for any of the other motors either. One simulation was performed with the MTPA angle on the CFS17 motor in which it was noted that the copper losses as expected was reduced but the rotor losses increased whilst the iron losses remained almost the same. The efficiency at that current angle was calculated to 92.6% which is the same as the efficiency that of Iteration 4. The reason that all of the simulations was not performed at the model respective MTPA angle was that the calculation of the harmonic content of the inductances was not accurate and hence the MTPA angle calculations was incorrect.

The relative loss to cooling surface of the machine gives an idea of where the motor will have its rated operation point. That is the reason that the torque varies to a certain extent due to a higher accuracy required to calculate the relative loss. The exact point of operation is of less interest as compared to the losses since the main reason for performing these simulations is to find the rated torque. If the relative loss is less than one, it means that the motor cannot be sufficiently cooled at that operation point and hence the rated point of operation must be lower. That is the case for the first version of the shortened stack and the reduction in width concept. Iteration 4 turned out to have the highest relative loss and whilst also having the highest power output. That would indicate that the Iteration 4 has the highest point of rated operation.

8.1.2 Maximum power

The maximum power comparison was made by supplying the models with an RMS current which produced the same MMF as when the CFS17 motor was supplied with 125 A in q-direction and 0 A in d-direction. The machines were run at their rated speed of 11900 rpm and their maximum torque, losses and phase voltage would be monitored. If the correct number of turns has been selected, the torque should be the highest for the most efficient motor. The results from these simulations are presented in Table 35.

Table 35: Maximum power of the CFS17 motor, Concept 1 and Iteration 2

Motor	CFS17 motor	Concept 1	Iteration 2
Current	176.8 A	176.8 A	157 A
Torque	24.1 Nm	20.3 Nm	19.4 Nm
Copper losses	3969 W	3502 W	3114 W
Stator losses	1366 W	1152 W	1318 W
Rotor losses	186 W	186 W	171 W
phase voltage magnitude	350 V	295 V	312 V
Power	30 032 W	25 296 W	24 175 W
Efficiency	84.47 %	83.94 %	84 %

Table 36: Maximum power of Concept 2, Iteration 3 and 4

Motor	Iteration 3	Concept 2	Iteration 4
Current	157 A	154 A	145 A
Torque	19.7 Nm	18.6 Nm	19.7 Nm
Copper losses	3114 W	3958 W	3194 W
Stator losses	1275 W	1530 W	1215 W
Rotor losses	168 W	137 W	152 W
phase voltage magnitude	311 V	330 V	350 V
Power	24549 W	23 178 W	23 802 W
Efficiency	84.3 %	80.5 %	83.4 %

The motor will be ran at lower current magnitude as compared to the CFS17 motor which means that it should be possible to have a larger voltage drop over the motor whilst still being able to deliver the same current. When winding the CFS17 motors it is possible although not preferable to add 3-4 more turns to the stator which would increase the fill factor. Should there not be a sufficient number of turns on the coils, they can be added afterwards as long as the motor has not been potted.

8.1.3 Weight reduction and magnet volume

The estimated weight reduction will be expressed in terms of % of material volume. The weight from the stator material, rotor material and copper will be considered. The weight of the copper is the most difficult weight to estimate. The method used to approximate the weight of the windings was to use given weight in the datasheet and relating it to the per phase wire resistance. The wire resistance is calculated using (85) and by estimating the wire length, the resistance is can be calculated as

$$R_{phase} = \rho_{copper} \frac{N_{turn,phase}^2 N_{slot}}{3A_{cu}} 2(L_{stack} +$$

$$+2 \cdot h_{insulation} + 4 \cdot (\frac{A_{slot}}{4(OD_{stator}/2 - ID_{stator}/2 - L_{tooth,w} - Hs0))} + 2L_{tooth,w})) \tag{106}$$

Where:

- R_{phase} is the phase resistance [Ω]
- N_{slots} is the number of stator slots
- L_{stack} is the stack length [m]
- OD_{stator} is the outer diameter of the stator [m]

- ID_{stator} is the inner stator diameter $[m]$
- H_{S0} is the slot opening height $[m]$
- $L_{tooth,w}$ is the length of the non-slot wedge tooth length $[m]$
- A_{cu} is the copper area in the slot $[m^2]$
- $h_{insulation}$ is the end winding insulation height $[m]$

These geometry definitions used to calculate the wire length are illustrated in Figure 23. That is assuming that the wire diameter is unchanged. Also, the magnet volume is an important factor when it comes to cost of the motor. In the Tables 37 and 38, the weight of the different parts of the motors are shown and the magnet volume is shown.

Table 37: Weight summary and magnet volume of the CFS17 motor, iteration 1 and 2 of the PMSM with reduced stack length

Motor	CFS17 motor	Concept 1	Iteration 2
Stator iron weight	1.65 kg	1.39 kg	1.29 kg
Rotor iron weight	0.54 kg	0.45 kg	0.45 kg
Copper weight	0.6 kg	0.53 kg	0.59 kg
Magnet volume per pole	5.4 cm^3	4.6 cm^3	4.6 cm^3
Total weight	2.79 kg	2.37 kg	2.33 kg
Percent weight reduction	0 %	15 %	16.5 %

Table 38: Weight summary and magnet volume of iteration 3 and 4 of the PMSM with reduced stack length and the PMSM with reduced outer stator diameter

Motor	Iteration 3	Concept 2	Iteration 4
Stator weight	1.29 kg	1.15 kg	1.32 kg
Rotor weight	0.44 kg	0.54 kg	0.44 kg
Copper weight	0.59 kg	0.72 kg	0.79 kg
Magnet volume per pole	5 cm^3	5.4 cm^3	5.4 cm^3
Total weight	2.32 kg	2.41 kg	2.55 kg
Percent weight reduction	16.8 %	13.6 %	12 %

From Tables 37 and 38 it can be seen that all of the motors will lead to substantial weight reduction as compared to the previous motor. One very important note when it comes to weight is that the power density of iteration 4 is reduced as compared to the CFS17 motor which is not desirable. The power density should be possible to improve and will be discussed further in the future work section.

8.1.4 Efficiency maps

For the efficiency maps, only three motors would be compared to the CFS17 motor. The reason for this is the computational time required to perform these simulations. As previously mentioned, only three maps were obtained and are presented in Figure 60. Only values up till torque levels of 20 Nm was obtained and in the case of the CFS17 motor, that was deemed sufficient even though it did not cover the full torque span of the motor. The reason for this is that the comparison at maximum power in the previous section was deemed sufficient and that the time required to run the final simulations could not be motivated.

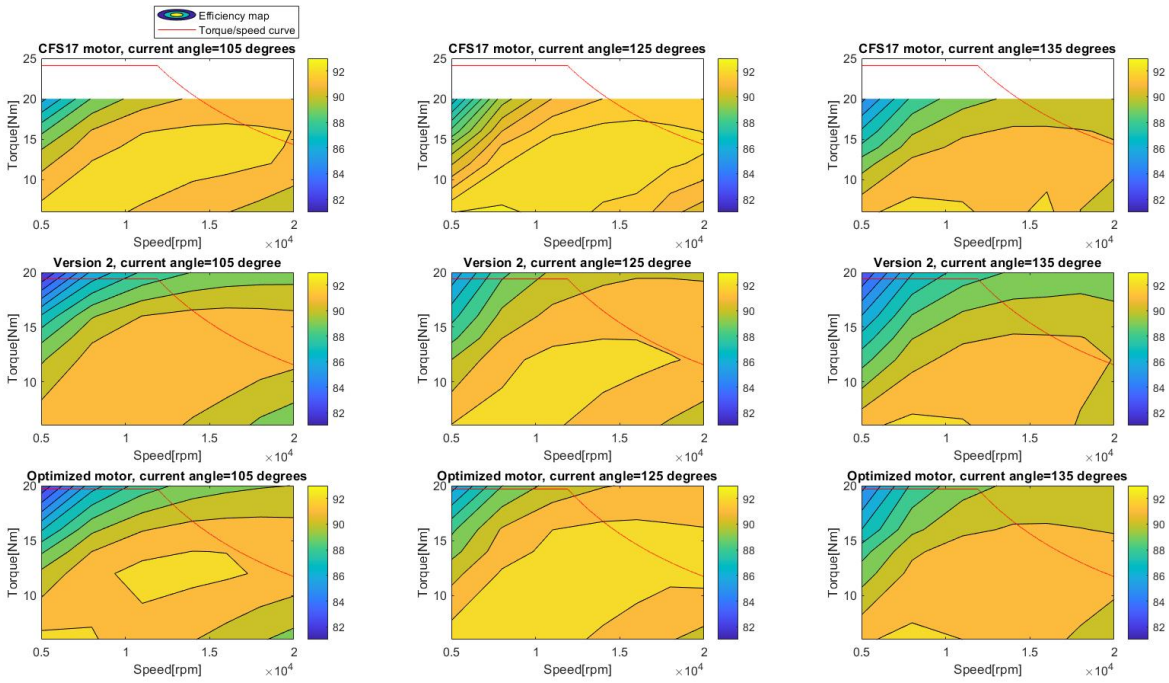

Figure 60: Low resolution of the efficiency maps of the CFS17 motor, iteration 2 and 4 of the reduced stack length

When studying these results, it should be kept in mind that the current was set manually and the accuracy of the torque output which was deemed acceptable was set to $\pm 0,2\ Nm$. That could have more of an impact at lower torque levels where it could skew the actual power output by up to 3-4 %.

From these plots, it should be noted that the behaviour between Iteration 4 and the CFS17 motor is similar which could indicate that they also will behave similarly in reality. It can also be seen that the changes made from version two of the shortened stack to the final Iteration led to a larger span where relatively high efficiency is obtained.

Another important aspect which can be examined on the efficiency maps. Depending on the gear ratio that is used in the car, the RMS speed and torque changes. For that reason, it is important to have a wide span at which the efficiency is high to avoid requiring a re-design if the gear ratios are changed. It can be noted that the span where high efficiency is obtained for Iteration 4 is larger than that of the CFS17 motor and the second version of the shorter stack concept. That means that this motor may be less sensitive to changes in gear ratios.

8.2 Recommendation of concept PMSM

When making the final recommendation of which of these motors would be the most suitable for CFS, the total weight of the motor and the efficiency will be the main two factors considered whilst also taking into account any large changes in manufacturability and/or cost of the motor.

The first version of the reduction in stack length will not be recommended as a suitable machine since the copper losses are significantly higher than that of the other motors. It is also had the highest rotor losses at rated speed as compared to the other versions. The rotor losses were the same as in the CFS17 motor and with a smaller thermal mass in the rotor, there could be a risk of it overheating.

The concept using the smaller outer stator diameter did show promise in terms of the location of the losses were mainly the iron losses increased but due to it not providing a significant reduction in weight whilst also not reducing the diameter significantly, it cannot be recommended for future CFS teams. It was also the least efficient concept of the two.

Iteration 2 of the reduction in stack length was more efficient than the first version and that could mainly be attributed to the decrease in copper losses in the stator. The rotor losses also decrease slightly whilst the iron losses increased. The increase in iron losses can probably be attributed to the increase in stator reluctance as a result of the larger slots required to maintain the fill factor. This version was 0.1 % less efficient at rated speed compared to the CFS17 motor and the largest proportional increase in losses was in the rotor. The reduction in stack length also did lead to the largest reduction in weight as compared to the reduction in flux path width. The stator design was kept for the third iteration and was initially intended to be the one recommended for future use for CFS but it was later noticed that its phase voltage waveforms which had significant 5:th and 7:th order harmonic magnitudes.

Iteration 3 of the reduction in stack length had a new rotor design with thicker magnets which increased the magnet MMF and hence increased the magnet flux in the machine. That meant that the flux from the coils could be reduced and hence the copper losses decreased. Also, the flux distribution in the stator and rotor core changed which led to lower rotor losses and lower iron losses. This version also proved to be the more efficient and had similar efficiency to iteration 2.

Due to the problems with the harmonic content in the phase voltage combined with a magnitude which was too low it was decided to make one final iteration of the stator. In that version the stator was altered to reduce points in the stator where high flux densities are achieved. That version sacrificed a bit of its power density in order to obtain better EMF wave forms. This motor proved to have significantly reduced rotor losses and to have significantly improved phase voltage wave forms. This version of the motor proved to be about 5 % heavier than its predecessor but due to the problems that the phase voltage could cause combined with a lower efficiency of that version this stator will be recommended.

To summarize, the fourth iteration of the reduction of stack length is recommended as the new front motors for the CFS22 team. That is because of it having the highest efficiency of the investigated motors combined whilst also having the lowest harmonic content of all of the versions. It also had lower rotor losses which indicates that the risk of having overtemperatures in the rotor and thereby demagnetizing the magnets is reduced.

8.3 Suggested manufacturing methods of the motor

When manufacturing the motor, the methods used could significantly impact the performance of the motor. The findings from the literature study conducted and summarized in Chapter 4 indicates that the stator laminations should preferably be cut using wire electrical discharge machining since that is more suitable for prototype and low quantity production combined with having lower degradation effects on the material. The bonding should be done using coating since that will have the lowest risk of failure combined with lower levels of degradation and having lower Eddy current losses. The end-winding insulation will be a transferable part from the old to the new motor. In that way, they will not need to be manufactured separately.

The winding of the stator will be done by hand or partially with a needle and the rest by hand. The reason for this is that the changes that would be required in order to fully wind the coils in a machine would have a significant impact on the performance of the machine. The coils would ideally be connected in series but since that would require a thicker wire, that would be required to be tested in order to verify if it is possible or not in terms of winding.

The motors should be potted since that method has been used in the past but that is something that should be studied further since there are significant benefits if that could be avoided in terms of being able to remove damaged windings. Not potting the motor may however lead to higher risks of insulation failures in the windings and worsened heat dissipation from the coils. Also the risk of windings coming loose will be more likely.

8.4 Suggested prototype manufacturing and testing

The winding of the prototype should be done slightly differently where it should be done with 2 mm wires instead of 1.12 mm and the coils should be connected in series. The number of turns per coil should them be 1/3 of the number specified in Section 7.6. The motor should initially not be potted since that would make it impossible to adjust the number of turns if it should be needed. The initial tests should monitor the phase voltage and if it is possible, check if the maximum torque can be produced at the intended base speed. If it cannot be done, one turn per stator tooth should be removed and the tests should be re-done. Having to remove turns will lead to higher copper losses at all torques which makes it even more important to have the largest phase voltage possible whilst still being able to push maximum torque at rated speed. These tests must be performed for short durations to avoid overheating the coils and the stator.

Once the correct phase voltage has been ensured, the motor can be potted and then a temperature test can be performed. The temperature test entails running the motor as base speed and base torque and the rotor and stator temperatures are monitored. The motor should run until the temperatures reach equilibrium or the maximum temperature. Should the motor reach maximum temperature, the motor will have to be downrated and the base operation point must be lowered in terms of torque or speed. The expected rated power should be slightly higher than 11.5 kW which should be confirmed when testing. According to the data from the drive cycle analysis that rated power will be sufficient for all expected operating conditions for the front motor.

9 Conclusion

The aim of this thesis is to re-design the CFS17 PMSM to suit the performance requirements of the front hub motors of the CFS21 car. Drive cycle analysis was used to obtain the parameters, needed for the new PMSM. A 1-D powertrain model was used to run the drive cycles which was also used in 2017 when the parameters of the old motors was found. The power train model was updated, and new drive cycles were created with more up to date data. The results indicated that a new smaller motor could be obtained. The new motor should be able to deliver maximum 20 Nm at 12 000 RPM and be 8.7 Nm continuously.

The FEM model of the CFS17 motor was provided by AROS electronics of which two design concepts were made. These concepts were implemented the FEM software and the results were evaluated in Chapter 4. IRO AB provided feedback on the manufacturability of the motor, the manufacturing methodology was specified, and the designs were adjusted in order to be able to implement the chosen methodology. The designs were evaluated, and the most suitable design choice was chosen based on the results presented in Chapter 8. A shorter stack with thicker magnets in the rotor and a higher number of coil turns proved to be the most suitable motor. The new motor will be able to deliver 19.7 Nm at 12 000 RPM and more than 9.1 Nm continuously with an estimated efficiency of 92.6 % which is 0.1 % higher than the old CFS17 motor. The stator and rotor iron combined with the copper in the windings will weigh 12 % less than the old CFS17 motor.

10 Future work

Before making a motor prototype, there are some considerations and further work required.

- The total power density of the machine is reduced and that is a consequence of EMF waveform problems in the machine. For future work, the iteration 4 motor model could potentially be used as a base-line design and then make smaller changes to reduce the weight further.
- A study of the rotor topology should be conducted and changing the magnet topology to a V-shape or decentred magnet topology. By doing that, it might be possible to increase the MMF produced by the magnets. In such a study, the magnet dimensions can also be varied. That could be suitable as a design project team within Formula Student or as a standalone design project.
- The stator can be optimized more to minimize the iron losses whilst maintaining the weight reduction. The weight might even be able to be further reduced. The area that is of the main interest is the slots where if possible, a topology optimization should be performed. When performing the optimization, the fill-factor should be maintained in order to not affect the manufacturability of the motor. One way to study this in detail is to make a full motor in 2-D instead of just a fraction of it. Then study the flux density distributions at different instances during one electric cycle when the losses have stabilized. Having instances of high flux distributions in the core will lead to higher hysteresis losses and hence it would be of interest to try to limit them without increasing the weight of the stator.
- Since CFS21 is developing a new inverter, the concept of increasing the number of poles in the motor should be examined. The concept has been built in the FEM software, but extensive optimization or testing has not been performed. The use of more poles will require a higher electrical frequency of the motor, but the motor will be able to produce a higher overall flux and hence the potential torque production increases. It is not certain that a larger number of poles will be possible when having such a small rotor, but it should be investigated.
- In order to be able to obtain more reliable data on what performance requirements are needed from the front motors, in car testing should be done where the maximum power that can be regenerated can be examined. Also, the power-flow during an endurance run and during autocross should be examined in detail in order to be able to see where the actual rated torque and power is.
- Also, the torque vectoring system should be tested in the car and the extreme cases should be tested in terms of how the power could be distributed during a turn. Since the CFS17 motors are over dimensioned, they can be used to see what the extreme cases are and by utilizing power limiting in the motors, the theoretical behaviour of the new motors can be examined. From that data, conclusions can be made regarding if they are dimensioned correctly or not.
- In order to test the regenerative braking properly, the battery cells would require extensive testing in order to be uprated such that they can handle higher levels of regenerative braking. Also, the power requirement, of the rear motor should be examined and if a new design would be needed there. Since CFS22 will have a new gearbox with a new gear ratio, the power requirements of the motor should be examined again. Preferably during the summer of 2021 when more test data is available.
- When designing new motors, the FEM software can be controlled using MATLAB and that will save significant time when compared to doing everything by hand. There exists old code which maybe could be modified to be able to be used for future re-designs of the motors.

References

[1] FSG, *Formula student rules 2020*, 2020. [Online]. Available: https://www.formulastudent.de/fileadmin/user\textunderscoreupload/all/2020/rules/FS-Rules\textunderscore2020\textunderscoreV1.0.pdf.

[2] B. J. et al, *Vehicle dynamics compendium for course mmf062*, University Compendium, 2015.

[3] A. Andersson and M. Vencel, "Design and verification of a sic voltage source inverter for chalmers formula student", Master's thesis, Chalmers University of Technology, 2020.

[4] E. Lund and R. Lause, "Design and implementation of a pmsm control system for use in a formula student car", Master's thesis, Chalmers University of Technology, 2020.

[5] R. A. Serway and J. W. J. Jr, *Physics for Scientist and Engineers with Modern Physics*, English, 9th ed. 2015, ISBN: 978-1-305-40196-9.

[6] S. J. Chapman, *Electric Machinery Fundamentals fifth edition*. Avenue of the Americas, New York: McGraw-Hill, 2011, ISBN: 978-0-07-352954-7.

[7] D. K. Cheng, *Field and Wave Electromagnetics, Seventh Edition*. Edinburgh gate, Harlow: Pearson education limited, 2013.

[8] Y. Liu, J. Tang, N. Sharma, and A. Rodionov, "Electrical machines, design and analysis", unpublished, unpublished.

[9] P. Sekerak, V. Hrabovcova, J. Pyrhönen, L. Kalamen, P. Rafajdus, and M. Onufer, "Comparison of synchronous motors with different permanent magnet and winding types", *IEEE Transactions on Magnetics*, vol. 49, pp. 1256–1263, Mar. 2013. DOI: 10.1109/TMAG.2012.2230334.

[10] M.-D. Calin and E. Helerea, "Temperature influence on magnetic characteristics of ndfeb permanent magnets", *2011 7th International Symposium on Advanced Topics in Electrical Engineering, ATEE 2011*, Jan. 2011.

[11] L. Harnefors, *Control of Variable-speed Drives*. Applied Signal Processing and Control, Department of Electronics, Mälardalen University, 2002. [Online]. Available: https://books.google.se/books?id=wyXXjwEACAAJ.

[12] R. H. Park, "Two-reaction theory of synchronous machines generalized method of analysis-part i", *Transactions of the American Institute of Electrical Engineers*, vol. 48, no. 3, pp. 716–727, 1929. DOI: 10.1109/T-AIEE.1929.5055275.

[13] P. Pillay and R. Krishnan, "Modeling of permanent magnet motor drives", *IEEE Transactions on Industrial Electronics*, vol. 35, no. 4, pp. 537–541, 1988. DOI: 10.1109/41.9176.

[14] P. Kundur, *Power System Stability and Control*. New York: McGraw-Hil, 1994, pp. 1–1200, ISBN: 978-0070359581.

[15] W. C. Duesterhoeft, M. W. Schulz, and E. Clarke, "Determination of instantaneous currents and voltages by means of alpha, beta, and zero components", *Transactions of the American Institute of Electrical Engineers*, vol. 70, no. 2, pp. 1248–1255, 1951. DOI: 10.1109/T-AIEE.1951.5060554.

[16] J. Pyrhönen, T. Jokinen, and V. Hrabovcová, *Design of Rotating Electrical Machines*, English, 2nd ed. 2013, ISBN: 978-1-118-58157-5.

[17] A. Lehikoinen, N. Chiodetto, E. Lantto, A. Arkkio, and A. Belahcen, "Monte carlo analysis of circulating currents in random-wound electrical machines", *IEEE Transactions on Magnetics*, vol. 52, no. 8, pp. 1–12, 2016. DOI: 10.1109/TMAG.2016.2535332.

[18] A. Al-Timimy, P. Giangrande, M. Degano, M. Galea, and C. Gerada, "Investigation of ac copper and iron losses in high-speed high-power density pmsm", Sep. 2018, pp. 263–269. DOI: 10.1109/ICELMACH.2018.8507166.

[19] G. Bertotti, F. Fiorillo, and G. Soardo, "The prediction of power losses in soft magnetic materials", *http://dx.doi.org/10.1051/jphyscol:19888867*, vol. 49, Dec. 1988. DOI: 10.1051/jphyscol:19888867.

[20] D. Lin, P. Zhou, W. Fu, Z. Badics, and Z. Cendes, "A dynamic core loss model for soft ferromagnetic and power ferrite materials in transient finite element analysis", *Magnetics, IEEE Transactions on*, vol. 40, pp. 1318 –1321, Apr. 2004. DOI: 10.1109/TMAG.2004.825025.

[21] J. Cros and P. Viarouge, "Synthesis of high performance pm motors with concentrated windings", *IEEE Transactions on Energy Conversion*, vol. 17, no. 2, pp. 248–253, 2002. DOI: 10.1109/TEC.2002.1009476.

[22] P. Lindh, J. Nerg, J. Pyrhönen, M. Polikarpova, H. Jussila, and M. Rilla, "Interior permanent magnet motors with non-overlapping concentrated windings or with integer slot windings for traction application", *Przeglad Elektrotechniczny*, vol. 88, pp. 9–12, Jan. 2012.

[23] K. Yamazaki, Y. Fukushima, and M. Sato, "Loss analysis of permanent magnet motors with concentrated windings - variation of magnet eddy current loss due to stator and rotor shapes", in *2008 IEEE Industry Applications Society Annual Meeting*, 2008, pp. 1–8. DOI: 10.1109/08IAS.2008.55.

[24] Y.-Y. Choe, S.-Y. Oh, S.-H. Ham, I.-S. Jang, S.-Y. Cho, j. Lee, and K.-C. Ko, "Comparison of concentrated and distributed winding in an ipmsm for vehicle traction", *Energy Procedia*, vol. 14, Dec. 2012. DOI: 10.1016/j.egypro.2011.12.1103.

[25] A. Krings, S. A. Mousavi, O. Wallmark, and J. Soulard, "Temperature influence of nife steel laminations on the characteristics of small slotless permanent magnet machines", *IEEE Transactions on Magnetics*, vol. 49, no. 7, pp. 4064–4067, 2013. DOI: 10.1109/TMAG.2013.2255026.

[26] S. Raj, R. Aziz, and M. Ahmad, "Influence of pole number on the characteristics of permanent magnet synchronous motor (pmsm)", *Indonesian Journal of Electrical Engineering and Computer Science*, vol. 13, pp. 1318–1323, Mar. 2019. DOI: 10.11591/ijeecs.v13.i3.pp1318-1323.

[27] S. Skoog and A. Acquaviva, "Pole-slot selection considerations for double layer three-phase tooth-coil wound electrical machines", in *2018 XIII International Conference on Electrical Machines (ICEM)*, 2018, pp. 934–940. DOI: 10.1109/ICELMACH.2018.8506772.

[28] Seun Guy Min and B. Sarlioglu, "Investigation of electromagnetic noise on pole and slot number combinations with possible fractional-slot concentrated windings", in *2017 IEEE Transportation Electrification Conference and Expo (ITEC)*, 2017, pp. 241–246. DOI: 10.1109/ITEC.2017.7993278.

[29] N. Bianchi and M. Dai Pre, "Use of the star of slots in designing fractional-slot single-layer synchronous motors", *IEE Proceedings - Electric Power Applications*, vol. 153, no. 3, pp. 459–466, 2006. DOI: 10.1049/ip-epa:20050284.

[30] N. Bianchi, S. Bolognani, and E. Fomasiero, "A general approach to determine the rotor losses in three-phase fractional-slot pm machines", in *2007 IEEE International Electric Machines Drives Conference*, vol. 1, 2007, pp. 634–641. DOI: 10.1109/IEMDC.2007.382741.

[31] S. Sharkh, J. Renedo Anglada, and M. Yuratich, "Rotor losses in pm synchronous machine", Jul. 2017.

[32] H. Zhang and O. Wallmark, "Limitations and constraints of eddy-current loss models for interior permanent-magnet motors with fractional-slot concentrated windings", *Energies*, vol. 10, p. 379, Mar. 2017. DOI: 10.3390/en10030379.

[33] L. Chong, *Design of an interior permanent magnet machine with concentrated windings for field weakening applications*, 2011.

[34] L. Chong, R. Dutta, and M. Rahman, "Field weakening performance of a concentrated wound pm machine with rotor and magnet geometry variation", Aug. 2010, pp. 1 –4. DOI: 10.1109/PES.2010.5589868.

[35] F. Ma, H. Yin, L. Wei, G. Tian, and H. Gao, "Design and optimization of ipm motor considering flux weakening capability and vibration for electric vehicle applications", *Sustainability*, vol. 10, p. 1533, May 2018. DOI: 10.3390/su10051533.

[36] W. Purwanto, R. Risfendra, D. Fernandez, D. Sudarno Putra, and T. Sugiarto, "Design and comparison of five topologies rotor permanent magnet synchronous motor for high-speed spindle applications", *International Journal of GEOMATE*, vol. 13, pp. 148–154, Jan. 2017. DOI: 10.21660/2017.40.02765.

[37] C. Studer, A. Keyhani, T. Sebastian, and S. K. Murthy, "Study of cogging torque in permanent magnet machines", in *IAS '97. Conference Record of the 1997 IEEE Industry Applications Conference Thirty-Second IAS Annual Meeting*, vol. 1, 1997, 42–49 vol.1. DOI: 10.1109/IAS.1997.643006.

[38] Touzhu Li and G. Slemon, "Reduction of cogging torque in permanent magnet motors", *IEEE Transactions on Magnetics*, vol. 24, no. 6, pp. 2901–2903, 1988. DOI: 10.1109/20.92282.

[39] F. Meier, "Permanent-magnet synchronous machines with non-overlapping concentrated windings for low-speed direct-drive applications", 2008.

[40] W. Tong, *Mechanical design of electric motors*. Jan. 2014, pp. 1–680. DOI: 10.1201/b16863.

[41] Bayraktar and Y. Turgut, "Effects of different cutting methods for electrical steel sheets on performance of induction motors", *Proceedings of the Institution of Mechanical Engineers Part B Journal of Engineering Manufacture*, vol. 232, pp. 1287–1294, Aug. 2016. DOI: 10.1177/0954405416666899.

[42] M. Bali, H. De Gersem, and A. Muetze, "Finite-element modeling of magnetic material degradation due to punching", *IEEE Transactions on Magnetics*, vol. 50, no. 2, pp. 745–748, 2014. DOI: 10.1109/TMAG.2013.2283967.

[43] A. J. Clerc and A. Muetze, "Measurement of stator core magnetic degradation during the manufacturing process", *IEEE Transactions on Industry Applications*, vol. 48, no. 4, pp. 1344–1352, 2012. DOI: 10.1109/TIA.2012.2199950.

[44] Y. Gai, M. Kimiabeigi, Y. Chuan Chong, J. D. Widmer, X. Deng, M. Popescu, J. Goss, D. A. Staton, and A. Steven, "Cooling of automotive traction motors: Schemes, examples, and computation methods", *IEEE Transactions on Industrial Electronics*, vol. 66, no. 3, pp. 1681–1692, 2019. DOI: 10.1109/TIE.2018.2835397.

[45] A. Krings, J. Soulard, and O. Wallmark, "Pwm influence on the iron losses and characteristics of a slotless permanent-magnet motor with sife and nife stator cores", *IEEE Transactions on Industry Applications*, vol. 51, Mar. 2015. DOI: 10.1109/TIA.2014.2354735.

[46] K. Yamazaki and Y. Fukushima, "Effect of eddy-current loss reduction by magnet segmentation in synchronous motors with concentrated windings", *IEEE Transactions on Industry Applications*, vol. 47, no. 2, pp. 779–788, 2011. DOI: 10.1109/TIA.2010.2103915.

Appendix A

Author:	Date:	Rev:	Rev date:
UTV/BJ	2018-02-22	A	-

Technical data sheet
CFS18 stator/rotor

Stator/rotor

Active dimensions: D/d-L = 90/50-70 mm
Stator stack: 01-1010_Prel-B / 01-1011_Prel-B
Rotor: 2 x 01-1009_Prel-A
Rotor inertia: 1.37 kg*cm^2 /rotor section

Winding

Number of windings: 9
Phase interconnection: 3 in parallel per phase (1,4 and 7 etc), Y-connection
Number of winding turns: 41
Winding wire: Ø 1.12 mm (core dia)
Amount of winding wire: ~600 g
Phase to phase resistance: 100 mOhm ±5%
Phase to phase EMF: 55.9 VRMS ±5% @ 4000 rpm
Rated voltage: 600 VAC
High voltage testing (windings and temp. sensor): 1000 VAC, 2s and max 0.1 mA
Temperature class: F
Temperature sensor: KTY84 - 130

Cooling

Type: Circulating water, with optional antifreeze and anti-corrosion additives
Coolant inlet temperature: max 40 °C @ rated output power
Volume flow: min 9 l/min @ rated output power (ΔT 5 K)
Winding temperature increase: ~13 K/s @ peak torque

Performance

Rated torque: 10.8 Nm
Peak torque: 24.1 Nm

Rated speed: 11900 rpm
Max mechanical speed: 20000 rpm

Rated output power: 13.5 kW
Peak output power: 32 kW

Motor current: 48 A @ rated output power

Efficiency: 91% @ rated output power